ENHANCED RAMAN EFFECT ON MBE GROWN SEMICONDUCTOR QUANTUM DOTS

By
RICHARD LIVINGSTONE

A dissertation submitted to the Graduate Faculty in Chemistry in partial fulfillment of the requirements for the degree of Doctor of Philosophy, The City University of New York.

2010

This manuscript has been read and accepted for the
Graduate Faculty in chemistry in satisfaction of the
dissertation requirement for the degree of Doctor of Philosophy.

Prof. John R. Lombardi

08/13/2010
Date

Chair of Examining Committee

Prof. Mahesh Lakshman

08/13/2010
Date

Executive Officer

Prof. Lou Massa

Prof. Ronald L. Birke

Dr. Marco Leona

Prof. John R. Lombardi
Supervisory Committee

THE CITY UNIVERSITY OF NEW YORK

Abstract

Enhanced Raman Effect On MBE Grown Semiconductor Quantum Dots

By Richard Livingstone

Advisor: John R. Lombardi

Using Surface Enhanced Raman Spectroscopy (SERS), I observed Raman enhancements (10^4-10^5) for pyridine, 4-tertbutylpyridine and other biological molecules adsorbed on a II-VI semiconductor CdSe/ZnBeSe sample of uncapped self-assembled quantum dots produced by molecular beam epitaxy. When a monolayer of Raman active molecule is adsorbed on these structures, excitation at 488 nm produces intense Raman spectra and a very large enhancement of the a_1, b_1 and b_2 modes. This indicates the presence of charge-transfer as a contributor to the enhancement. Furthermore, the excitation wavelength is in the vicinity of several interband transitions located both in the quantum dots and the wetting layer, and it is likely that these resonances also contribute to the enhancement factor. The observed enhancement is among the largest yet seen on semiconductor quantum dot systems and is the first obseved on MBE grown quantum dots.

The observed Raman spectrum shows several differences from the normal Raman spectrum, and is closer in some ways to the SERS observed on Ag nanoparticles. Among other things, the prominence of non-totally symmetric lines indicates the importance of charge-transfer contributions to the overall enhancement. In Ag nanoparticle SERS, both the charge-transfer and surface plasmon resonances have been shown to be responsible for the effect. However, in semiconductors, the excitation wavelengths are far from the

region of surface plasmon resonance for CdSe and so the magnitude of enhancement must be attributed to other possible resonances.

Bandgap dependence studies using 4-tertbutylpyridine on semiconductor quantum dots with varying bandgap energies, indicates that transitions to the bandgap are important contributors to the overall enhancement, and may possibly be regarded as a replacement for the surface plasmon resonance so important in metallic SERS. As in SERS, however, the observation of non-totally symmetric bands indicates additional contributions from charge-transfer resonances. It is most likely a combination of these two effects which is responsible for the rather large enhancements observed here.

Acknowledgements

This thesis would never be completed without the guidance of my academic mentor Professor John R. Lombardi. His encouragement and inspiration through tough situations has allowed me to increase my knowledge and confidence in art of scientific research. I would like to thank him for his confidence in me and for allowing me the opportunity to become a better scientist.

I would like to extend a special thank you to Professor Ronald Birke, and Dr. Marco Leona for serving on my dissertation committee. Your advice and guidance throughout my research is greatly appreciated. I am especially indebted to another member of my dissertation committee, Prof. Lou Massa for his kind support, incredible understanding and effort with my defense. Your efforts will be forever appreciated.
I wish to thank also Professor Maria Tamargo for her patience and understanding in arranging the MBE growth of my samples, Dr. Lucia Quagliano for her assistance. Professor Mahesh Lakshman for his tireless effort in making my defense possible.

I owe my deepest gratitude to Mrs. O. Diane Adebowale, Assistant Program Officer, Chemistry Department, for your unyielding support and encouragement throughout some of the most difficult times of this research; for your untiring effort in especially the final days before my defense, making sure that this moment would happen, even when it did not seem possible. For continuously watching out for my best interest as I progress through my PhD program and beyond, my heartfelt thank you. This celebration would be impossible without your support. I trust that God will give you the strength to continue impacting the lives of the students who will be very fortunate to meet you. I will be forever grateful for all that you did for me in making this research successful.

I am grateful to Dr. Noemi Perez Paz and Dr. Xuecong Zhou for assistance in growing my samples; Tatiana Teslova, Dr. Bing Zhao, Dr. Weiqing Xu, Dr. Maria Vega Canamares and especially Dr. Deanna O'Donnell, my friends and colleagues without your help at various stages of my research this would not be possible. A very special thank you to my colleague and friend Dr. Fleumingue Jean-Mary who made immense effort in assisting me with the AFM images of my samples, taught me the techniques in AFM, a great pillar of support and encouragement through the very difficult and frustrating days of my research. I will be forever grateful.

I would also like to thank Mrs. Jemma Poyer and Denise Addison in the Chemistry office at City College for all their assistance throughout my research; Mr. Derek Quinlan, Chemistry Department at City College and the staff at Evergreen Laser Cooperation, Durham Connecticut for your technical assistance with the lasers used in my research.

Words fail me to express my appreciation to my wife Grace whose dedication, love and persistent confidence in me, brought me through very tough and frustrating days during my research. You are my pillar of strength and support, without you this day would have never been possible. I am indebted to you for the rest of my life, again my heartfelt thank you for your unwavering and passionate support. To my daughter and little angel Dena, thank you for your support, love and understanding, throughout these challenging years.

I gratefully acknowledge the funding sources that made my Ph.D. work possible. I was supported by the MARC/RISE Fellowship, National Science Foundation under Cooperative Agreement No. RII-9353488, grant No. CHE-0091362, CHE-0345987 and

grant number ECS0217646 and by the City University of New York PSC-BHE Faculty Research Award Program. I am also indebted to the National Institute of Justice (Department of Justice award No. 2006-DN-BX-K034) and the City University Collaborative Incentive program (No. 80209)

Last but not least, thanks be to God for guiding my life through all tests in the past few years. Through whom all things were made possible.

This is dedicated to my loving wife Grace Livingstone and daughter Dena Livingstone for your unyielding love and support.

Table of Contents

List of Tables

List of Figures

Chapter 1. Introduction

The discovery of useful applications of two-dimensional (2D) quantum well heterostructures in the early 1980's resulted in the exploration of other heterostructures with reduced dimensionality such as quantum wires and quantum dots (QDs). However it was not until 1982 when Arakawa and Sakaki[1] theoretically described the effects of size quantization on three dimensional systems, as artificial atoms with the electrons confined in all three dimensions, these heterostructures were first referred to as quantum dots. Their experimental studies allowed insight into the structure and applications of QDs and demonstrated valuable advantages of these quantum-size heterostructures in laser applications, including huge increase in the material gain, a lower lasing threshold current, and reduction of temperature influence in the device performance. These discoveries led Ekimov and Onushchenko[2] to fabricate the first semiconductor dots based on II-VI micro-crystals in glass matrix. The quality of the structure's interface between the glass and semiconductor dot was low, and therefore restricted its applications. Colloidal quantum dots, such as CdSe[3] and CdS[4] which have been extensively fabricated, solved the problem of low quality dots found in the glass matrix of solid state semiconductor dots, however, new problems such as the size dispersion, and stability of some of the semiconductor colloidal solutions arises.

The revolutionary development of new growth techniques such as molecular beam epitaxy (MBE) and metal organic carbon vapor deposition (MOCVD), led to greater control of the growth process of these semiconductor quantum dots, giving rise to quantum dots with a variety of physical and chemical properties. The MBE growth technique allows the fabrication and study of spontaneous QD formation. This self-

assembling technique used in fabricating nanoscale islands led to a breakthrough in QD devices, specifically, in the laser applications.

Low dimensional structures with new optical and optoelectronic applications, such as quantum dots fabricated from II-VI semiconductors using MBE techniques, are of special interest, due to the higher exciton binding energy and the large energy band gap of these materials[5]. These wide band gap quaternary ($Zn_xCd_yMg_{1-x-y}Se$) material system, can be grown lattice matched to the InP substrate giving rise to a wide selection of band gaps, 2.1 eV to ~3.6 eV[6,7], covering most of the visible spectrum and the near ultraviolet region. This variation in band gap properties allow these quantum dot systems to be used as cladding and waveguides in laser diodes (LD) and light emitting diode (LEDs) designs.[6]

The nature, importance and invaluable applications of semiconductor quantum dots, in recent years, resulted in increasing interest in monodisperse nanostructures, either in gas phase studies, colloidal suspension, or implanted on solid surfaces. This research is of special interest in the field of semiconductors, where nanocrystals often display discrete, atom-like valence (hole) and conduction (electron) levels due to quantum confinement effects[8]. Quantum dots are possible building blocks for novel electronic as well as photonic devices, for example both a single-electron transistor[9] and a light emitting diode[10] have been constructed from a CdSe quantum dot. Quantum dots have also found application in the field of biosensors[11,12]. The performance of these devices depends critically on the properties of the surface features, their structural details as well as the optical and electrical responses. It is therefore of interest to explore spectroscopic means of determining these properties.

Raman spectroscopy as a surface spectroscopic probe has several potential advantages such as high spectral resolution and the ability to probe interfaces. However, the low intensity of normal Raman scattering has prevented its wide application to surface studies. Under normal conditions for vibrational studies of adsorbed species, Raman scattering is too weak to be detectable. To overcome these restrictions, surface enhanced Raman scattering (SERS) has found usefulness in providing surface and interface Raman studies in metals. The SERS effect is characterized by an enormous increase in the Raman intensity by many orders of magnitude for species adsorbed on rough metal surfaces compared to that obtained from the same number of molecules in solution or the gas phase[13,14,15,16]. Typical enhancement factors obtained on a roughened Ag surface are on the order of 10^6. The enhancement process is generally accepted as having several mechanisms contribute to the overall enhancement of the Raman signal. Electromagnetic theories predict that the electric field at the metal surface becomes very large when excitation takes place within surface plasmon resonances of the roughened features. The chemical enhancement mechanism is generally mentioned as a charge-transfer process.

As surface spectroscopy, the SERS technique has as number of important advantages: sensitivity, selectivity, non-destructive detection, and feasibility for *in-situ* studies. Besides, this spectroscopy enables the determination of detailed information about adsorbed species like their molecular structure and orientation .

1. 1 Objectives of Thesis

This dissertation presents a summary of the MBE growth process and the first detail report of surface enhance Raman spectroscopy characterization of II-VI wide bandgap semiconductor quantum dots. Also discussed is an atomic force microscopy (AFM) technique used to measure the size and density of dots on the surface. The probe molecules used were pyridine, 4-tert-butylpyridine, tyrosine, tryptophan and adenine. Two types of self-assembly semiconductor quantum dots were used in this study. The first was CdSe/$Zn_{1-x}Be_xSe$, (with x =0.03 which allows near lattice match between the GaAs and the ZnSe layer), resulting in the formation of quantum dots with fixed bandgap. The other was CdSe quantum dots fabricated on a quaternary layer of ZnCdMgSe. Varying the Mg deposition temperature resulted in the fabrication of quantum dots with different bandgap.

4-Tert-butylpyridine (4tBP) was chosen a probe molecule, since it is SERS active in the environment and it was originally believed that the bulky t-butyl addendum would tend to slow the possible ripening effect[17] of the quantum dots, and protect against oxidation. However, since SERS of 4-tert-butylpyridine adsorbed on silver was not previously reported, and assignments of Raman signal from 4-tert-butylpyridine on QDs were to be based on comparison to the molecule adsorbed on silver, reported in this dissertation for the first time is the normal Raman and SERS of 4-tert- butylpyridine on silver electrode.

Also presented is a brief discussion of the roll of SERS in art.

The experiments conducted during this research not only prove that SERS technique is a very useful tool in characterizing wide bandgap quantum dots, but also reinforce the roll of charge transfer in the overall contribution to Raman enhancement.

1.2 Thesis Structure

The remainder of this thesis is arranged as follows:

Chapter 2 presents a brief definition of a quantum dot and the general MBE growth process involved in fabricating these quantum dots along with the instrumentation and principles involve in AFM of the dots. Also discussed in detail is the concept of Raman spectroscopy and instruments used in the experiment, to the extent of it's application in this research.

Chapter 3 gives a detail description of observation of surface enhancement Raman signal from pyridine molecules adsorbed on a self-assembled CdSe/$Zn_{1-x}Be_xSe$. Also discussed in this chapter is the specific growth process of these fixed bandgap quantum dots and the use of AFM spectroscopy to measure the size and density of the dots. A detail discussion of the results is also presented.

Chapter 4 describes the SERS of 4-tert-butylpyridine on a silver electrode, along with the normal Raman spectroscopy of the neat liquid. Voltage dependency study and a detail discussion of the result is presented.

Chapter 5 presents an in depth study of surface enhancement Raman signal from 4-t-butylpyridine molecules adsorbed on a self-assembled CdSe/ ZnCdMgSe, uncapped quantum dots grown by molecular beam epitaxy (MBE). The effect of varying the quaternary bandgap on Raman signal, by changing the deposition temperature of in

magnesium is also described. Also discussed in this chapter is SERS of biological molecules (adenine, tyrosine, and trytophan) adsorbed on these self-assembled MBE grown quantum dots.

Chapter 6 describes application of Raman and surface enhanced Raman spectra for flavone and several hydroxy- derivatives on silver colloids and silver electrodes. A comparison of use of flavone and it's hydroxy derivatives in textile art is also presented.

.

Chapter 2. Background and Experimental Techniques

2.1 Quantum Dots

A quantum dot is a semiconductor with it's excitons confined in all three spatial dimensions. Figure 1 shows a schematic diagram of the derivation of a quantum dot. We start with a crystal structure, example GaAs crystal, which is defined in three dimensions x, y, z represented in figure 2.1.

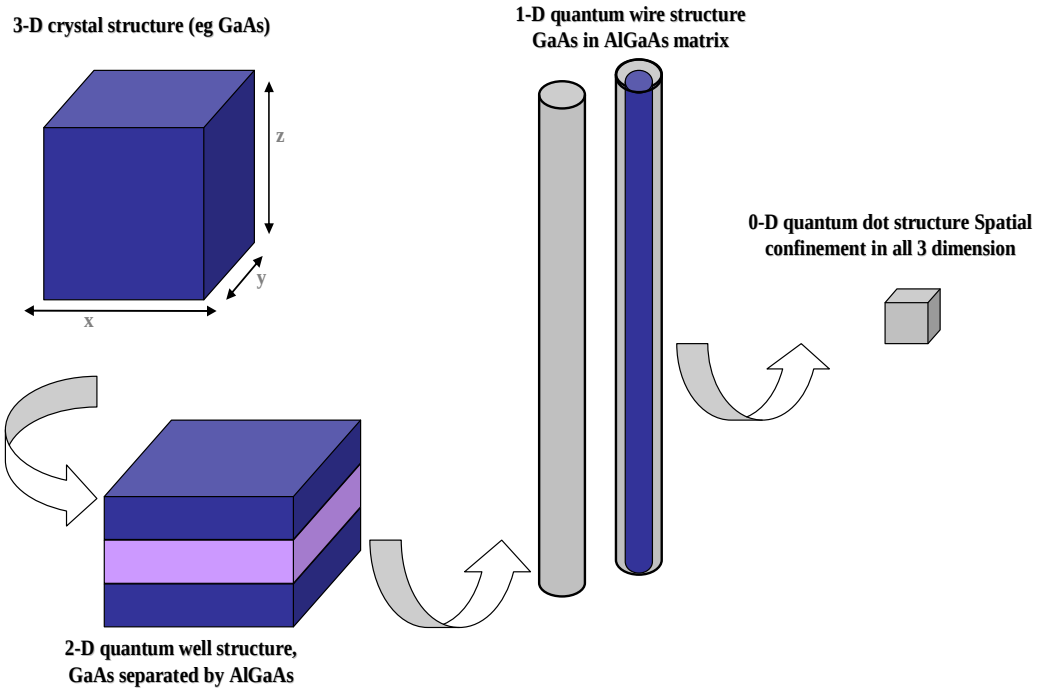

Figure 2.1 showing the schematic derivation of the quantum dot from bulk 3-D structure

This crystal has electrons that are free to move in the conduction band. Decreasing the third dimension (z) until this structure is similar to the wavelength of the electron, results in a confined heterostructure in one dimension. This is the case of a quantum well, for example GaAs well with barriers of AlGaAs. Repeating this process with another dimension, will result in a heterostructure confined in two dimensions, in which the electrons move easily in 1 dimension seen in GaAs quantum wires in a matrix of AlGaAs. Decreasing the third dimension, yield a structure confined in three dimensions. This structure is called a quantum dot.

The physical properties and quantum characteristics of these nanostructures, can be derived by examining the size of the periodic potential when reduced in any dimension to a length (L), where the electron has discrete energy states[18] in this dimension rather than continuous energy bands. The quantum characteristics which these structures posses allows the formation of discrete energy states. Conversely the allowed energy levels in the bulk solid is continuous. This phenomena give rise to quantum confinement of electrons within low dimensional nanostructures. The dependence on energy levels, density of states and wavefunctions for dimensionally confined electrons can be approximated using the particle in a box theory , whose potential is zero (V=0), and increases to infinity outside. The electronic wavefunction of such particle can only have discrete energy levels, corresponding to certain standing wave pattern, and hence the energy levels in this potential well is quantized. Potential profiles of the particle in a box, for these semiconductor hetrostructures materials with different bandgaps, can be simulated by varying the bandgap of these systems. This is evident in the quantum dot which consists of a "caged dot" having a lower bandgap than surrounding semiconductor

matrix. Exitons are confined in the "caged" lower bandgap material by the effective potential well. A modified Bloch's theorem can now be used to describe the states of the electrons and holes in these semiconductor hetrostructures[19], where the particle wavefunction $\psi(\vec{r})$ is the product of a periodic $\mu(\vec{r})$ and envelope wavefunction $\chi(\vec{r})$. This yields the following equation:

$$\Psi(\vec{r}) = u(\vec{r})\chi(\vec{r}) \qquad \text{equation 2.1}$$

Conduction band electrons in the periodic part $\mu(\vec{r})$ of binary nanostructure system such as ZnCdMgSe/CdSe quantum dots, have an s-like wavefunction, while the valency band holes has p-like orbital characteristics. The envelope function in these system $\chi(\vec{r})$ is described using the effective mass approximation

$$\left[-\frac{\hbar}{2m^2}\nabla^2 + V(\vec{r})\right]\chi(\vec{r}) = E\chi(\vec{r}) \qquad \text{equation 2.2}$$

This equation is similar to the Schrodinger equation, where the particle mass is the effective mass m*, the potential describes the band edge or well boundaries (bottom of the conduction band and top of valency band), having carrier energy;

$$E(k) = E(k_x) + E(k_y) + E(k_z) \qquad \text{equation 2.3}$$

The solution of these equation for the electronic wavefunction $\Psi(\vec{r})$ and energy E (k) of the quantum dot with an infinite potential well (particle in a box), yields the following equations:

$$\Psi(\vec{r}) = A(\sin k_x x)(\sin k_y y)(\sin k_z z)$$ equation 2.4 and

$$E(k) = \frac{\hbar^2}{8m_e^{\,2}}\left(\frac{n_x^{\,2}}{L_x^{\,2}} + \frac{n_y^{\,2}}{L_y^{\,2}} + \frac{n_z^{\,2}}{L_z^{\,2}}\right)$$ equation 2.5

where n_x, n_y, n_z = 1, 2,3.....

It should be noted that the wavefunction and energy for the bulk semiconductor can be found from the following equations:

$$\Psi(\vec{r}) = Ae^{i(k_x x + k_y y + k_z z)}$$ equation 2.6 and

$$E(k) = \frac{\hbar^2\left(k_x^{\,2} + k_y^{\,2} + k_z^{\,2}\right)}{2m_e^{\,*}}$$ equation 2.7

The density of sates of these low dimensional quantum dots is given by the following expression:

$$\rho_e(E) = \frac{dN}{dE}\alpha\frac{d}{dE}E^{\frac{3}{2}} = E^{\frac{1}{2}}$$ equation 2.8

and for the bulk semiconductor:

$$\rho_e(E) = \frac{dN}{dE}\alpha\frac{d}{dE}\sum_{\varepsilon_i<E}\Xi(E-\varepsilon_i) = \sum_{\varepsilon_i}\delta(E-\varepsilon_i)$$ equation 2.9

where Θ is the Heaviside step function, ε_i are discrete energy levels and delta (δ) is the Dirac function. These solution shows that reducing the degree of freedom of particle motions in low dimensional nanostructures dramatically changes the density of states in comparison to the bulk material, where the energy exist as a continuum. Quantum dots therefore have discrete energy states and the physical properties of a caged atom.

2.1.1 General Process of MBE Growth

The samples used in the experiments described in Chapters 3 and 5 of this dissertation were grown in a MBE system with two Riber 2300P growth chambers located in The City College of New York Epitaxy Group. Fig 2. 2 shows a schematic view of the system which is composed of 6 chambers: loading, transfer channel, treatment, metallization and two growth chambers (one for III-V materials and the other for the growth of II-VI materials chamber). The transfer channel which connect the chambers, allow materials to move through successive cahmbers while still under ultra high vacuum (UHV).

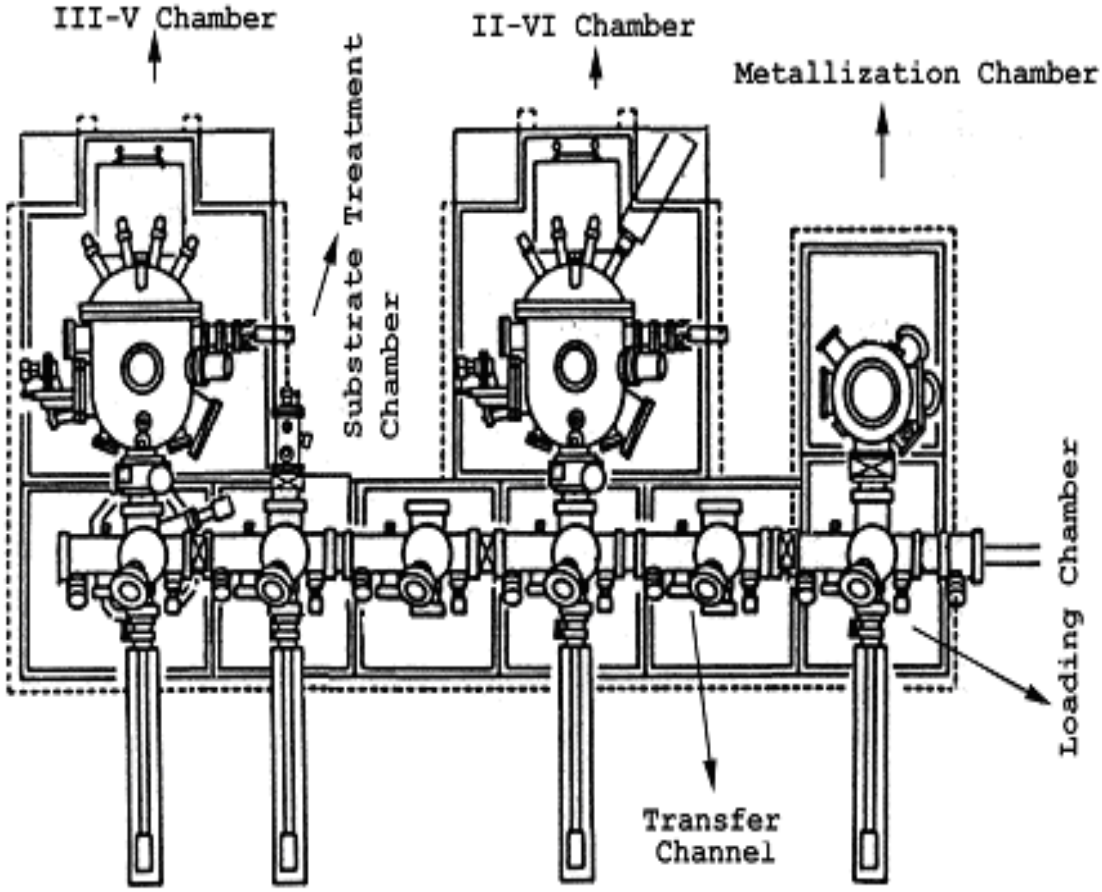

Figure 2.2 showing a schematic diagram of the MBE apparatus used to grow the samples *(courtesy of The City College of New York Epitaxy Group.)*

Prior to MBE growth the substrate used (InP) in the fabrication process is first degreased with trichloroethylene (TCE), acetone and methanol, then etched with a (4:1:1) solution of H_2SO_4:H_2O_2:H_2O, for one minute. The sample is then flushed with distilled water which produces an oxide layer which prevents contamination. In order to facilitate easy loading of the sample in the loading chamber, the substrate is bonded to a molybdenum block using indium. Once the sample is introduced into the loading chamber of the MBE system, two gate valves are closed, locking the sample in the loading chamber where it is vented using pure nitrogen gas, while at UHV (10^{-9} to 10^{-10}). After venting the sample is transferred into the II-V growth chamber where the cell is preheated to the temperature required for the desired flux.

The oxide layer on the substrate is then removed by heating the substrate with an As flux impinging on the surface. The deoxidation process is monitored by use of Reflection High-Energy Electron Diffraction (RHEED), which becomes streaky and bright when the oxide layer is removed. After deoxidation, the substrate temperature is then set to the desired growth temperature and the process begin by opening up the relevant shutters. Since the interest is growth of II-VI structure, a II-V buffer layer which is lattice matched to the substrate is grown to create a smooth substrate surface, prior to the sample being transferred to the II-VI chamber, where the growth process is terminated once the quantum dots are grown. A detail discussion of the growth process in the II-VI chamber will be presented in Chapters 3 and 5.

2.2 Atomic Force Microscopy (AFM)

Atomic Force Microscopy is a scanning probe microscope used to characterize nanostructure surfaces by probing the surface atoms, and record the topographic contours of the surface atoms. Figure 2.3 shows a schematic diagram of the atomic force microscope used in the experiments. The AFM has two scanning modes; contact and non-contact mode. In the contact mode the scanning probe tip is in actual contact with the surface. Associated with this operational mode is the finite size of the probe resulting in tip convolution effect which exaggerate the topography of the image produced[20]. Other difficulties include rapid oxidation of the CdSe quantum dots when exposed to air during the characterization process and damages to the surface of the sample subjected to the probe. A detail description of the use of AFM technique used to characterize the quantum dot surface in the contact mode is discussed in Chapters 3 and 5.

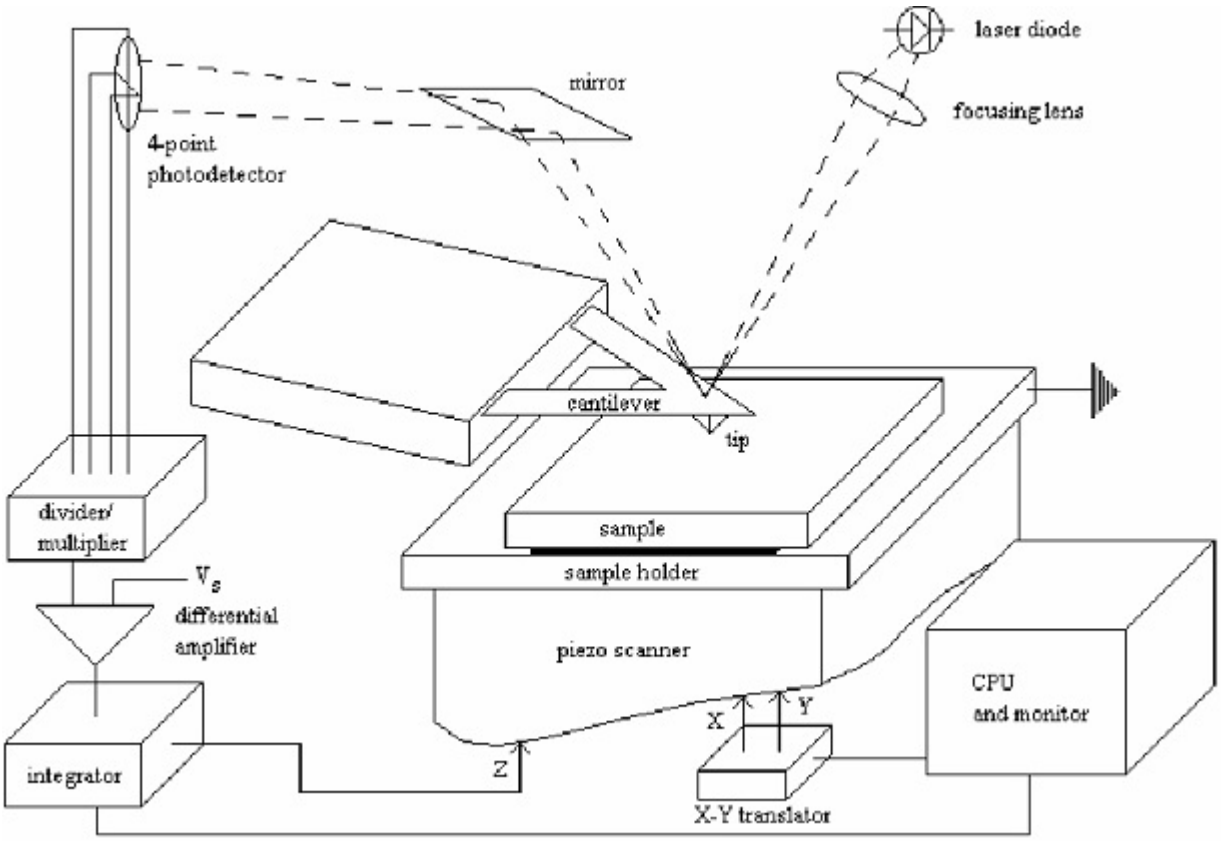

Figure 2.3 Schematic diagram of the atomic force microscope used in experiments.

2.3 Surface Enhance Raman Spectroscopy (SERS)

Since the discovery of SERS in 1974 by M. Fleischmann *et al* [21], this phenomenon has been widely used tool in the exploration of nanoscience. Consequently this immense interest has led to a plethora of publications some of which will be examine in later in this section. In earlier studies it was widely believe that the surface plasmon resonance must be the dominant factor of the large enhancement observed since most of these experiments were done on the noble metal (detail discussion in Chapter 3, 4, 5). However as more research was conducted it was obvious that plasmon theory alone could not explain all the observation made when molecules are adsorbed on metallic surfaces and

soon several researchers[22,23,24,25] proposed a charge transfer mechanism as explanation for this new phenomena. These proposals suggested that the metal conduction band orbitals are located between the highest molecular filled level and it's first excited unfilled layer. This allow transitions from the filled molecular level to empty states above the fermi level. The reverse transitions filled metal levels (below the fermi level) to unoccupied molecular orbitals also occur. This led to the investigation of pyridine and pyrazine on silver in high-resolution electron energy loss experiment, by Demuth *et al*[26] in which low-lying high energy transfer bands were observed. Several attempts using resonance Raman spectroscopy along with plasmon resonance, were then made to explain the additional enhancements observed on these system. These theories had severe limitations however, since it could not be used to explain the lack of overtones and the prominence of non-totally symmetric modes observed in the spectra[27]. The concept of contributions to the overall enhancement from the Herzberg-Teller theory by mixing of the vibronic states, was first pioneered by Albrecht[28] to explain the observe Raman intensities, which Lombardi *et al*[29] later used to successfully combine both molecule to metal and metal to molecule charge transfer in one theory.

It is now worthwhile to highlight some of the recent developments in both experimental and theoretical studies in SERS, on which most of this dissertation was developed.

The SERS concept has seen dramatic expansion in its application to very small sample sizes, which has now been observed at the single molecule level, adsorbed between two silver nanoparticles[30,31,32]. The gigantic enhancement of 10^{14} observe could not be explain by surface plasmon theory since this would include the presence of a very

large electric field on the molecule, which would undoubtedly chemically change the molecule properties. This indicate the presence of charge transfer effect which was also evident in the time-dependent interruptions of the electronic coupling between molecule and nanoparticle, resulting in the blinking effect[33,34], indicative of a resonance enhancement due to silver molecule charge-transfer states[35,36]. Observations of resonant Rayleigh scaterring and single molecule SERS intensity by Michaels *et al*[37], shows no correlations between the two, a strong indication that there are other important effects of SERS other than surface plasmon resonance. Other developments in SERS which shows the importance of a charge-transfer mechanism in the overall enhancement of single molecules, includes the potential dependence and the Stokes/ anti-Stokes ratio on silver electrodes by Brolo *et al*[38]. It is clear from these experiment that large SERS enhancement can be explain by a very small number of molecules when they are located at special Raman active site called "hot spots". This theory was used by Hildebrandt and Stockburger[39] to show that anion activated sites are formed when rhodamine 6G is adsorbed on silver colloid, at extremely low surface coverage, which are responsible for a large portion of the observed enhancement.

The SERS technique recently has expanded to include systems which are far from plasmon resonances hence small resonance contribution are expected . These result are widely documented such as; enhancement observed on silver nanoparticles at 1064nm, far from the silver plasmon resonance[40], enhancement on atomically flat copper surfaces documented by Campion *et al*[41,42], and enhancement observed by Tian *et al*[43,44] on many metals other than transition and noble metals. The remarkable achievement of SERS enhancements on MBE grown quantum dots such as InAs/GaAs[45], CdSe/ ZnBeSe[46] and

CdSe/CdMgZnSe[47] as well as colloidal suspensions; (ZnO and CdTe recently), has produced surprisingly large enhancement factor of up 10^6, typically found on noble metals, where the plasmon resonance lies close to the excitation wavelength. The size of these nanoparticles are smaller than the Bohr radius diameters and hence experience quantum confinement effects, which makes these systems unique in their practical applications, as discussed earlier in section 2.1 and will be discussed in detail in Chapters 3 and 4 for the MBE grown quantum dots.

Another useful development in SERS is the use of density functional theory (DFT) to quickly and accurately determine molecular properties using quantum mechanical calculations, predict the IR and Raman spectrum of large complex molecules and therefore enable accurate assignments of the normal modes of the molecule. Calculations on a pyridine-Ag_{20} cluster by Schatz *et al*[48], pyridine molecule between Ag_{20} junction[49], as well as time-dependent study TD-DFT of Ag_{10}-pyridine complex[50], has enable the distinct separation of the various contributions to the overall SERS enhancement as well as an estimation of the relative contribution. The development of time dependent studies in Raman spectroscopy pioneered by Heller *et al*[51,52] and Lee, has shed new light on previous Raman theory described by Kramers, Heisenberg, and Dirac[53,54], allowing DFT calculations which has been previously restricted to ground state properties to be used in calculations involving excited states. all of which has been incorporated into calculations done by Schatz et al[48], Birke et al[50] and other investigations currently been undertaken in this area of SERS.

The fact that plasmon resonance contribution to SERS is limited in its explanation to the enhancement observed on various substrate such as semiconductor nanoparticles,

means that it is now important to show how the contributions to totally symmetric and non-totally symmetric bands vary if the system being analyzed is in a region of charge transfer or molecular resonance. Since these conditions are typical of semiconductor quantum dots and will be crucially important to the explanation of experimental result and discussed in this dissertation, a quantitative treatment will now be used to show how the different contributions from surface plasmon resonance and charge transfer resonance affect the total contribution to the overall Raman intensities.

The intensity of light scattered for Raman transition between two states $|I\rangle$, and $|I'\rangle$ of a scattering system is given by;

$$I = [8\pi(\omega \pm \omega_{I'I})^4 I_L / 9c^4] \sum \alpha_{\sigma\rho}{}^2 \qquad \text{equation 2.10}$$

where I_L is the incident laser intensity at frequency ω; $\omega_{\Gamma L}$ is the frequency of the Raman transition $|I\rangle \leftarrow |I'\rangle$, and $\alpha_{\rho\sigma}$ is the transition polarizability tensor. Second order pertubation theory gives the following expression for the polarizability;

$$\alpha_{\sigma\rho} = \sum_{S \neq I,I'} \left\{ \frac{\langle I|\mu_\sigma|S\rangle\langle S|\mu_\rho|I'\rangle}{E_S - E_I - \hbar\omega} + \frac{\langle I|\mu_\rho|S\rangle\langle S|\mu_\sigma|I'\rangle}{E_S - E_I + \hbar\omega} \right\} \qquad \text{equation 2.11}$$

where μ_ρ and μ_σ are the dipole moment opertors on ρ and σ, the scattered and incident polarization directions respectively. This expression also shows that the two different dipole moment matrixes must be non-zero simultaneously for a Raman transition to occur. The zero-order adiabatic Born-Oppenheimer approximation shows that the vibronic states (I, I', S) is a product of the electronic and vibrational wavefunction: $|I\rangle = |I_e\rangle|i\rangle$, $|I'\rangle = |I_e\rangle|f\rangle$; and $|S\rangle = |S_e\rangle|k\rangle$; e is the purely electronic state and all lower case letters are the vibrational functions. The Born-Oppenheimer

condition is valid when the electronic transition moment is a weakly varying function of the nuclear coordinates. The Herzberg-Teller treatment is also valid under this condition of weak vibronic coupling and can be used to derive an expression for $\alpha_{\sigma\rho}$ as shown by Albrecht[55]:

$$|S\rangle = |S_{e'}0\rangle + \sum \lambda_{SR} Q |R_{e'}0\rangle \qquad \text{equation 2.12}$$

$$\lambda_{SR} = h_{SR}/(E_R^0 - E_S^0) \qquad \text{equation 2.13}$$

$$h_{SR} = \langle S_{e'}0|(\partial V_{eN}/\partial Q)_0|R_{e'}0\rangle \qquad \text{equation 2.14}$$

This derivative involves three terms A, B, and C and the electron-nuclear attraction term V_{eN} in the Hamiltonian is evaluated with respect to the equilibrium nuclear positions. The purely electronic transition moment between states can be express as $\mu^{\sigma}{}_{SI} = \langle S_e | \mu^{\sigma} | I_e \rangle$, $\mu^{\sigma}{}_{RI} = \langle R_e | \mu^{\sigma} | I_e \rangle$, and $\mu^{\sigma}{}_{SR} = \langle S_e | \mu^{\sigma} | R_e \rangle$.

Lombardi *et al*[29,56] applied these expression to SERS, assuming the molecule is bound to the metal surface by a weak covalent bond and the molecule-metal system is treated as a whole system in the calculations. This implies that the A,B and C terms derived in the Albrecht expression includes the metal conduction band M. Albrecht also shows that the appearance of forbidden bands in the optical spectra is due to intensity borrowing from the same allowed transition[57,58]. Thus uncoupling of the metal-molecule complex implies that charge-transfer transitions are forbidden. The second order breakdown of the Born-Oppenheimer approximation, on coupling will allow intensity borrowing from allowed molecular transition μ_{KI} by molecule to metal transition μ_{IM}, via the Herzberg-Teller coupling term h_{MK}. This can also occur via metal-molecule

transition μ_{MK} through Herzberg-Teller coupling h_{IM}. Summing over all excited states of M for the charge transfer contribution and substituting the Herzberg-Teller mixing of vibronic coupling, (equations 2.12 - 2.14) into equation 2.11 gives the Albrecht expressions for the molecule metal system;

$$\alpha_{\sigma\rho} = A + B + C$$

equation 2.15 where,

$$A = \sum_{S=F,K\neq I} \sum_{k} \left[\frac{\mu_{SI}^{\sigma}\mu_{SI}^{\rho}}{\hbar(\omega_{SI} - \omega)} + \frac{\mu_{SI}^{\rho}\mu_{SI}^{\sigma}}{\hbar(\omega_{SI} + \omega)} \right] \langle i|k\rangle\langle k|f\rangle$$

$$B = \sum_{R=F,K} \sum_{S=F,K} \sum_{k} \left[\frac{\mu_{IR}^{\sigma} h_{RS} \mu_{SI}^{\rho}}{\hbar(\omega_{KI} - \omega)} + \frac{\mu_{IR}^{\rho} h_{RS} \mu_{SI}^{\sigma}}{\hbar(\omega_{KI} + \omega)} \right] \frac{\langle i|k\rangle\langle k|Q_k|f\rangle}{\hbar\omega_{KS}}$$
$$+ \sum_{R=F,K}{}' \sum_{S=F,K}{}' \sum_{k}{}' \left[\frac{\mu_{IS}^{\sigma} h_{SR} \mu_{RI}^{\rho}}{\hbar(\omega_{RI} - \omega)} + \frac{\mu_{IS}^{\rho} h_{SR} \mu_{RI}^{\sigma}}{\hbar(\omega_{RI} + \omega)} \right] \frac{\langle i|Q_k|k\rangle\langle k|f\rangle}{\hbar\omega_{RS}}$$

$$C = \sum_{R=F,K} \sum_{S=F,K} \sum_{k} \left[\frac{\mu_{IR}^{\sigma} h_{IS} \mu_{SK}^{\rho}}{\hbar(\omega_{RI} - \omega)} + \frac{\mu_{IK}^{\rho} h_{IS} \mu_{SR}^{\sigma}}{\hbar(\omega_{RI} + \omega)} \right] \frac{\langle i|k\rangle\langle k|Q_k|f\rangle}{\hbar\omega_{SI}}$$
$$+ \sum_{R=F,K} \sum_{S=F,K} \sum_{k} \left[\frac{\mu_{SR}^{\sigma} h_{IS} \mu_{IR}^{\rho}}{\hbar(\omega_{RI} - \omega)} + \frac{\mu_{SR}^{\rho} h_{IS} \mu_{IR}^{\sigma}}{\hbar(\omega_{RI} + \omega)} \right] \frac{\langle i|Q_k|k\rangle\langle k|f\rangle}{\hbar\omega_{SI}}$$

Assuming the frequency of the exciting light is far from molecular resonance of any states ($\omega \angle \omega_{IK}$) the frequency dependent terms in all expression A, B, and C in equation 2.15) can be discarded for the summation over all vibrational states k. Application of the closure relation $\sum |k\rangle\langle k| = 1$ to the A term in equation 2.15 shows that $\sum (i/k\rangle\langle k/f\rangle) = \langle i/f\rangle$. In this case the harmonic oscillator approximation disappears, hence the A term in the expression contributes only to Rayleigh line and the B and C terms are the only contributors to the overall surface enhanced Raman intensity.

Examination of the charge-transfer and molecular resonances in which the exciting light is resonant with the surface plasmon and also a charge transfer transition in the molecule-metal system, the expressions in equation 2.15 contains a charge transfer state F. Detail analysis of these expressions[29,56] shows two A terms; A_f and A_k. A_f represents resonant molecule- to- metal charge transfer from the molecular ground state to one of the unfilled metal levels M. A_k is a metal-molecule charge transfer from a filled metal state to an excited state K. Therefore the A_f and A_k terms are associated with resonant Raman spectroscopy. It should be noted that these terms also proves that far from resonance, the numerator in the expressions disappears, while only the totally symmetric modes are seen while on resonance both symmetric and non-totally symmetric modes are found in the SERS, the B and C terms which predicts both must be considered.

Examination of the metal-molecule charge transfer expression in C shows that the corresponding molecule to metal transfer can be express in a single equation

$$R_{IFK}(\omega) = \frac{\mu_{KI}\mu_{FK}h_{IF}\langle i|Q_k|f\rangle}{((\epsilon_1(\omega)+2\epsilon_0)^2+\epsilon_2^2)\left((\omega_{FK}^2-\omega^2)+\gamma_{FK}^2\right)\left((\omega_{IK}^2-\omega^2)+\gamma_{IK}^2\right)}$$

equation 2.16

where; $|R_{IFK}(\omega)|^2$ is proportional to the SERS total enhancement factor. The first term in the denominator $\left(\left(c_1(\omega)+2c_0\right)^2+{c_2}^2\right)$ arises from plasmon resonance at $c_1(\omega) = -2c_0$; the second term is a Fermi energy dependent resonant representing a charge transfer resonance occurring at $\omega = \omega_{FK}$. This term is significant for electrochemical SERS, where the C term predicts a positive applied voltage at resonance.

The final term in the denominator $(\omega_{IK}{}^2 - \omega^2) + \gamma^2{}_{IK}$ gives the molecular resonance $\omega = \omega_{IK}$ resulting in surface enhanced resonance Raman spectroscopy (SERRS), typically observed in single moecule experiments.

Careful examination of the numerator which provides the SERS selection rules, shows all four terms connected with each other. The Herzberg-Teller contributes a product of h_{IF} containing $\langle i|\ Q_K\ |f\rangle$ in this expression having normal mode Q_K. This requires normal harmonic oscillator selection rules and implies that only normal modes for which $\langle i|\ Q_K\ |f\rangle \neq 0$ will be observed. Hence, both overtones and non-totally symmetric vibrational lines are not observed normally. The other terms $\mu_{KI}\mu_{FK}$ are allowed molecular transition $\mathrm{I} \rightarrow \mathrm{K}$, metal-molecule charge transfer $\mathrm{F} \rightarrow \mathrm{K}$, which depend on the orientation of the molecule with respect to the metal.

The Herzberg-Teller surface selection rules for metal-molecule charge transfer can be express as;

$$\mu^{\sigma}{}_{KI}\mu^{\rho}{}_{FK}h_{IF} = \langle I_g|\mu^{\sigma}|K_e\rangle\langle K_e|\mu^{\rho}|F_e\rangle\langle F_e|\partial V_{eN}/\partial Q_k|I_g\rangle$$ equation 2.17,

and show that for appreciable SERS intensity to occurr, all three terms must be simultaneously non-zero. This imposes a rigid test for the Herzberg-Teller theory. However simplifying the selection rules in equation 2.17 by considering only symmetry species of the operators involve gives:

$$\Gamma(Q_k) = \sum_K \Gamma(\mu_{CT}^{\perp}) x \Gamma_K$$ equation 2.18.

where $\Gamma(Q_K)$ is the irreducible representation which SERS vibration is allowed, $\Gamma(\mu_{CT}{}^{\perp})$ is the irreducible representation where the charge transfer dipole component is

perpendicular to the surface and Γ_K is the irreducible representation of the molecular excited states corresponding to the allowed optical transition $I \rightarrow K$. Intensity borrowed by charge-transfer contribution to SERS intensity can be measured from the following equation:

$$\rho_{CT}(k) = \frac{I^k(CT) - I^k(SPR)}{I^k(CT) + I^0(SPR)} \qquad \text{equation 2.19}$$

where k is an index used to identify molecular lines in the spectrum. The intensity of two reference lines obtained in a spectral region in which there is no charge transfer contribution is needed. One of these is $I^{K}(SPR)$ is the intensity of one of these lines (k), in question taken where only the SPR contributes to the SERS intensity where only SPR contributes to the SERS intensity. The other reference is a chosen totally symmetric line, also measured with only contributions from SPR, denoted by $I^{O}(SPR)$. $I^{K}(CT)$ is the measured intensity of the line (*k*) in the region of the spectrum in which the charge transfer resonance makes an additional contribution to the SERS intensity. Thus for a totally symmetric line $I^{K}(SPR) = I^{O}(SPR)$ and in the case of a non-totally symmetric line $I^{K}(SPR) \rightarrow 0$. Therefore in equation 2.19 if ρ_{CT} is zero there will be no charge transfer contribution to the spectrum, however as ρ_{CT} increases to one, the charge transfer contribution will dominate. When ρ_{CT} = 1/2 the surface plasmon and charge transfer contribution to the spectrum are equal. This quantitative treatment of the contributing components of charge transfer transition in SERS will now be applied pyridine molecules adsorbed on fixed bandgap semiconductor quantum dots.

Chapter 3. Surface Enhanced Raman Spectroscopy of Pyridine on CdSe/ZnBeSe Quantum Dots Grown by MBE

3.1 Introduction

Nanostructures are of special interest in the field of semiconductors, where they display discrete, atom-like valence (hole) and conduction (electron) levels due to quantum confinement effects[59]. Quantum dot assemblies are regarded as likely building blocks for novel electronic as well as photonic devices. Both a single-electron transistor[60] and a light emitting diode[61] have been constructed from arrays of CdSe quantum dots. Quantum dots have also found application in the field of biosensors[62,63]. In order to assess the characteristics of quantum dot surfaces and their value in the field of sensing, we must develop techniques for observation of the details of the molecule-surface interaction. A high resolution, non-destructive probe is needed. Absorption and emission spectroscopy are of limited resolution, due to the rather broad line-widths obtained. A preferable technique is that of Raman spectroscopy, which has proven invaluable for detection and identifying important molecules.

Normally Raman scattering from molecules adsorbed on surfaces is too weak to be detectable. In order to overcome these problems, surface enhanced Raman scattering (SERS) has been found to be of value in surface and interface Raman studies in metals. The SERS effect is characterized by an enormous increase in the Raman intensity by many orders of magnitude for species adsorbed on rough metal surfaces compared to that obtained from the same number of molecules in solution or the gas phase[64,65,66,67]. Additionally fluorescence, which often obscures Raman spectra, is suppressed on a surface. Typical enhancement factors obtained on a roughened Ag surface are on the

order of 10^6. SERS on metal substrates has been shown to arise from a product of surface plasmon and charge transfer resonances[68,69]. Electromagnetic theories predict that the electric field at the metal surface becomes very large when excitation takes place within surface plasmon resonances of the metal nanoparticles. Additional contributions to the enhancement are obtained when the excitation frequency is in resonance with a charge-transfer transition of a specific adsorbate-metal complex.

SERS provides a number of important advantages: sensitivity, selectivity, non-destructive detection, and feasibility for *in-situ* studies. It often allows detailed information as to the nature and orientation of the adsorbed molecule, not to mention effects of adsorption on the molecular force field. Remarkable work has been carried out recently on rhodamine 6G (R6G)[70,71] by observing giant Raman enhancements (estimated at 10^{14}) on small, single Ag nanoparticles and nanowires[72]. Until now, SERS experiments have been essentially restricted to adsorbates on rough metallic surfaces, especially noble and alkali metals. Reports describing SERS experiments on non-coinage metal surfaces are available[73,74,75].

In a recent work[76,75] we have reported a successful application of surface enhanced Raman spectroscopy to surface characterization of semiconductor materials by using two different methods. The first consists of coating the semiconductor surface with a silver island film. The second method is based on the use of a chemical etching process. With both SERS-activation procedures the surface roughness plays a crucial role in obtaining very large enhancement of the Raman signal.

More recently we have observed SERS from III-V (InAs/GaAs) semiconductor quantum dots[77]. This suggests a technique for sensitive, high-resolution

study of the interaction of adsorbate molecules with quantum dot surfaces. Pyridine (C_5H_5N) was chosen as probe molecule for these SERS studies because its Raman spectrum is sensitive to the environment. A lower enhancement factor of approximately 10^3 was measured with a very sophisticated method utilizing a microscope attached to the Raman apparatus. This method under-estimated the enhancement factor, but was very useful to prove the existence of SERS on semiconductors.

Surface enhancement has been also observed on semiconductor nanoparticles in colloidal suspensions such as CdS[78], ZnS[79], ZnO[80], CuO[81] and CdTe[82]. These systems have displayed enhancement factors ranging from 10^2 to 10^4. The reason these enhancement factors are so much lower than that of Ag is most likely due to the fact that the surface plasmon excitation frequency for semiconductors is quite far from the laser excitation. These considerations lead us to examine whether we can obtain higher degrees of surface enhancement due to CdSe quantum dots using excitation energy in the excitonic region of these systems.

Reported in this disssertation is the observation of surface enhancement of a Raman signal from pyridine molecules adsorbed on a self-assembled CsSe/$Zn_{1-x}Be_xSe$, (with x = 0.03 which allows near lattice match between the GaAs and the ZnSe layer) uncapped quantum dots grown by molecular beam epitaxy (MBE). Using laser excitation at 488 nm, chosen to be in a region of QD absorption, we have found a large enhancement factor, and by detailed analysis of the observed Raman spectra, we can obtain information as to the orientation of the molecule with respect to the surface. Furthermore, the high degree of spectral selectivity, coupled with the high sensitivity

afforded by the rather large enhancement factors, makes such systems good candidates for possible use in detecting and identifying SERS active molecules.

3.2. Experimental

3.2.1 Molecular Beam Epitaxial Growth of Samples (NP)

The quantum dot (QDs) assemblies were grown by MBE on GaAs (001) substrates in an ultrahigh vacuum (UHV) Riber system that has two connected growth chambers, one dedicated to III-V materials and another to II-VI materials. The entire growth process was monitored in situ by reflection high-energy electron diffraction (RHEED)[83]. In order to achieve a flat growth surface for the QD formation, first, the oxide layer of the GaAs substrate is removed by heating the substrate with an As flux impinging on the substrate surface. This was followed by the growth of a 200-nm GaAs buffer layer, 30 periods of 2-nm GaAs/2-nm AlAs short-period superlattice, and a 30-nm GaAs layer, all grown at 580 ^{0}C. The substrate with the III-V buffer layer was then transferred to the II-VI chamber in UHV. In order to avoid the formation of Ga_2Se_3, which is related to the formation of stacking faults[84] along the III-V/ II-VI interface, the GaAs surface was exposed to a Be/Zn flux at 170 ^{0}C during 20 seconds. The substrate temperature was then increased to 250 ^{0}C and a 6nm ZnSe buffer layer was grown. This was followed by the growth of ZnBeSe epilayers (94nm) at 270 ^{0}C. The CdSe quantum dots were formed on the ZnBeSe surface by depositing 2.5 mono layers (MLs) of CdSe at a temperature of 320 ºC followed by a growth interruption time of 26 s. After this, the sample was cooled to room temperature. To slow a possible ripening effect[85], the samples were immediately cut into smaller rectangles (approximately 3mm), immersed in liquid

nitrogen after growth and kept in this condition until the moment of taking the surface topography or Raman spectra.

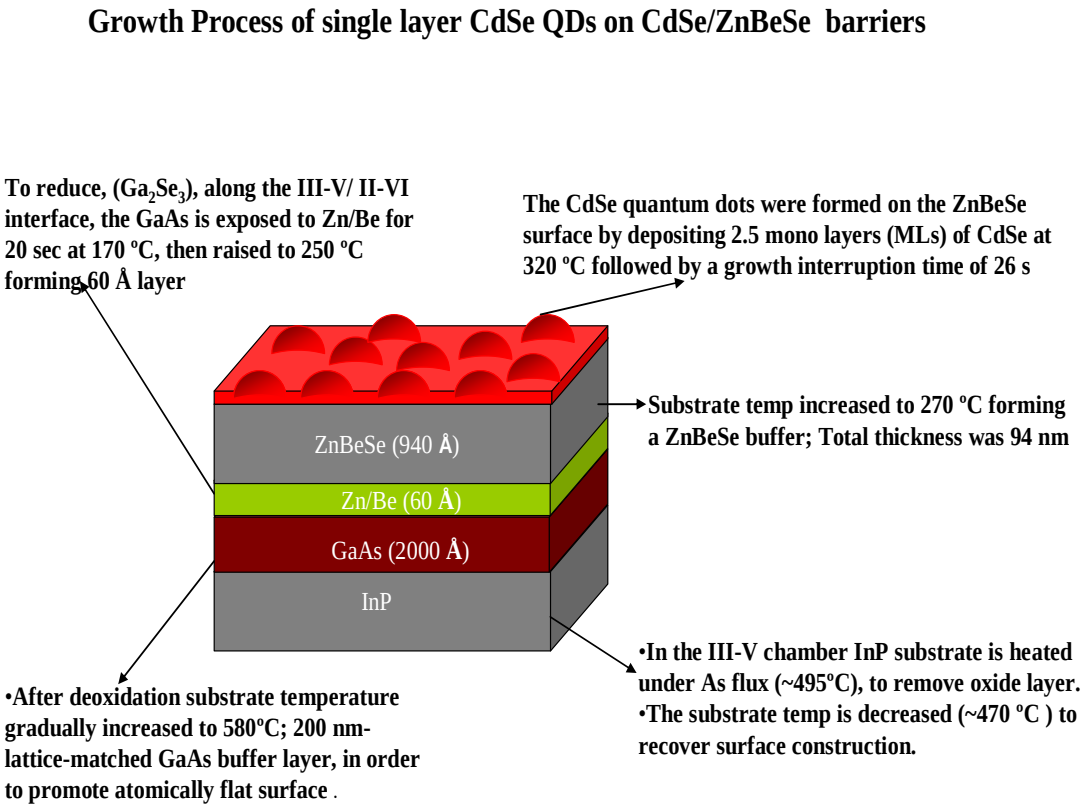

Figure 3.1. Schematic diagram showing the MBE growth process of CdSe/ZnBeSe Quantum Dots

3.2.2 Raman Spectroscopy

A stock solution of commercial pyridine was prepared at 1mM concentration in deionized-distilled water. One of the cut pieces of the quantum dot samples were then removed, allowed to attain room temperature conditions, and then immersed in a small portion (10ml) of the liquid pyridine for 20 minutes. The sample was sonicated in

commercial acetonitrile solution for 5 minutes to remove excess liquid and mounted near the entrance slit of a SPEX (0.75 meter) model 1401 double monochromator. Light from a Spectra Physics Model 2560 argon ion laser was filtered to remove interference from plasma lines and focused on to the sample with 10μm spot size. The scattered Raman emission, which is reflected at 90° from the sample, was collimated using a collecting lens and focused onto the slit of the spectrometer. The slit widths were set at 150μm, providing a resolution of about 3 cm^{-1}.

All spectra reported below were taken at 488 nm. Typical power levels at the sample were measured to be approximately 30 mW.

3.2.3 Atomic Force Microscopy

Atomic Force Microscope (AFM) images were recorded in non-contact mode using a ThermoMicroscopes Explorer™ system (Veeco Instruments, Santa Barbara, CA, USA), operated in air and at room temperature. Silicon microfabricated cantilevers (Veeco nano-probe tips Model # 1650-00) possessing a spring constant of 13-100 N/m and a resonance frequency of 260 kHz were used. The integral and proportional gains ranged between 0.5 and 1.2, figures 3.2 and 3.2a. Images were recorded in the range of 5x5 μm with a 300 x 300 pixel resolution and a scan rate of 3.69 μm/s. The microscope was placed on a pneumatic anti-vibration table, under a damping cover. The processing was conducted using the SPMLab software.

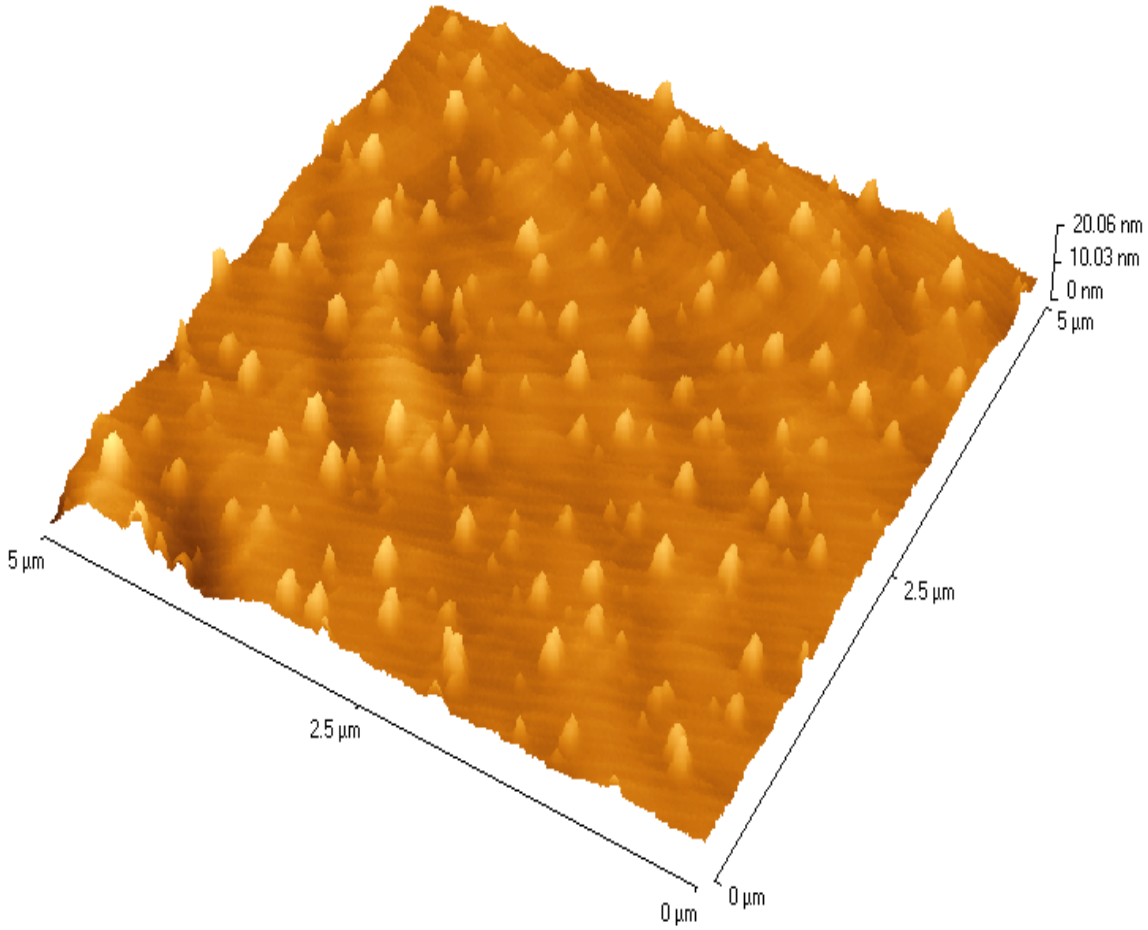

Figure 3.2a. 3D representation of an AFM image of the quantum dots

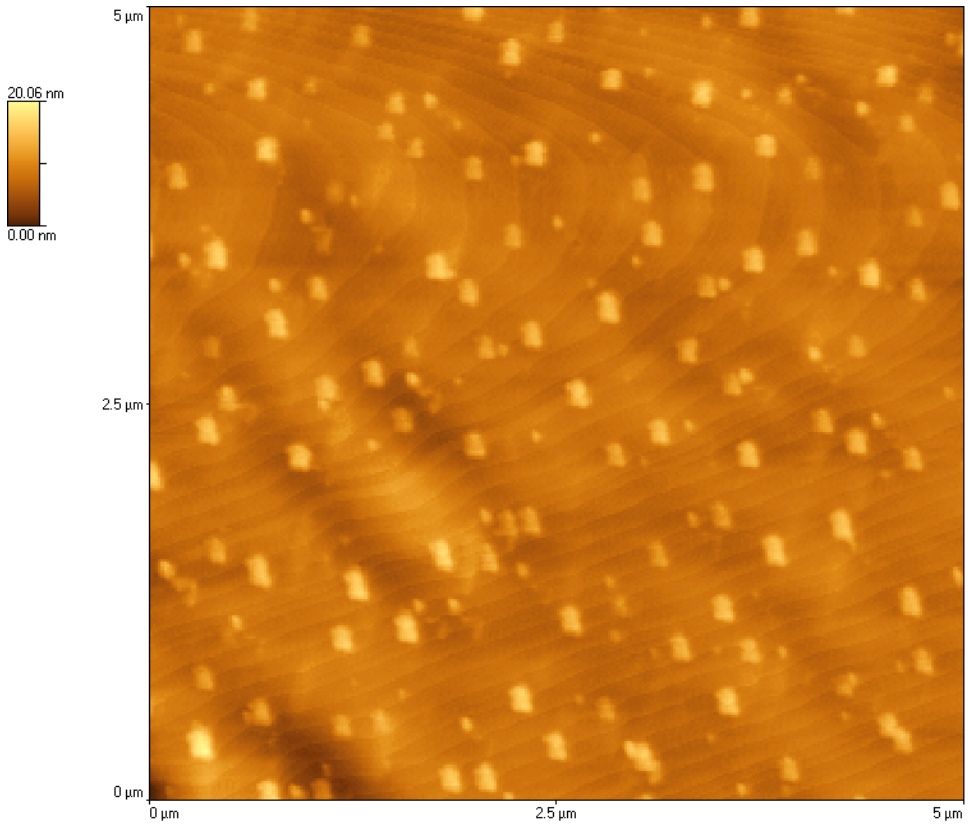

Figure 3.2. AFM image of quantum dots

3.3. Results

The atomic force micrograph images (figure 3.2) of surface of similar samples grown under identical conditions[86] indicate that the average height of a dot is 12 nm, while the dot radius is approximately 35 nm., which indicates that they have a hemi-ellipsoidal shape rather than spherical or hemispherical. The surface quantum dot density is 1.5×10^{9} cm^{-2}. Contactless electroreflectance (CER) studies[87] on similar samples, in which the quantum dots are capped by another ZnBeSe layer, provide evidence for a thin wetting layer. The total amount of deposited CdSe is nominally 2.5 ML. Calculation of the volume of the quantum dots indicates that the wetting layer is approximately 1.0-1.5

ML and this is consistent with the CER studies. The remainder forms the hemi-ellipsoid quantum dots.

In figure 3.3, we show the Raman spectrum of the quantum dot sample, coated with pyridine molecules, excited at 488 nm in the region of 550-1250 cm^{-1}.

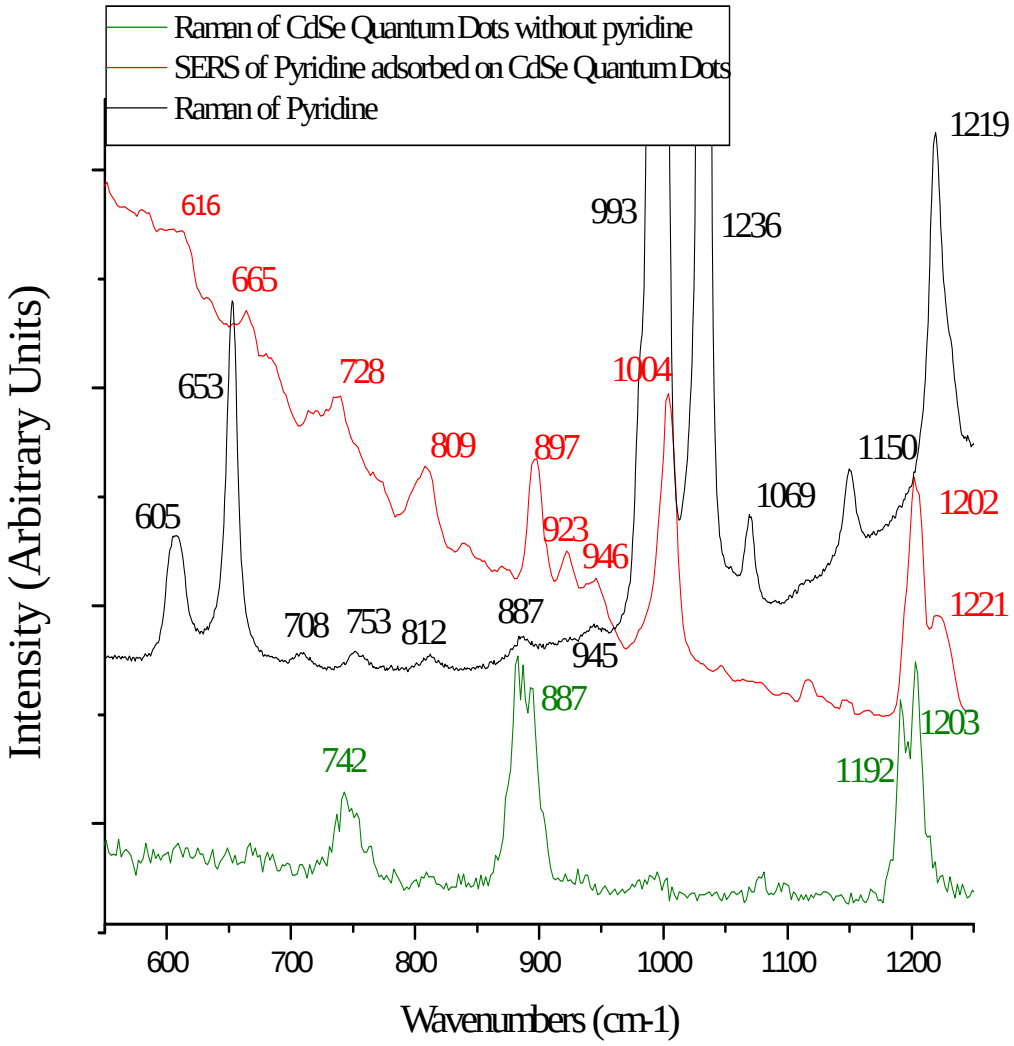

Fig 3.3: Normal Raman and SERS spectrum of pyridine on Ag and CdSe quantum dots excited at 488 nm. For reference the spectrum of bare quantum dots is also shown

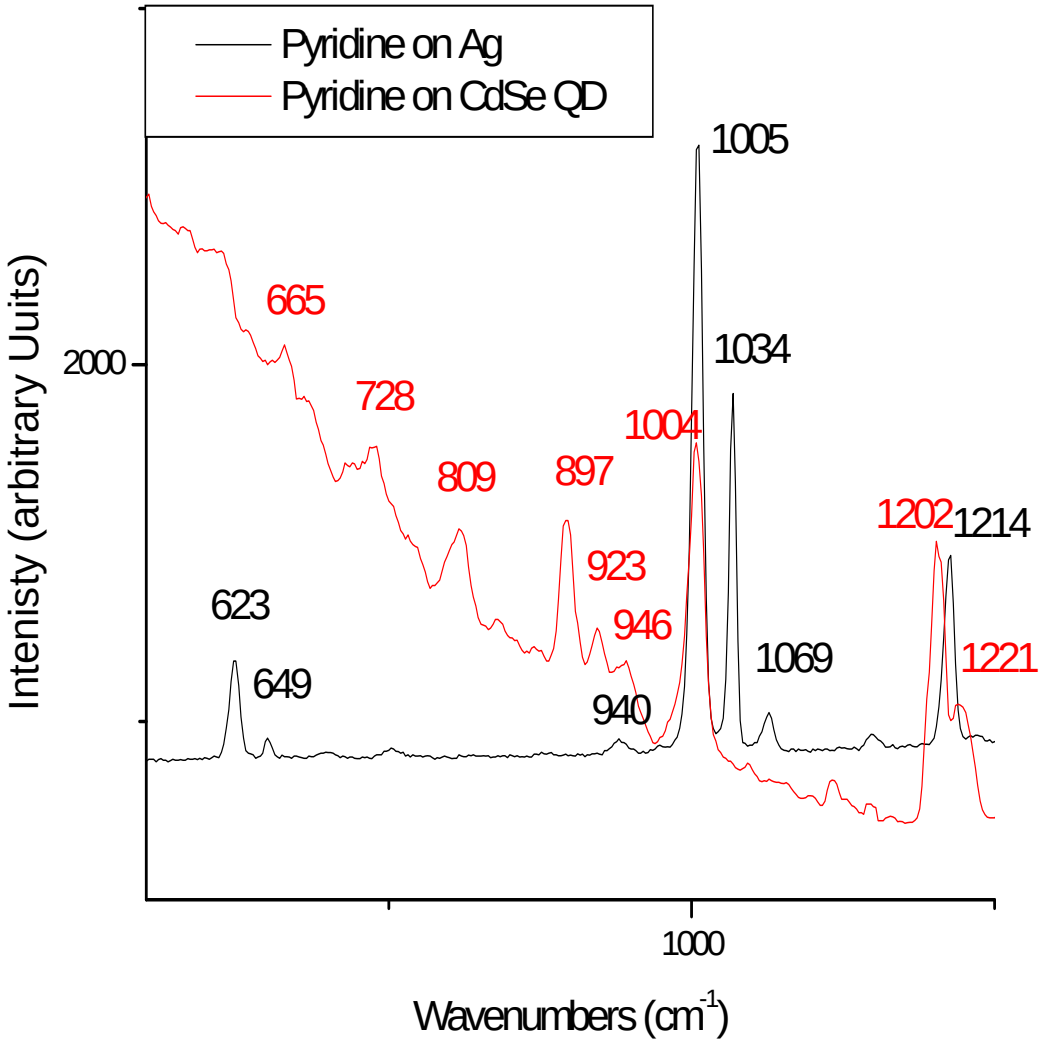

Figure 3.4 SERS spectrum of pyridine on CdSe and Ag

Measured wavenumbers are listed in table 3.1. Since the Raman spectra arise from surface coating of at most, one monolayer of the molecule, it is clear that the molecular spectral lines are considerably enhanced by proximity to the quantum dots. When the same experiment was carried out after depositing pyridine on the bare ZnBeSe layer without quantum dots deposited, no lines due to this molecule could be observed. This

was also the result when pyridine was adsorbed on a thick layer of CdSe which has no quantum dots deposited on the ZnBeSe layer .

Figure 3.4 shows the SERS spectrum of the pyridine molecules adsorbed on the CdSe quantum dots, together with the Raman spectrum of the quantum dots sample before the deposition of the molecule and the Raman spectrum of the pyridine solution. Numerous lines characteristic of pyridine appear, as can be seen by comparison with the normal Raman spectrum of pyridine liquid. These are listed in the table, along with the lines observed on Ag (figure 3.4). We also present a brief summary of the assignment of the normal modes[88] of pyridine, including their Wilson number and symmetry in C_{2v}. On the quantum dot surface most of the lines correspond to lines previously observed either in the liquid or on a Ag surface. Note that in addition to the expected enhancement of several a_1 modes (616, 897, 1004, 1221 cm^{-1}), the bands at 665 (b_2), 728 (b_1), 923 (b_1) and 946 (b_1) $cm^{-1}$are also considerably enhanced relative to the liquid spectrum. The line at 728 cm^{-1}suffers from interference from the bare quantum dot line at 742 cm^{-1}, and should therefore be considered questionable. The same is true for the a_1 line at 897 cm^{-1}, while the line at 1221 cm^{-1} is sufficiently distinct from the QD line at 1203 cm^{-1} to be acceptable. The observation of relatively intense non-totally symmetric modes is usually diagnostic of a charge-transfer contribution to the observed enhancement, most probably from the quantum dots to the molecule[89]. Intensity borrowing from the low-lying $^1B_1$ and $^1B_2$ transitions in pyridine is likely.

Wilson #	C_{2v} Symm	Pyridine Liquid	SERS Pyridine on Ag	SERS Pyridine on CdSe QDs
6a	a_1	605(vw)	623(mw)	616(w)
6b	b_2	653(w)	649 (w)	665(m)
11	b_1	708	698	715(w)
4, QD	b_1	753	753(w)	728(m)
		812		809(m)
10a, QD	a_1	887	877(vw)	897 (s)
10b	b_1	942		923(w)
17b	b_1	945	940 (w)	946 (w)
1	a_1	993(vs)	1005(vs)	1004(vs)
12	a_1	1034(s)	1034(s)	
18a,18b	a_1,b_2	1069	1063(w)	
15	b_2	1150	1148(vw)	
QD				1202
9a	a_1	1219	1214(m)	1221(s)

Table 3.1: Pyridine lines as observed in Normal Raman, SERS on a Ag surface and on CdSe/ZnBeSe self-assembled quantum dots.
Lombardi, J.R.; Birke, R.L Foucault R; Vivoni A, J.Phys.Chem. B, 2003, 107, 5547-5557.

3.4 Discussion

The observed Raman spectrum shows several differences from the normal Raman spectrum, and is closer in some ways to the SERS observed on Ag nanoparticles. Among other things, the prominence of non-totally symmetric lines (table 1) indicates the importance of charge-transfer contributions to the overall enhancement. In Ag

nanoparticle SERS, both the charge-transfer and surface plasmon resonances have been shown to be responsible for the effect. However, in semiconductors, the excitation wavelengths are far from the region of surface plasmon resonance for CdSe and so the magnitude of enhancement must be attributed to other possible resonances. We suggest that one contribution is likely a charge transfer resonance between the molecule and the quantum dot. A previous study of molecules on ZnO quantum dots[90] showed that a size dependent resonance could be observed, and that a surface-bound ionized acceptor-exciton complex[91] was implicated in the mechanism. This mechanism has since been proven[92], and it is highly suggestive here as well. In addition, in the CER spectrum[93] at room temperature for the CdSe/ZnSe QD structure there are several interband or excitonic transitions in the quantum dot in the optical region, which may be assigned to peaks observed near the laser excitation at 2.54 eV. These interband transitions are at 2.32 eV (QD_0) and 2.46 eV (QD_1), corresponding to the CdSe/ZnSe QDs and 2.56 eV correponding to the CdZnSe wetting layer. The band gap energy for the bulk CdSe is approximately 1.6 eV. The laser excitation energy is closest to the wetting layer transition. However, we cannot rule out the possibility that one or more of the quantum dot transtitions are excited by the laser. The closest is the QD_1 transition, which has been assigned as the $|1,1>_e \rightarrow |1,1>_{hh}$ transition (for |N,M> the M denotes the z component of the angular momentum, N the level designation). It may also be that our distinction between wetting layer and quantum dot is larger than should be, and since they may be regarded as parts of the same strain-induced surface system. Alternately, the excitation attributed to the wetting layer in the CER spectrum could easily be transferred to the quantum dots, thus erasing the distinction altogether.

3.4.1 Calculation of the Enhancement Factor

It is now worthwhile to estimate the enhancement factor. As mentioned previously, typical enhancement factors for roughened Ag are on the order of 10^6-10^7, but under some circumstances have been observed to be as large as 10^{14}. The enhancement factor (E_F) is the ratio of Raman intensity per adsorbed molecule divided by that of the free (or solid phase) molecule and may be determined by the relationship:

$$E_F = I_{surf}N_{sol}/I_{sol}N_{surf}$$

Where I and N are the intensities and number of molecules on the surface and in the solution. We consider a surface which is composed of two parts, one a wetting layer of roughly 7.1 Å thickness, covered by a layer of hemi-ellisoidal quantum dots. The dots have a height of 12 nm and a radius of 35 nm. These two components of the surface are most likely to possess different properties with respect to the adsorbed molecule, since they are clearly different in structure. However, it is impossible at this stage to determine whether the observed signal is from molecules adsorbed on the quantum dots, or on the wetting layer. Consequently we will take into account both possibilities.

We take for our intensity measurements the 993 cm^{-1} line of pyridine. This line was chosen because it is moderately intense when compared to the other spectral lines, and well separated from its neighbors. After subtraction of the background intensity, the intensity in the normal Raman spectrum of this line is about 950 counts, while from the surface enhanced quantum dot spectrum, we obtain about 1440 counts. In both spectra the laser intensity and focus was kept the same. The intensity ratio (I_{surf}/I_{sol}) is therefore approximately 1.52. Using the probe spot size of the laser which is 10µm in diameter, the

path length in the liquid of about 1 cm, and the concentration of 0.01M pyridine of 6.0 x 10^{18} molecules/cm^3 we determine that N_{sol} is 4.7 x 10^{12} molecules. In order to determine N_{surf}, we take the surface coverage of molecules to be about 10^{15} molecules/cm^2. The laser spot size is 7.9 x 10^{-7} cm^2, so that, for molecules on the flat wetting layer, this results in N_{surf} = 7.9 x 10^8 molecules, and the wetting layer enhancement factor is then 0.9 x 10^4. If instead we consider that only molecules adsorbed on the hemi-ellipsoidal quantum dots (h = 12 nm, r = 35 nm) contribute to the enhancement, we then find that each dot has a total exposed area to the laser per dot of 3.8 x 10^{-11} cm^2. Multiplying by the dot density (1.5x10^9 dots/cm^2) the laser spot size (7.9 x 10^{-7} cm^2) and the number of molecules per unit area, we obtain N_{surf} = 4.7 x 10^7 molecules interrogated by the laser. This results in an enhancement factor due to molecules only on the dots of approximately 1.5 x 10^5. Although it is possible that the enhancement is due to molecules adsorbed on the quantum dots, for which the higher enhancement (10^5) is indicated, we cannot fully rule out the possibility that some or all of the enhancement arises from molecules adsorbed on the wetting layer instead, in which case the lower value for the enhancement factor (10^4) should be used. Note these values are about one or two orders of magnitude smaller than those obtained on Ag nanoparticles. However, they represent the largest yet observed on semiconductor quantum dot systems.

3.5 Conclusions

We have observed the enhancement of the Raman intensity of pyridine on a sample of self assembled quantum dots of $CdSe/Zn_{1-x}Be_xSe$. The enhancement factor observed is in the range 10^4-10^5 depending on which part of the surface is responsible for the enhancement. In any case, the observed enhancement is among the largest yet seen on semiconductor quantum dot systems. We therefore conclude that the enhancement is due to some combination of charge-transfer resonance and an interband transition either residing in the wetting layer or the quantum dots

Chapter 4. Surface Enhanced Raman Spectroscopy of 4-t-Butylpyridine on Silver Electrode

4.1 Introduction

The technique of surface enhanced Raman scattering (SERS) has been widely used in numerous experimental, investigations of molecular species adsorbed on metal surfaces since first measured by Fleischman et al[94] in 1974. High resolution, sensitivity, and molecular specificity, allows SERS to be the preferable technique used to investigate the nature of molecular interactions on both silver electrodes[95,96,97,98,99,100,101,102,103], as well as on semiconductor nanoparticles[104,105,106,107]. The SERS phenomenon is characterized by a large increase in the Raman intensity for molecules adsorbed on metal nanoparticles, when compared to that obtained from the same number of molecules in solution or gas phase[108,109,110,111] . This enormous increase in Raman intensities which is normally too weak to be detected when molecules are adsorbed on smooth surfaces, is effectively due to a combination of surface plasmon resonance and charge transfer resonances[112,113,114]. The surface plasmon resonance which is predicted by electromagnetic descriptions, arises from the interaction of the exciting laser frequency with the conduction band electrons. This induced electric field becomes very large when excitation takes place within surface plasmon resonances of the nanoparticle surface, producing large enhancements in Raman signals when these electric fields interact with adsorbed molecules. Additional enhancement occurs when the excitation laser frequency is in resonance with a charge-transfer transition of a specific adsorbate-metal complex. It is important to note that although the vibrational frequencies of the adsorbed molecules

are generally unaffected by SERS, their Raman intensities increases enormously. This results in dramatic changes in the intensities of the observed spectrum, especially the non-totally symmetric modes of the molecule, when the charge transfer resonances are the major contributor to the overall enhancement[115]. Typical enhancement factors obtained on a roughened Ag surface are on the order of 10^6, although extremely large Raman enhancements estimated at 10^{14} have been reported with rhodamine 6G (R6G)[116,117] on small, single Ag nanoparticles and nanowires[118].

Recently we have observed SERS from III-V (InAs/GaAs)[119] and II-VI (CdSe/ZnBeSe)[115] semiconductor quantum dots. Pyridine (C_5H_5N) was chosen as probe molecule for these SERS studies because its Raman spectrum is sensitive to the environment. Enhancement factors of approximately 10^3 and 10^5 respectively were observed. The successful use of SERS as a very useful technique for sensitive, high-resolution study of the interaction of adsorbate molecules with quantum dot surfaces has prompted us to investigate other molecules on II-VI quantum dot systems with promising results[120]. However, some of these surfaces suffer from oxidation and ripening effects due to exposure to the atmosphere. 4-tert-butyl-pyridine (4tBP) was the probe molecule chosen, since it is SERS active in the environment and it was originally believed that the bulky t-butyl addendum would tend to slow the possible ripening effect[121] of the quantum dots, and protect against oxidation. In addition, studies also have shown that the addition of 4tBP to the electrolyte in dye-sensitized solar cell[122,123,124,125,126,127], increases the open-circuit voltage and improves the long term stability of the cell. More recently using resonance Raman scattering and transient absorption spectroscopy, it was observed that

the photoinduced electron injection efficiency in nanocrystalline TiO_2 films sensitized by black dye[128,129], decreases with the addition of 4tBP.

It is therefore worthwhile to investigate the SERS of 4-t-butylpyridine on silver electrode. In this work, we report on the observation of surface enhanced Raman spectra of 4tBP are compared with its normal solution Raman spectra. We present for the first time a comprehensive assignment of the normal modes of this molecule. We also discuss the relative intensities, and shift of observed transitions.

Using laser excitation at 488 nm, chosen to be in a region of silver nanoparticle plasmon resonance, we have found a large enhancement factor, and strong enhancement of a_2 and b_2 modes of 4tBP on silver. The appearance of these non-totally symmetric a_2 and b_2 modes are typically diagnostic of a charge transfer process. This phenomenon could possibly explain the effect of 4tBP observed on photoinduced electron injection efficiency in nanocrystalline TiO_2 films sensitized by black dye[128]. Investigations to support this evidence are currently underway in this laboratory.

4.2. Experimental

Raman spectra of the sample were obtained using a Spectra Physics Model 2560 argon ion laser in conjunction with a SPEX 1401 double spectrometer. The samples were mounted near the entrance slit of the spectrometer in an electrochemical cell with electrode and configuration, as discussed in previous publications[99,130]. The normal solution Raman spectra (NR), was measured using a SPEX liquid cell. A stock solution of commercial 4-t-butylpyridine was prepared at 0.05M concentration in 0.1M KCl using deionized-distilled water. Potassium chloride (KCl) (reagent grade 99%) and 4-t-

butylpyridine (reagent grade 96%) was supplied by Sigma-Aldrich. The silver (Ag) electrode was of 99% purity.

Prior to electrochemical pretreatment the Ag electrode surface was first polished with emery paper to a bright shiny luster, then sonicated with distilled water for 15 minutes and finally rinsed with distilled water. During the electrochemical pretreatment, the electrochemical cell was filled with 0.05M 4tBP in 0.1M KCl solution. The polished Ag electrode (working electrode), was then fitted, and the potentials of the working electrode was set at -0.5V. A potential step was then applied for 2s to +0.3V and then back to the original potential at -0.5V. The electrode potential was held at -0.5V and light from a Spectra Physics Model 2560 argon ion laser was filtered to remove interference from plasma lines and focused on to the electrode in the cell with 10µm spot size. The experiment was repeated with the electrode potential held at -0.3V. All potentials were measured against a saturated calomel electrode (SCE).

The scattered Raman emission, which is reflected at 90° from the sample, was collimated using a collecting lens and focused onto the slit of the spectrometer. The slit widths were set at 150 µm, providing a resolution of about 3 cm^{-1}. Normal solution Raman spectra (NR) of 4tBP was observed replacing the electrochemical cell in the experiment a 1cm high SPEX liquid cell through which filtered light from the Spectra Physics Model 2560 argon ion laser was focused and Raman emission collected as was previously done.

All spectra reported below were taken at 488 nm. Typical power levels at the sample were measured to be approximately 30 mW.

4.3 Results

Figure 4.1 shows the NR and SERS spectra for 4-t-butylpyridine with working electrode potential held at -0.5V, excited at 488 nm in the region of 200-1700 cm^{-1}. Measured wavenumbers are listed in table 1 along with their relative intensities and Wilson assignments[131,132] of their vibrational modes and symmetry in C_{2v}. These assignments were made by analogy with the spectral assignments of methyl pyridines[100,101] as well as that of t-butly benzene[132]. Since the relative intensities of the Raman spectra arise from the surface of the Ag electrode coated with 4tBP is much greater than that of liquid, it is clear that the molecular spectral lines are considerably enhanced by proximity to the roughened silver surface. Figure 4.2 shows the SERS spectrum of the 4-tert-butylpyridine molecules adsorbed on the silver, with electrode potential at -0.3V and -0.5V. It is evident that when the same experiment was carried out with the electrode potential decreasing to -0.3V, a decrease in Raman intensities was observed, however there was no change in the vibrational frequencies of the bands.

In figure 4.1 numerous bands characteristic of 4-tertbutylpyridine appear, as seen by comparison with the normal Raman spectrum of pyridine liquid. It should be noted that in addition to the expected enhancement of several a_1 modes (678, 1022, 1212, 1236, 1482 and 1618 cm^{-1}), the bands at 732 (b_2), 1078 (b_2), 1144 (b_2) and 1284 (b_2) cm^{-1} are also considerably enhanced relative to the liquid spectrum. In addition to changes in the relative intensities, considerable Raman shift was observed in the 1022 cm^{-1} ring breathing a_1 mode. The same is true for the 732 (b_2), molecular band. A single band at 944 cm^{-1} is attributed to a mode of a_2 symmetry. When comparing the band intensities of NR with SERS of 4tBP, it should be noted that the NR was prepared in an electrolytic

solution to produce the best condition as in the SERS. This may result in suppression in the intensity of some peaks that would be more intense in pure commercial grade 4tBP. The observation of relatively intense non-totally symmetric modes is usually diagnostic of a charge-transfer contribution to the observed enhancement, most probably from the silver metal to the molecule and from the 4tBP molecule to the metal[113,114]. Intensity borrowing from the relatively intense ultraviolet $^1B_2$ transition in 4-t-butylpyridine is likely responsible for the enhancement of the b_2 vibrational bands. However, no molecular transition to a $^1A_2$ band is allowed. In a recent DFT study on pyridine attached to Ag_{10} it was found that the a_2 bands observed in the pyridine spectrum were caused by borrowing from an A_2 electronic transition in the metal cluster[1144]. This is a likely explanation of the observed intensity of the single a_2 mode.

4.4 Discussion

The observed SERS spectrum of 4tBP on Ag shows several shifts in vibrational modes from the normal Raman spectrum, and is similar to the SERS of 4-methly-pyridine or other monosubstituted pyridine[100,1132]. As previously mentioned, electromagnetic theories predict that the interaction of the exciting laser frequency of 488 nm with the Ag conduction band electrons, will produce surface plasmon resonances. This phenonomenon occurs, since excitation is taking place within surface plasmon resonances of the Ag nanoparticle surface, adding a significant contribution to the overall enhancements in Raman signals, when these nanoparticles interact with nearby 4tBP molecules. This effect has been shown to enhance only totally symmetric modes (a_1). However the abundance of non-totally symmetric modes (table 4.1) indicates the

importance of charge-transfer contributions to the overall enhancement. This is typical of Ag nanoparticle SERS, where both the charge-transfer and surface plasmon resonances have been shown to be responsible for the effect[113].

4.5 Calculation of the Enhancement Factor

It is now worthwhile to estimate the enhancement factor. As previously noted, typical enhancement factors for roughened Ag are on the order of 10^6-10^7, but under some circumstances have been reported to be as large as 10^{14}. The enhancement factor (E_F) is the ratio of Raman intensity per adsorbed molecule divided by that of the free (or solid phase) molecule, and can be determined by the following relationship:

$$EF = I_{surf}N_{sol}/I_{sol}N_{surf}$$

Where I and N are the intensities and number of molecules on the surface and in the solution. We consider total surface coverage of 4tBP molecules on the roughened silver electrode surface after electrochemical pretreatment

The 998 cm^{-1} line of the NR spectrum of 4-t-butylpyridine line was chosen for our intensity measurement. This line was chosen because it is moderately intense when compared to the other spectral lines, and well separated from its neighbors. After subtracting the background intensity, the intensity in the normal Raman spectrum of this line is approximately 241 counts, while from the surface enhanced Raman scattering on silver electrode at an electrode potential of -0.5V we obtain about 1624 counts for the 1022 cm^{-1} band. In both spectra the laser intensity and focus was kept the same. The intensity ratio (I_{surf}/I_{sol}) is therefore approximately 6.74. Using the probe spot size of the laser which is 10μm in diameter, the path length in the liquid of about 1 cm, and the

concentration of 0.05M 4tBP of 3.01 x 10^{18} molecules/cm^3 we determine that N_{sol} is 2.38 x 10^{13} molecules. In order to determine N_{surf}, we take the surface coverage of molecules to be about 10^{15} molecules/cm^2. The laser spot size is 7.9 x 10^{-7} cm^2, so that, for molecules on the roughened silver surface, this results in N_{surf} = 7.9 x 10^8 molecules, and the enhancement factor is then 0.2 x 10^6. This value is comparable to that obtained with pyridine on silver nanoparticles.

4.6 Conclusions

We have examined the surface-enhanced Raman spectrum (SERS) of 4-t-butylpyridine. A large enhancement of the Raman intensity is obtained, and we present an assignment of the Raman bands based on those observed in pyridine, methyl pyridine and t-butylbenzene. The prominence of several non-totally symmetric modes (b_2 and a_2) is taken to be evidence of charge-transfer contributions to the surface plasmon resonance usually observed in SERS. Applications to studies of 4-t-butylpyridine adsorbed on semiconductor quantum dots and dye sensitized TiO_2 based solar cells are discussed.

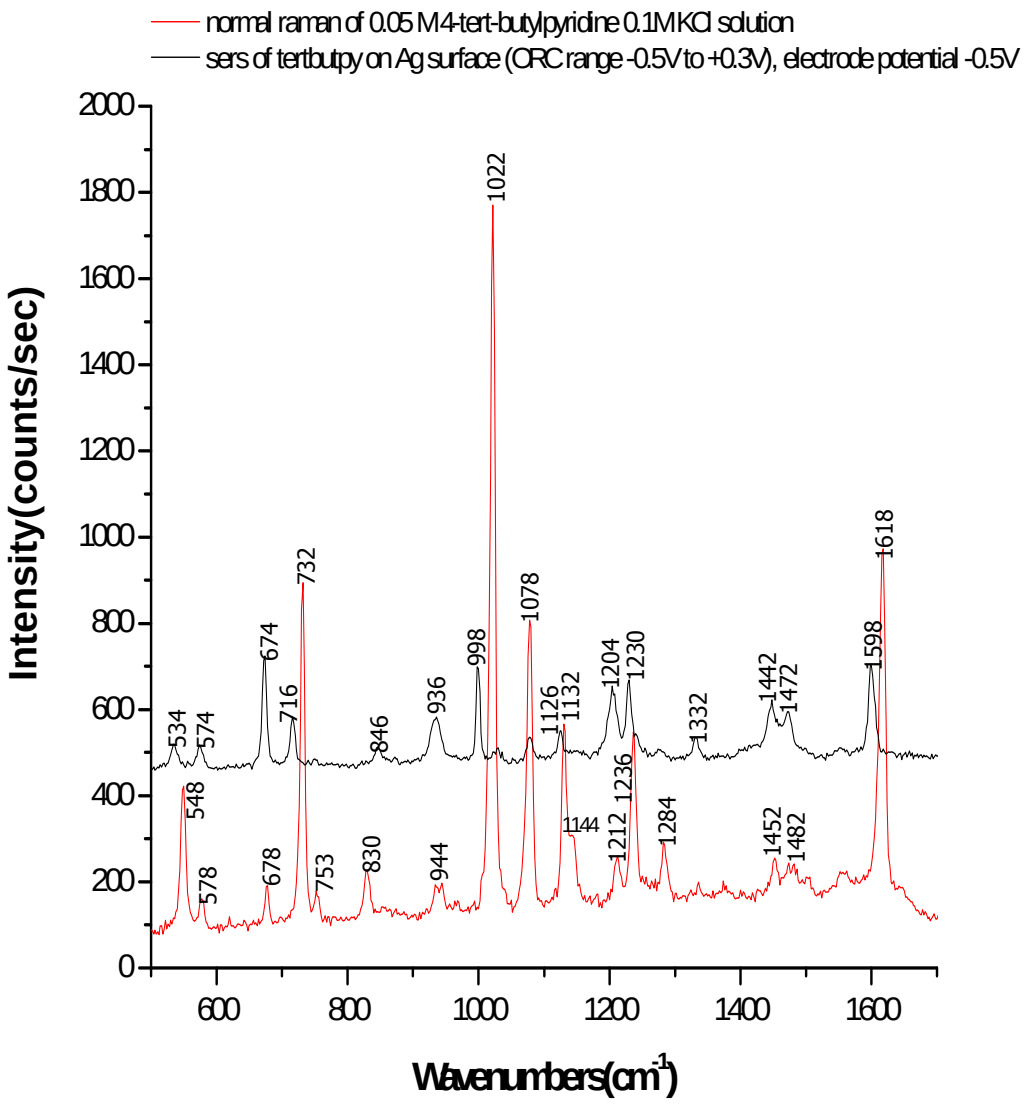

Figure 4.1. Normal Raman and SERS spectrum of 4-t-butylpyridine on Ag at -0.5 volts.

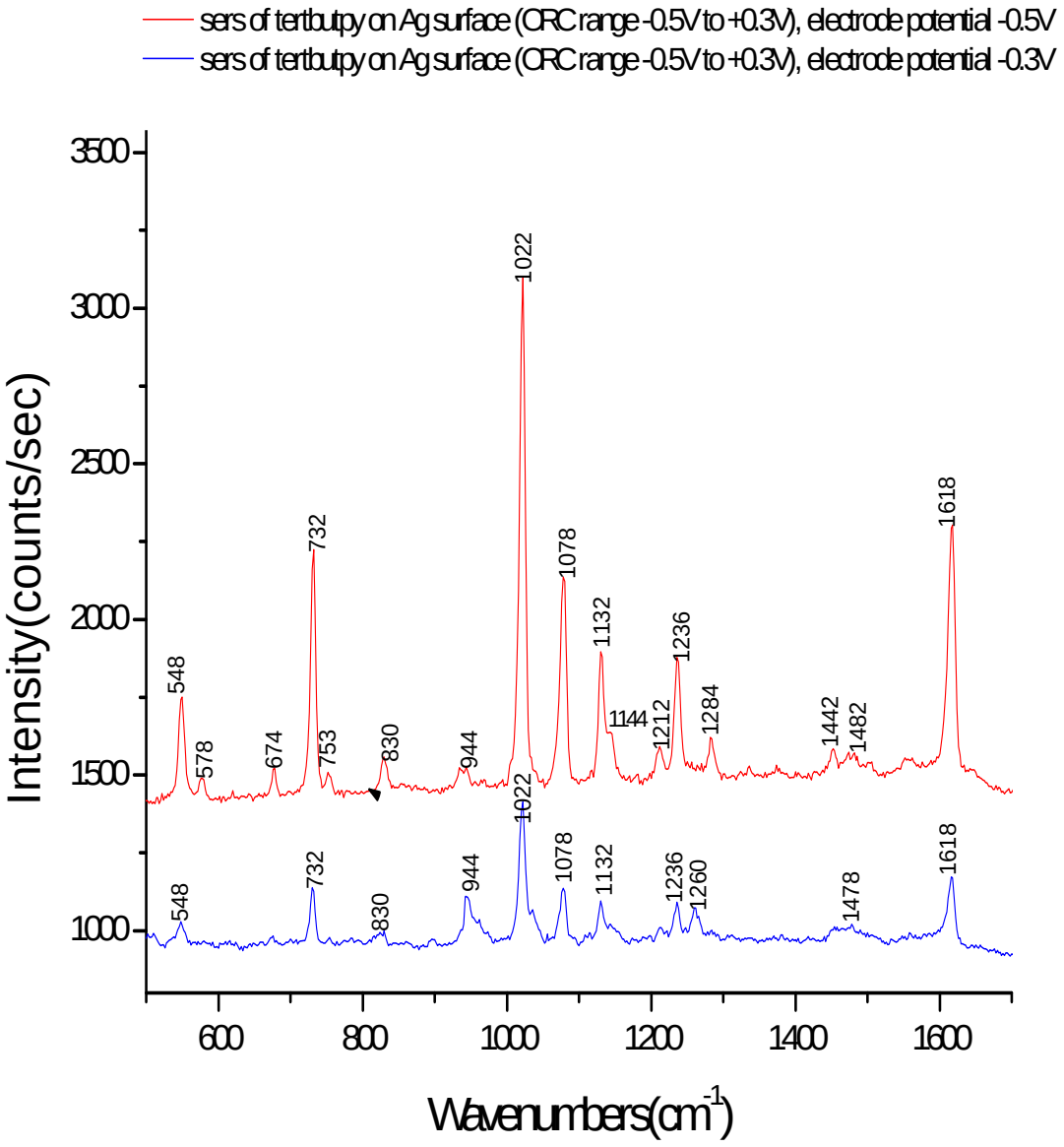

Figure 4.2. SERS spectrum of 4-t-butylpyridine on Ag at -0.3 and -0.5 volts.

Wilson no	**C_{2v} Sym**	**Herzberg no**	**4-Me pyr liquid**	**t-but benz liquid**	**t butpy liquid (NR)**	**t butpy Ag (SERS)**
		ν_{10}	530	530	534 (w)	548(s)
					574(w)	578(m)
6a	a_1	ν_{19}	673	625	674(s)	678(m)
6b	b_2	ν_{25} (oop)	725	710	716(m)	732(vs)
4	b_1					753(w)
		$\nu_{24,}\nu_9$	812	845	846(vw)	830(m)
17a	a_2	ν_8 (oop)		930	936(m)	944(w)
1	a_1	ν_8	1011	1002	998(s)	1022(vs)
18a	a_1			1030		
18b	b_2	$\nu_{7,}M_6$	1074		1078 (w)	1078(vs)
				1115	1126 (w)	1132(s)
15	b_2	$M_6(b_2)$		1160		1144(sh)
				1190		
9a	a_1			1205	1204(m)	1212(w)
9a	a_1	m_1, ν_6	1222, 1231		1230(m)	1236(s)
3	b_2	M_3		1270		1284(m)
3	b_2	M_3	1387		1332(w)	1374(vw)
19b	b_2	M_4	1424	1445	1442(m)	1452(vw)
19a	a_1	ν_5		1475	1472(m)	14782(vw)
8a	a_1	ν_4	1617	1600	1598(s)	1618(vs)

Table 4.1: Assignment of t butylpyridine peaks as observed in Normal Raman, SERS on a Ag surface when compared with 4-Methylpyridine and t-butylbenzene liquid. The notation M_n referrs to normal modes centered on the t-butyl part of the molecule. Lombardi, J.R.; Birke, R.L Foucault R; Vivoni A, *J.Phys.Chem. B*, 2003, 107, 5547-5557. and Dollish, F.R.; Fateley, W.G.; Bentley, R.F.; *Characteristic Raman Frequencies of Organic Compounds. John Wiley & Sons, Inc,* ***1974, pp 170-175***

Chapter 5: SERS of 4-t-Butylpyridine, Adenine, Tryptophan and Tyrosine on MBE Grown ZnCdMgSe /CdSe Quantum Dots

5.1 Introduction

The recent development in the application of semiconductor quantum dots to novel electronic as well as photonic devices, such as single-electron transistors, LEDs and biosensors emphasizes the need to develop techniques for characterizing the surface of the quantum dots. Raman spectroscopy has proven invaluable for detection and identifying important molecules and has been successfully applied to these quantum dot systems (chapter 3).

In this chapter, the observation of surface enhancement of a Raman signal from 4-t-butylpyridine molecules adsorbed on a self-assembled CdSe/ ZnCdMgSe, uncapped quantum dots grown by molecular beam epitaxy (MBE) is reported. 4-T-butyl pyridine was chosen to take advantage of the bulky t-butyl group to suppress possible oxidation of the quantum dots during observation. Other spectral properties, however, are similar to those of pyridine, which is use for comparison. Because it was proven (in chapter 3), that the higher degree of surface enhancement observed on the II-VI (CdSe/ZnBeSe)[133] system, was due to the fact that the excitation wavelength is in the vicinity of several interband transitions located both in the quantum dots and the wetting layer, the effect of varying the quaternary bandgap on Raman signal, by changing the deposition temperature of magnesium will be examine. Laser excitation at 488 nm, chosen to be in a region of QD absorption was used, yielding a large enhancement factor. However changes in the quaternary bandgap were found to show a dramatic effect on the Raman signal as well.

5.2. Experimental

5.2.1 Molecular Beam Epitaxial Growth of Samples

The quantum dot (QDs) samples were grown by Molecular Beam Epitaxy (MBE) on InP (001) substrates in an ultrahigh vacuum (UHV) Riber system that has two Riber 2300 growth chambers, one dedicated to III-V materials and another for II-VI materials. First, the oxide layer of the InP substrate is removed by heating the substrate with an As flux impingent on the substrate surface. The oxide desorption of the substrate was monitored using reflection high-energy electron diffraction (RHEED). The removal of the oxide layer was established by the transition from a (2 x 4) to a (4 x 4) surface reconstruction at about 495 ºC. Immediately after the deoxidation temperature was reached, the substrate temperature was decreased to 470 ºC to recover the (2 x 4) surface reconstruction and then, a 150 nm lattice-matched InGaAs buffer layer was grown in order to obtain an atomically flat surface for the growth of the II-VI layers. The substrate temperature was gradually increased to about 485 ºC during the InGaAs layer growth. The RHEED showed a streaky (2 x 4) surface reconstruction during growth, indicating a good quality of the epilayer and the formation of an As-terminated surface, which is essential to obtain a good II-VI/III-V interface. After the III-V buffer layer growth, the samples were transferred into the II-VI chamber in UHV. Prior to the growth of II-VI layers, a Zn exposure for 40 sec at 170 ºC was performed to reduce defect density of the ZnCdMgSe epilayer, which is related to the formation of undesired compounds between Se atoms and In/Ga atoms, such as Ga_2Se_3[134]. This Zn exposure was followed by ~60 Å ZnCdSe to promote the two dimensional nucleation and to allow an ordered deposition of the ZnCdMgSe layer. Then the substrate temperature was increased to 255 ºC and a 13 nm

ZnCdMgSe buffer layer was grown. After this, the substrate temperature was set at 270 ºC for the remainder of the structure growth. The total thickness of the quaternary barrier is 400 nm, the RHEED showed a streaky Se-terminated (2 x 1) surface reconstruction indicating a good quality epilayer formation[135]. To initiate the CdSe deposition, the Zn and Mg shutters were closed. The CdSe QDs were formed on the ZnCdMgSe barrier by 10 sec-CdSe deposition time followed by a growth interruption time of 30 s with only the Se shutter open. The nominal thickness correspond to this deposition time is 2.5 monolayers (ML). Growth finished decreasing the temperature to 225 ºC under Se flux rich conditions. Samples were removed from the chamber immediately following the QD formation. Two other samples were grown under identical conditions except during the deposition of the ZnCdMgSe layer, the substrate temperature was increased to 255 ºC and 275 ºC for each respective sample. In order to slow the ripening effect[134], the samples were immediately immersed in liquid nitrogen after the growth and kept in this condition until the moment of taking the surface topography or Raman spectra.

5.2.2 Atomic Force Microscopy

Atomic Force Microscope (AFM) images were recorded in contact mode using a ThermoMicroscopes Explorer™ system (Veeco Instruments, Santa Barbara, CA, USA), operated in air and at room temperature. Silicon microfabricated cantilevers (Veeco nano-probe tips Model # 1650-00) possessing a spring constant of 13-100 N/m and a resonance frequency of 260 kHz were used. The integral and proportional gains ranged between 0.5 and 1.2. Images were recorded in the range of 5x5 μm with a 300 x 300 pixel resolution and a scan rate of 3.69 μm/s. The microscope was placed on a pneumatic anti-vibration

table, under a damping cover. The processing was conducted using the SPMLab software.

5.2.3 Raman Spectroscopy

A stock solution of commercial 4-t-butylpyridine was prepared at 1mM concentration in deionized-distilled water. One of the cut pieces of the quantum dot samples were then removed, allowed to attain room temperature conditions, and then immersed in a small portion (10ml) of the liquid 4-tertbutylpyridine for 20 minutes. The sample was sonicated in commercial acetonitrile solution for 5 minutes to remove excess liquid and mounted near the entrance slit of a SPEX (0.75 meter) model 1401 double monochromator. Light from a Spectra Physics Model 2560 argon ion laser was filtered to remove interference from plasma lines and focused on to the sample with 5µm spot size. The scattered Raman emission, which is reflected at 90° from the sample, was collimated using a collecting lens and focused onto the slit of the spectrometer. The slit widths were set at 150µm, providing a resolution of about 3 cm^{-1}. All spectra reported below were taken at 488 nm. Typical power levels at the sample were measured to be approximately 30 mW.

5.3. Results

The atomic force micrograph (AFM) images in figure 5.1a and 51b show the three-dimensional images of two uncapped samples with different MgSe content in the barrier. The variation in MgSe content was carried out in order to examine the effect of the size

and density of the QDs on the Raman signal. Both samples were grown with the same CdSe deposition time 10 sec, which correspond to a nominal thickness of 2ML. The MgSe concentration of the sample in fig 5.1a, is 39% by weight of the total ZnCdMgSe barrier and was deposited at 255 ºC. These fabricating conditions give rise to a quaternary ZnCdMgSe structure with a band gap of 2.6 eV (480 nm), while the MgSe content of the sample in figure 5.1b is 59% and was deposited at 275 ºC, with a quaternary bandgap of 2.9 eV. The higher concentration of Mg results in a more uniform size distribution of QDs in the sample. This result can be explained by a thermodynamic influence of Mg in the CdSe QDs formation. A higher Mg concentration changes the surface energy of the ZnCdMgSe which influences the wetting characteristics (binding energy between the substrate and the material deposited on the top) and, consequently, the size of the QDs.

The AFM images of both figure 5.1a and 5.1b recorded in the area of 5x5 μm indicates that the QDs have a hemi-ellipsoidal shape with a height of 4.5 ± 0.5 nm being the most abundant value in fig 5.1a. The average radius of the QDs base is 47 nm and average QDs density was $7x10^8$ cm^{-2}. However, in figure 5.1b, the most abundant QD height was 1.6 ± 0.5 nm, the lateral size was reduced at 30 nm and the average density of QDs was increased to 1.02 $x10^9$ cm^{-2}. It was observed that not only height, radius and density were affected by an increase of MgSe content in ZnCdMgSe barrier but also resulted in more uniform size distribution in the sample.

Contactless electroreflectance (CER) studies[136] on similar samples, in which the quantum dots are capped by another ZnCdMgSe layer, grown under same condition as the quaternary barrier, provide evidence for a thin wetting layer. Calculation of the volume of the quantum dots indicates that the wetting layer is approximately 1.0-1.5 ML

and this is consistent with the CER studies. The remainder forms the hemi-ellipsoid quantum dots.

Figure 5.2 shows the SERS spectrum of the 4-t-butylpyridine molecules adsorbed on the CdSe quantum dots grown on quaternary bandgap of 2.6 eV, together with the Raman spectrum of the quantum dots sample before the deposition of the molecule and the Raman spectrum of the 4-t-butylpyridine solution. Laser excitation was at 488nm and in the region of 450-1400 cm^{-1} We observed numerous lines characteristic of 4-t-butylpyridine, as can be seen by comparison with the normal Raman spectrum of 4-t-butylpyridine liquid and listed in table 5.1. These are listed in the table, along with the lines observed on Ag, as well as a summary of the assignment of the normal modes[137] of 4-t-butylpyridine, including their Wilson number and symmetry in C_{2v}. The molecular spectral lines are considerably enhanced by proximity to the quantum dots, since when the same experiment was done one on a thick ZnCdMgSe layer with no quantum dots, no Raman signals from the molecule was observed.

In figure 5.3, we show the SERS spectrum of the 4-t-butylpyridine molecules adsorbed on the CdSe quantum dots, grown on the quaternary layer with different bandgaps. The bandgaps of the quaternary layer used were; 2.6 eV (480 nm), 2.9 eV (430 nm) and 3.0 eV (400nm). It is worthwhile to note that as the bandgap of the quaternary layer shifts to the blue, the Raman intensities of the molecule decrease dramatically.

The enhanced spectral lines observed on the quantum dot surface in figure 5.2 correlates well to most of the lines previously observed either in the liquid or on a Ag surface. However, in addition to the enhancement of a_1 modes (678, 1034 cm^{-1}), several b_2 bands (738, 1073, 1268, 1377 cm^{-1}), (b_1), 738 and (a_2) 960 cm^{-1} are also considerably

enhanced relative to the liquid spectrum. The observation of relatively intense non-totally symmetric modes is usually diagnostic of a charge-transfer contribution to the observed enhancement, which is probably from the CdSe QDs to the molecule and from the 4tBP molecule to the metal[138,139]. Intensity borrowing from the relatively intense ultraviolet $^1B_2$ and $^1B_1$ optical transition in 4-t-butylpyridine are likely responsible for the enhancement of the b_2 and b_1 vibrational bands. However, no molecular transition to a $^1A_2$ band is allowed in t-butyl-pyridine. In a recent DFT study on pyridine attached to Ag_{10} it was found that the a_2 bands observed in the pyridine spectrum were caused by borrowing from an A_2 electronic transition in the metal cluster[138]. This is a possible explanation of the observed intensity of the single a_2 mode in this system.

5.4. Discussion

The observed SERS spectrum of 4-t-butylpyridine on CdSe quantum dots grown on a ZnCdMgSe barrier (2.6 eV), shows several shifts in vibrational modes from the normal Raman spectrum, and is similar to the to the SERS observed on Ag nanoparticles. The abundance of non-totally symmetric lines (table 5.1) indicates the importance of charge-transfer contributions to the overall enhancement. As previously mentioned in chapter 3, electromagnetic theories predict that the interaction of the exciting laser frequency with the conduction band electrons in metals, will produce surface plasmon resonances. This is typical in Ag nanoparticles and not in semiconductors, where the excitation wavelengths are far from the region of surface plasmon resonance as seen in CdSe and so the magnitude of enhancement must be attributed to other possible resonances. It is highly suggestive that one contribution is likely a charge transfer

resonance between the molecule and the quantum dot as previously described in chapter 3, where it was shown that in a recent study of molecules on ZnO quantum dots[140] demonstrated that a size dependent resonance could be observed, and that a surface-bound ionized acceptor-exciton complex[141] was implicated in the mechanism. This mechanism has since been proven[142], and was suggested in our recent work[Error! Bookmark not defined.Error! Bookmark not defined.] with pyridine using a Be doped barrier. Additionally, the CER spectrum[143] at room temperature for the CdSe/ZnSe QD (grown with similar bandgap 2.56 eV to the sample in table 5.1 and figure 5.1a) structure shows, several interband or excitonic transitions in the quantum dot in the optical region, which may be assigned to peaks observed near the laser excitation at 2.54 eV. These interband transitions are at 2.32 eV (QD_0) and 2.46 eV (QD_1), corresponding to the CdSe/ZnSe QDs wetting layer bandgap of 2.56. This bandgap energy is similar to quaternary ZnCdMgSe used in this study which is 2.6 eV. The band gap energy for the bulk CdSe is approximately 1.6 eV. As previously indicated in chapter 3, since the laser excitation energy is closest to the wetting layer transition, there is a great possibility that one or more of the quantum dot transtitions are excited by the laser. This is evident in figure 5.3 where the Raman intensities of the samples decreases dramatically, as the bandgap energies 2.9 eV (430 nm) and 3.0 eV (400 nm) move further away from the laser excitation frequency of 2.54 eV (488nm).

5.5 Calculation of the Enhancement Factor

The enhancement factor was calculated based on the equation used in chapter 3.4.1 and similar treatment of the quantum dot. It should be noted however that the dots have a height of 4.5 nm and a radius of 47 nm.

The intensity measurements was taken at the 1078 cm^{-1} line of 4-t-butylpyridine on the quantum dots which were fabricated on 2.6 eV quaternary ZnCdMgSe. This line was chosen because it is moderately intense when compared to the other spectral lines, and well separated from its neighbors. After subtraction of the background intensity, the intensity in the normal Raman spectrum of this line is about 61 counts, while from the surface enhanced quantum dot spectrum, we obtain about 266 counts. In both spectra the laser intensity and focus was kept the same. The intensity ratio (I_{surf}/I_{sol}) is therefore approximately 4.36. Using the probe spot size of the laser which is 10μm in diameter, the path length in the liquid of about 1 cm, and the concentration of 0.01M 4-t-butylpyridine of 6.0 x 10^{18} molecules/cm^3 we determine that N_{sol} is 4.7 x 10^{12} molecules. In order to determine N_{surf}, we take the surface coverage of molecules to be about 10^{15} molecules/cm^2. The laser spot size is 7.9 x 10^{-7} cm^2, so that, for molecules on the flat wetting layer, this results in N_{surf} = 7.9 x 10^8 molecules, and the wetting layer enhancement factor is then 0.3 x 10^5. If instead we consider that only molecules adsorbed on the hemi-ellipsoidal quantum dots (h = 4.5 nm, r = 47 nm) contribute to the enhancement, we then find that each dot has a total exposed area to the laser per dot of 6.94 x 10^{-11} cm^2. Multiplying by the dot density (7 x 10^8 dots/cm^2) the laser spot size (7.9 x 10^{-7} cm^2) and the number of molecules per unit area, we obtain N_{surf} = 4 x 10^7

molecules interrogated by the laser. This results in an enhancement factor due to molecules only on the dots of approximately 0.5 x 10^6. Although it is possible that the enhancement is due to molecules adsorbed on the quantum dots, for which the higher enhancement (10^6) is indicated, we cannot fully rule out the possibility that some or all of the enhancement arises from molecules adsorbed on the wetting layer instead, in which case the lower value for the enhancement factor (10^5) should be used. These values are similar to those obtained on Ag nanoparticles and are one or two orders of magnitude larger than previously reported[Error! Bookmark not defined.Error! Bookmark not defined.] on semiconductor quantum dot systems.

5.6 Conclusions

In this work we have obtained highly enhanced Raman spectra for 4-t-butyl pyridine adsorbed on MBE-grown quantum dots of CdSe on a ZnCdMgSe barrier. The measured enhancements are among the highest yet observed for semiconductor systems, and are close to those observed on metals surfaces. The bandgap dependence indicates that transitions to the bandgap are important contributors to this enhancement, and may possibly be regarded as a replacement for the surface plasmon resonance so important in metallic SERS. As in SERS, however, the observation of non-totally symmetric bands indicates additional contributions from charge-transfer resonances. It is most likely a combination of these two effects which is responsible for the rather large enhancements observed here.

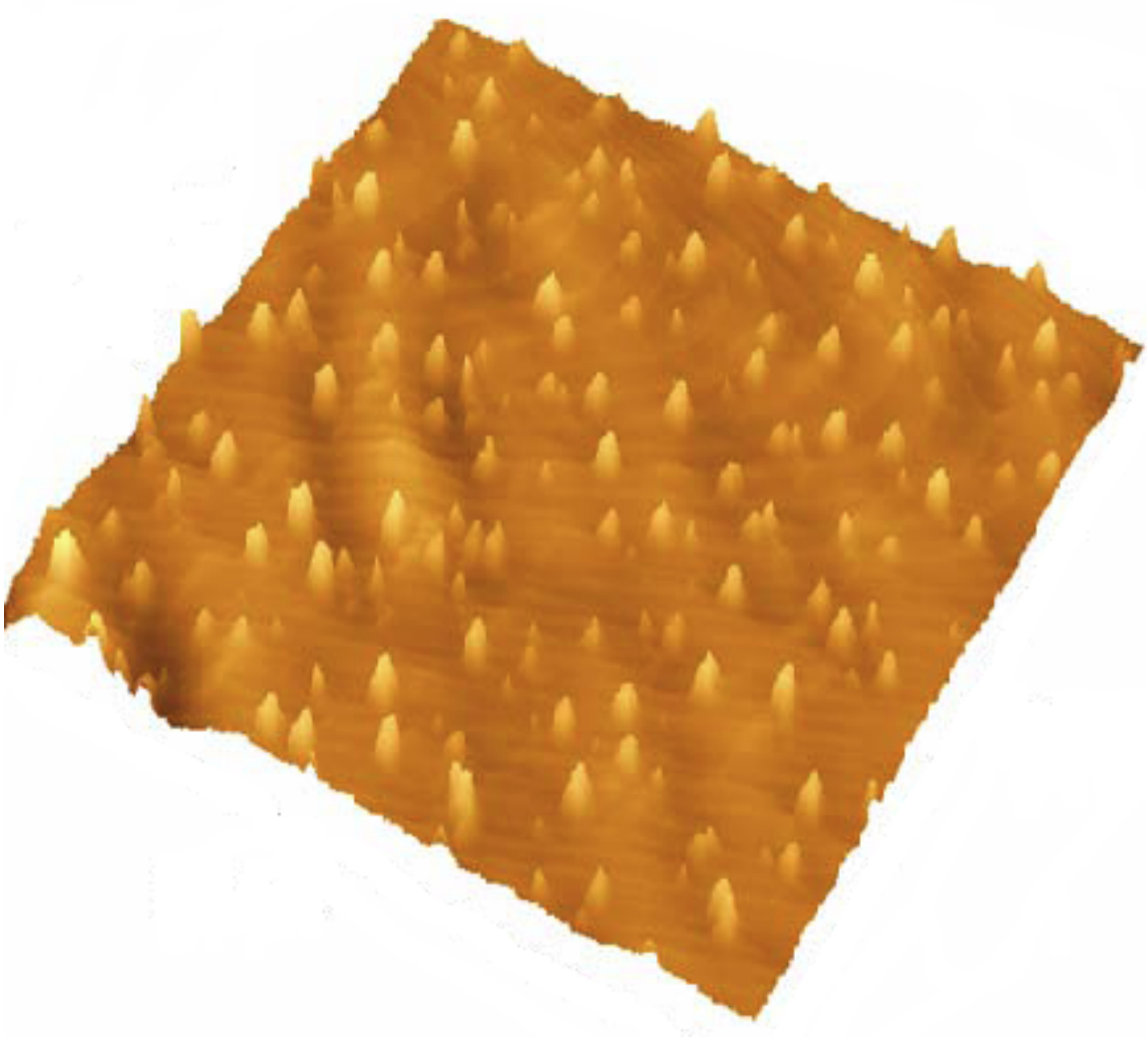

Figure 5.1a. Three dimensional AFM image for uncapped QD with 2ML-CdSe nominal thickness and 39% MgSe content in the ZnCdMgSe barrier

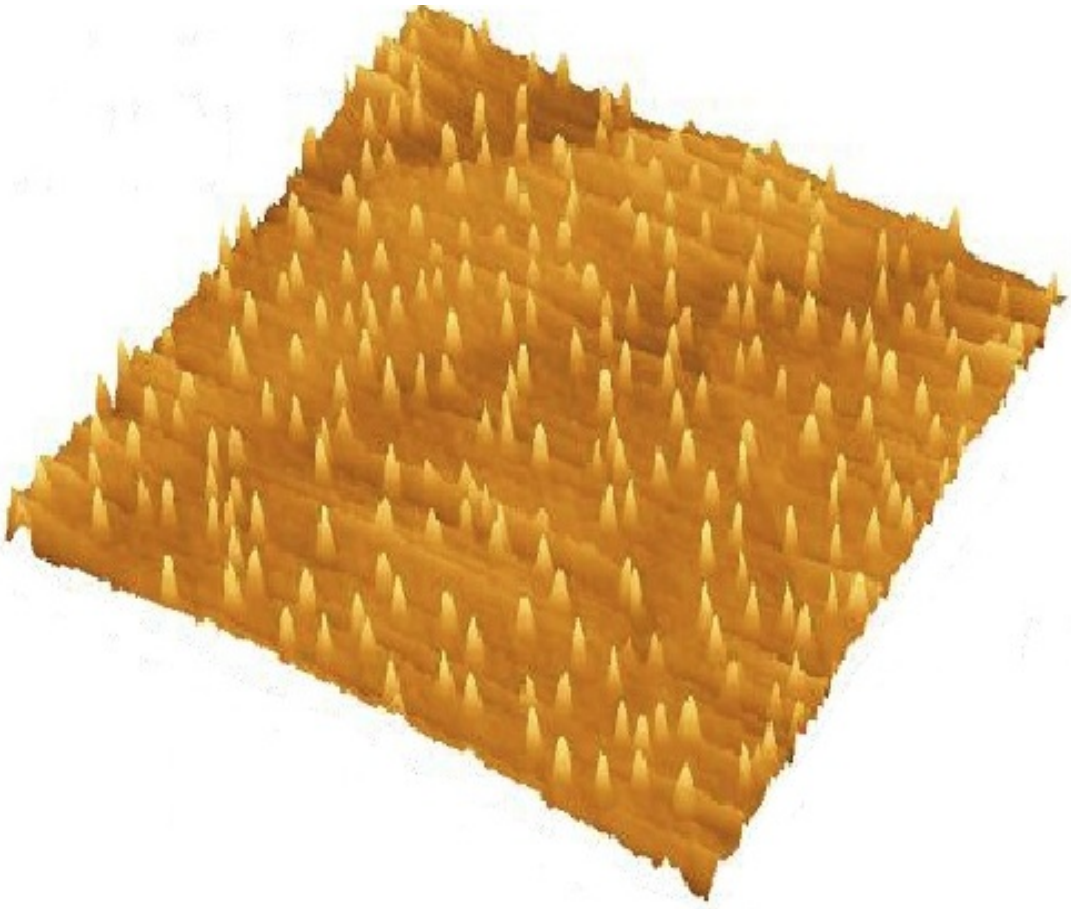

Figure 5.1b. Three dimensional AFM image for uncapped QD with 2ML-CdSe nominal thickness and 59% MgSe content in the ZnCdMgSe barrier

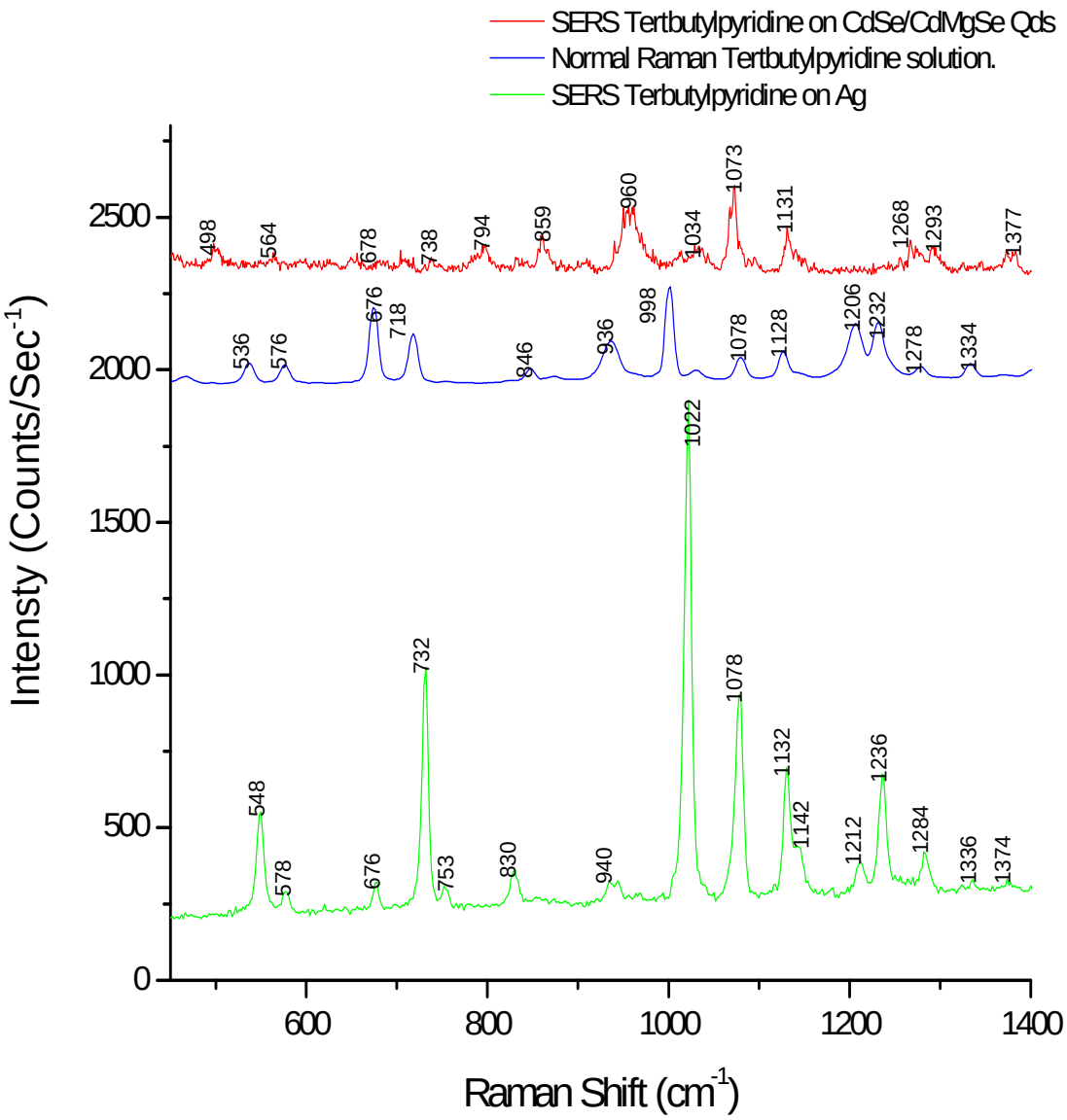

Figure 5.2. Normal Raman and SERS spectrum of 4-tbutylpyridine on Ag and CdSe quantum dots (quaternary bandgap ~2.6 eV) excited at 488 nm

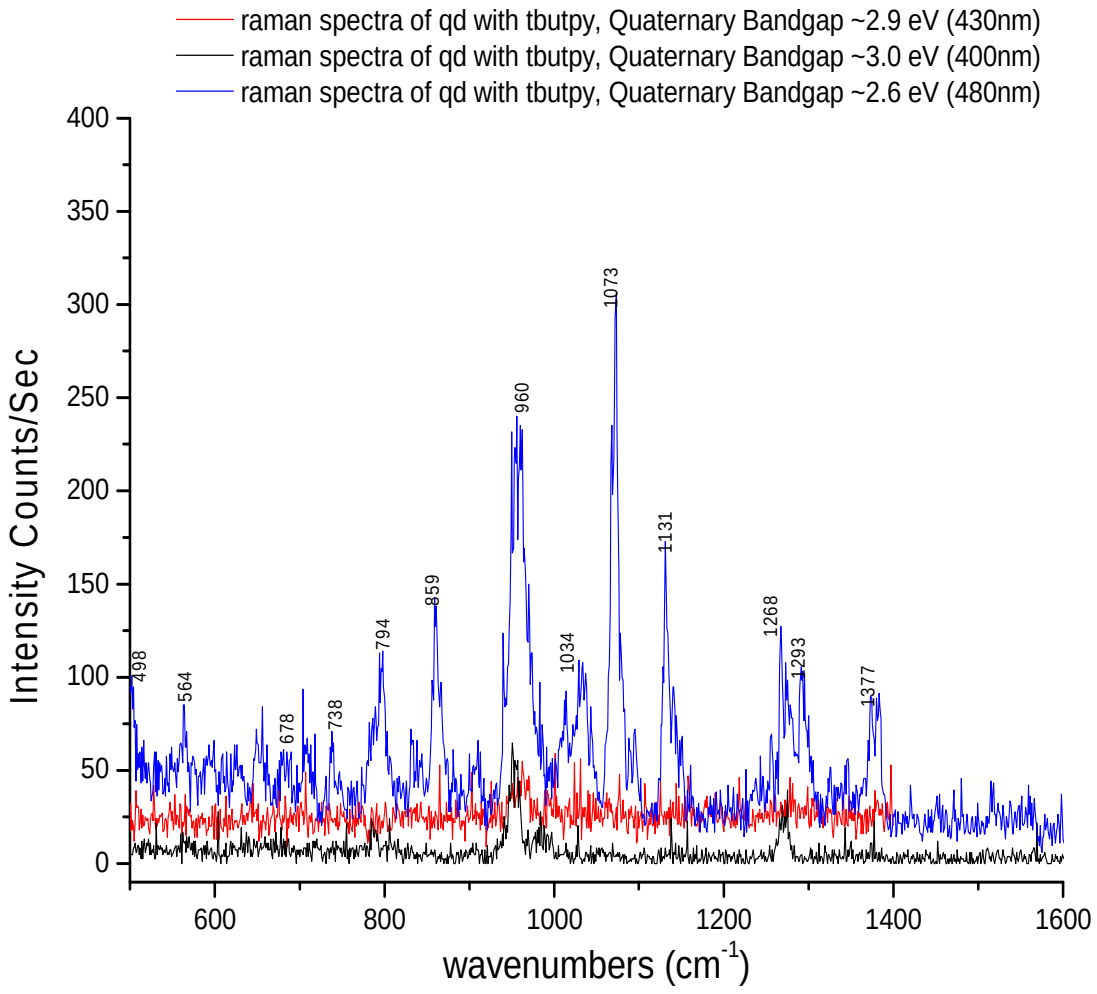

Fig 5.3 SERS spectrum of 4-t-butylpyridine on CdSe quantum dots, grown with different quaternary bandgap and excited at 488 nm

Wilson no	C_{2v} Symm	Hberg Assmt	t butpy Liquid (NR)	t butpy Ag (SERS)	t butpy CdSe/ ZnMgSe
		ν_{10}	536 (w)	548(s)	
			576(w)	578(m)	564(w)
6a	a_1	ν_{19}	676(s)	678(m)	678(vw)
6b	b_2	ν_{25} oop	718(m)	732(vs)	738(vw)
4	b_1			753(w)	794(w)
		$\nu_{24,}\nu_9$	846(vw)	830(m)	859(mw)
	a_2	ν_8 (oop)	936(m)	940(w)	960(s)
1	a_1	ν_8	1002(s)	1022(vs)	
12	a_1		1034 (vw)		1034(vw)
18b	b_2	$\nu_{7,}M_6$	1080 (w)	1078(vs)	1073(s)
9b	b_2		1128 (w)	1132(s)	1131(m)
15	b_2	$M_6(b_2)$		1142(sh)	
9a	a_1		1206(m)	1212(w)	
9a	a_1	m_1, ν_6	1232(m)	1236(s)	
3	b_2	M_3	1278(w)	1284(m)	1268(m)
3	b_2	M_3	1334(w)	1374(vw)	1377(m)
19b	b_2	M_4	1450(m)	1452(vw)	
19a	a_1	ν_5	1472(m)	1472(vw)	
			1554(vw)	1554(vw)	
8a	a_1	ν_4	1602(s)	1618(vs)	

Table 5.1: Assignment of tert butylpyridine lines as observed in Normal Raman, SERS on a Ag surface and on ZnCdMgSe /CdSe self-assembled quantum dots. Quaternary bandgap ~ 2.6 eV

5.7 SERS of Adenine Tyrosine and Tryptophan on ZnCdMgSe /CdSe self-assembled quantum dots

5.7.1 Introduction

Recent developments in SERS and applications of semiconductor quantum dots as indicated in the previous chapters led to the investigation of several molecules of biological interest, namely adenine (figure 5.4), tryptophan (figure 5.5) and tyrosine (figure 5.6) in order to ascertain whether the method might be of use in the growing field of biosensors. Using laser excitation at 488 nm, a much larger enhancement factor can be obtained in II-VI semiconductors than in III-V systems was observed, and by detailed analysis of the observed Raman spectra, determination of how the molecule is attached to the surface, can be ascertained, at least in some cases. Furthermore, the high degree of spectral selectivity, coupled with the high sensitivity afforded by the rather large enhancement factors, makes such systems good candidates for possible use in detecting and identifying biological molecules.

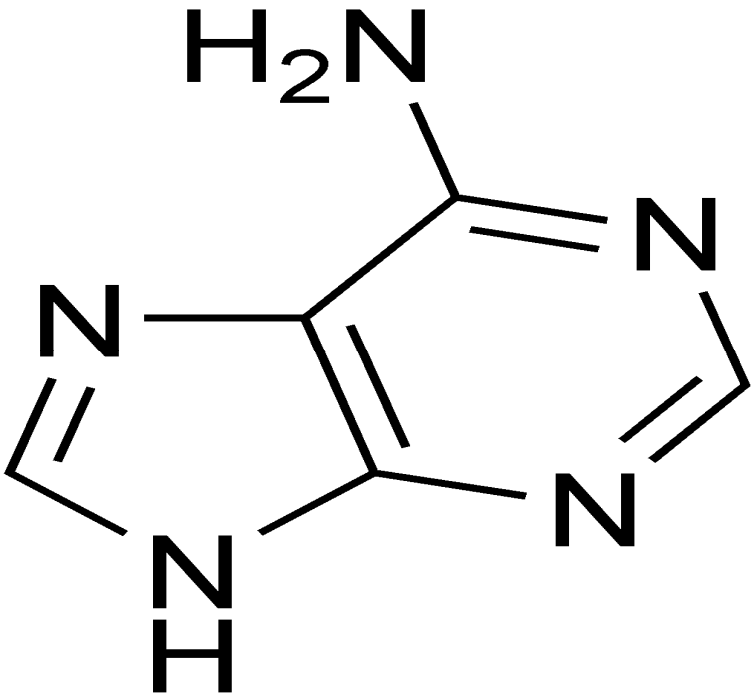

Figure 5.4 showing the molecular structure of Adenine

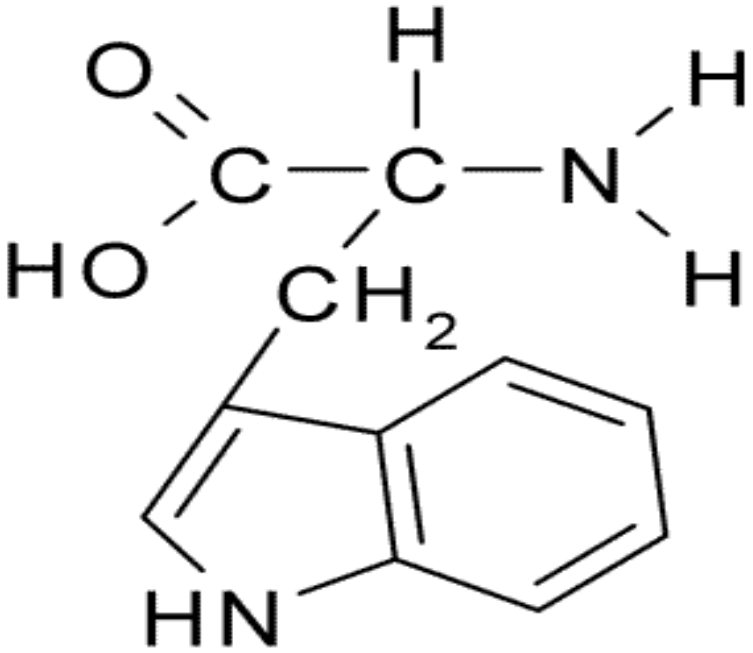

Figure 5.5 showing the molecular structure of Tryptophan

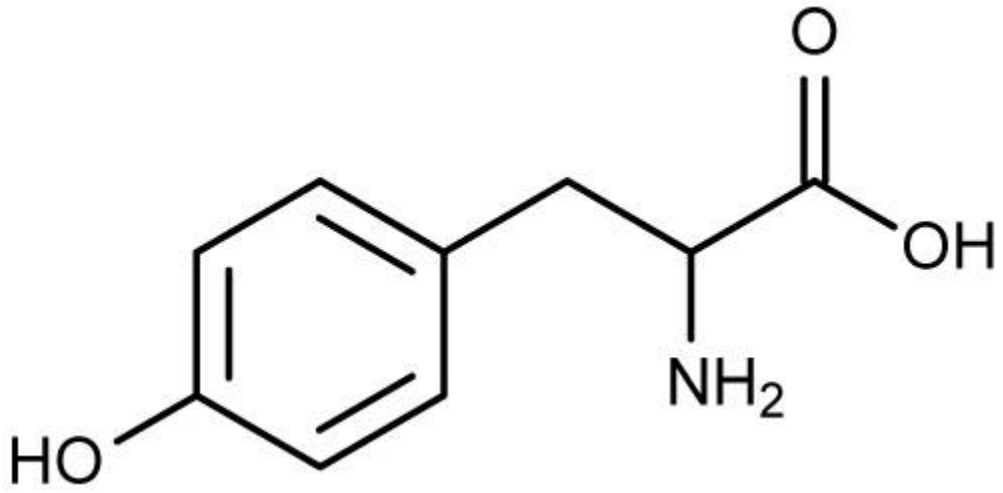

Figure 5.6 showing the molecular structure of Tyrosine

5.7.2 Experimental

The ZnCdMgSe /CdSe self-assembled quantum dots used in this experiment were grown under similar MBE condition to the sample in section 5.2.1. This results in a sample with quaternary bandgap energy of approximately 2.6 eV. Both AFM and Raman measurements were also taken under similar conditions as outlined in sections 5.2.2 and 5.2.3. Prior to taking the Raman measurements, a stock solution of 10^{-2} M solution of adenine, tryptophan and tyrosine was prepared using de-ionize water. The samples were then removed from liquid nitrogen, allowed to attain room temperature then placed in 10 mls portion of solution for 15 minutes. The sample was then sonicated for 5 minutes in acetonitrile to remove the excess layer, and then mounted near the entrance slit of a SPEX (1 meter) model 1401 double monochromator. The experiment was then carried out as outline in previous sections.

5.7.3 Results

Figure 5.7 shows a representative AFM image of the quantum dot sample. This demonstrates individual dots with the geometrical parameters typical for QDs: average height 8 nm, interparticle distance ~0.61 μm and surface density ≈ 2.04×10^8 dots/cm^2. The lateral diameter is determined only approximately to be 0.11(10) μm. The reason for the large degree of inaccuracy is the fact that sample features are roughly the same size as the probe tip used for imaging. This distorts the geometry of the probe tip during the imaging process and thus renders measured lateral size inaccurate. However, if we consider the total amount of CdSe deposited (2.5 ML), and use the accurate values for the dot density and height, we may calculate the dot diameter assuming a cylindrical shape (as seen in section 5.3). This result is 0.2 μm, in reasonable agreement with the AFM measurement. The ratio of height to diameter indicated here deviates considerably from either a sphere or hemisphere, which might be the expected shape for a dot. It might be more appropriate to call these quantum islands.

Figure 5.8 shows the Raman spectrum of the sample before coating with a molecule. It is important to note that several broad but weak features, which are most likely overtones of the phonon modes of the quantum dots, which are not observed when the substrate was examined, without the CdSe dots deposited (figure 5.9). When molecules are deposited on these samples, in addition to the Raman lines discussed below, we observe the appearance of several sharp and intense photo-emission bands. Some of these appear to coincide closely with the weak broad bands from the bare quantum dots (about 650, 950, and 1260 cm^{-1}). That these are due to emission, rather than

Raman shifts is confirmed by observation of spectra excited at 514.5 nm, in which these lines appear at the same absolute frequency. However, any Raman intensity, which may appear excited at this wavelength is too weak to measure. Neither Raman lines nor luminescence were observed using the Krypton ion laser line at 647 nm.

Figures 5.10-5.12 shows the Raman spectra of CdSe quantum dots coated with adenine, tryptophan, and tyrosine. Included in each of the plots is the spectrum of the uncoated dots (figure 5.8) on the same intensity scale as the coated spectra. It is clear that the molecular spectral lines are considerably enhanced by proximity to the quantum dots. When the same experiment was carried out on the substrate without quantum dots deposited, no spectra of these molecules could be observed. The lower frequency regions of these spectra are dominated by intense semi-conductor phonon modes, obscuring any possible molecular lines, and are not shown here since further analysis will be needed especially to develop a technique for lowering the intensity of the phonon modes so that any enhanced molecular lines can be observed.

The adenine spectrum in the region 500-1500 cm^{-1}, is shown in figure 5.10, with measured frequencies listed in table 5.2. Numerous lines characteristic of adenine appear, as can be seen by comparison to the normal Raman (NR) spectrum of the solid and the surface enhanced Raman spectrum (SERS) of adenine on Ag taken at 632 nm. We have also included a brief description of the normal modes assigned[144]. With the exception of a line at 862 cm^{-1}, and the abovementioned emission peaks, all the lines correspond to lines previously observed either in the solid or on a Ag surface. Note the absence of the ring breathing mode ν_{21} at 731 cm^{-1}, as well as lack of most of the bands attributed to $-NH_2$ motions. Only the ν_{12} $-NH_2$ rocking mode appears in this spectrum at 1235 cm^{-1}.

However, prominent in the spectra are numerous other lines (ν_{27}, ν_{20}, ν_{19} and ν_{16}) at 539, 789, 839, and 973 cm^{-1}. These have in common the fact that they represent out-of-plane vibrations. In surface enhanced Raman spectroscopy, this, along with the absence of the ring-breathing mode, is usually indicative of a molecule in which the plane lies parallel to the surface, and this is our interpretation. It is possible that in this configuration, the $-NH_2$ lies sufficiently close to surface atoms to have the modes associated with this part of the molecule either strongly shifted or decreased in intensity.

The tryptophan spectrum in the region 500-1500 cm^{-1}, is shown in figure 5.8, with measured frequencies listed in table 5.3. Also listed in table 5.3 are the lines obtained for the resonance Raman spectrum of liquid tryptophan taken at 200nm[145], as well as the IR spectrum of the liquid zwitterion[146]. Once again it can be seen that almost all of the lines observed in the CdSe quantum dot spectrum correspond to either Raman or IR lines observed. In some cases possible Raman lines coincide with emission lines, resulting in some ambiguity. Since both ring breathing modes at 766 and 1011 cm^{-1} appear on the quantum dot samples, it is likely that the molecule is oriented edge-on. Furthermore, since several prominent bands associated with either the β-NH_3^+ or the β-CO_2^- (in the zwitterionic form) are also observed relatively unshifted, it is unlikely that these species are the mode of attachment to the surface. Although there is no direct evidence, the only remaining site for adsorption to the surface is that of the nitrogen lone pair in the five-member ring.

. It is also possible that the molecule is attached through the indole nitrogen, as with pyridine on silver. The usual diagnostic for this is the appearance of a metal-nitrogen line (at about 239 cm^{-1} on Ag). However, this spectral region is obscured in our

samples by the intense phonon lines of the semi-conductor substrate, so this possibility cannot be confirmed in the present experiments.

The tyrosine spectrum in the region 500-1200 cm^{-1}, is shown in figure 5.12, with measured frequencies listed in table 5.4. Also listed are the observed resonance Raman frequencies[145] obtained from the liquid at 200 nm at pH-7. Also included are the results of a recent Raman spectrum[147] of the solid at 532 nm, which is listed just before the CdSe results. It can be seen that there is a strong correspondence between the quantum dot spectrum and the solid and liquid Raman spectra. The resonance Raman spectrum is relatively sparse, due to the fact that it is sensitive only to totally symmetric vibrations. Prominent in the Raman liquid spectrum is the well-known doublet at 834 and 857 cm^{-1}. This is due to the coincidence of the ν_1 ring-breathing mode with the first overtone of an out-of-plane bending motion of the ring ν_{16a}, and the relative intensities and frequencies may be attributed to a Fermi resonance[148]. This doublet is not observed in the quantum dot spectrum. Despite the fact that the –OH bend at 1251 is not observed, we do see the p-substituent stretch (C-O) ν_{7a} at 1218 cm^{-1}. The ν_{9a} ring stretch is observed considerably down-shifted at 1163 cm^{-1}, while the C-N stretch is up-shifted to 1068 cm^{-1}. With these exceptions, all other bands observed in the quantum dot spectrum and assigned to out-of-plane vibrations. These include the ν_{16b}, at 532 cm^{-1}, the ν_4, at 716 cm^{-1}, the ν_5, at 928 cm^{-1}, and the ν_{17a} at 961 cm^{-1}. The prominence of the usually unobserved (in SERS) out-of-plane vibrations is indicative of a molecular orientation with plane parallel to the quantum dot surface.

5.7.4 Discussion

The atomic force micrograph images of our surface (see figure 5.7) indicate that the average height of a dot is 8 nm, while the dot diameter is approximately 100 nm. This presents a picture of dots which have a cylindrical shape rather than spherical or hemispherical as previously discussed. The appearance of the micrograph is somewhat misleading since the vertical scale is not the same as that of the horizontal scale. Furthermore, due to the fact that the tip size is comparable to the dot size, the measurements of the horizontal dot diameter are not very accurate. However, using knowledge of the measured dot density (2.04×10^{8} dots/cm^2), assuming all the mass deposited in 2.5 ML (resulting in a total deposited volume of about 5×10^{-8} cm^3) contributes to the dots, and with the assumption that the dots have a cylindrical shape, we may make an independent estimate of the dot diameter. If the deposited CdSe layers are distributed evenly among the dots, we obtain a predicted diameter of 200 nm, which is consistent with the AFM measurement. This calculated diameter would be smaller if some of the CdSe deposited forms a wetting layer underneath the quantum dots. It is clear from the above results that the dots are neither spherical nor hemispherical, as the name might imply, but rather flat conical shapes with a height of 8 nm and diameter of approximately 110 nm. Any quantum confinement effects would be expected to take place in the short dimension, perpendicular to the surface, while parallel to the surface, it is likely that the properties of the dots are closer to those of the bulk semiconductor.

The further likelihood that the surface has been oxidized on removal from the molecular beam must be considered. Studies on a clean, smooth CdSe {001} surface[149] indicate that initially oxygen adsorbs only on Se atoms, and then with breaking of back

bonds, both selenium and cadmium oxides are formed. Part of the selenium oxide sublimes away (presumably in the form of SeO_2), leaving the surface rich in Cd=O. Bowen Katari, Colvin and Alivastatos[150] have examined this problem for quantum dot surfaces using X-ray photoelectron spectroscopy (XPS). Both the XPS data and thermodynamic considerations lead to the conclusion that $CdSeO_3$ is formed on the surface, although some Cd=O might also be present. In our case since the last layer is rich in Se, we expect that our quantum dots are capped with a layer of selenite, although it is possible that over time, as in the clean surface, SeO_2 sublimes leaving a surface richer in Cd=O. All the spectra shown here were obtained immediately after removal of our quantum dot samples from liquid nitrogen. In any case it is clear that to the extent that the molecules are adsorbed onto the CdSe surfaces, it is quite possible that they are adsorbed by means of the oxygenated species. Certainly, at least for adenine and tryptophan, where there is evidence for attachment through the $-NH_3^+$, it is reasonable that this is through bonding with negatively charged oxygen atoms.

The enhancement factor can now be estimated as was previously done (section 5.5). The intensity measurements were taken at 762 and 1016 cm^{-1} lines of tryptophan. These are chosen because they are relatively intense and isolated from other spectral lines. The intensity of the normal Raman spectrum of these lines are 10,000 and 7000 counts respectively, while from the surface enhanced spectra, we obtain 600 and 400 counts respectively. In both spectra the laser intensity was kept constant. The intensity ratio (I_{surf}/I_{soln}) is therefore approximately 0.06 in both lines. We assume a laser diameter of 10 μm and that about 1 cm of the path in the liquid is focused into the slit of the

spectrometer. In solution, this leads to a volume of about 10^{-6} cm^3, and therefore N_{soln} =7.5 x 10^{15} molecules scattering within this volume.

On the surface there are several possibilities, depending on the distribution of molecules, and their contributions to the enhancement. The two most likely situations are that only molecules adsorbed on the dots contribute to the enhancement, or that molecules adsorbed between the dots on the wetting layer, contribute as well, due to their proximity to the dots and quantum confinement effects of the wetting layer. In the latter case, the calculation is similar to that of a normal SERS surface. Assuming in a monolayer there are 2.5 x 10^{14} molecules/cm^2 in an area of 100 μm^2, we obtain N_{surf} = 2.5 x 10^8 molecules. This results in an enhancement factor of 1.8 x 10^6. On the other hand if we assume only molecules adsorbed on the cylindrical quantum dots contribute to the enhancement, we then give each dot a total area of $\frac{1}{4}\pi d^2 + \pi dh$ (including the circular top and the side) where d = 100 nm and h = 8 nm, the area per dot is 10^4 nm^2. Multiplying by the dot density and the number of molecules per unit area, we obtain N_{surf} = 5x10^6 molecules interrogated by the laser. This results in an enhancement factor of approximately 10^8. The factor of approximately 50 difference between the two calculations merely reflects the difference in surface area presented by the dots alone, as opposed to the total surface. Even if we take the more conservative value of 1.8 x 10^6 the enhancement for the II-VI CdSe quantum dots observed here is many orders of magnitude greater than that obtained for the II-V GaAs quantum dot system. Similar calculation of the enhancement factor in adenine with intensity measurements taken at the 1382 cm^{-1} line of adenine yields an enhancement factor of approximately 3x10^6

assuming the enhancement observed is from the molecule adsorbed on the quanum dots and 3 x 10^5 if enhancement is due to the wetting layer.

5.7.5 The Enhancement Mechanism

The calculated enhancement factor for CdSe quantum dots grown by MBE is quite large, and comparable to the enhancements obtained in noble metals. However, it is difficult to invoke the enhancement mechanism usually given for metals, namely the increased electric field near the metal surface caused by plasmon resonance excited by the laser light. As previously note in preceding sections, typical plasmon frequencies for semi-conductors lie too far in the infrared to be the cause of the effect seen here. Another contributing factor to metallic Raman enhancement has been identified as a charge transfer between molecule and metal. This is mediated by an interaction of the molecular electronic states with those of the metal conduction band[151,152]. The charge transfer resonance between the molecule and the quantum dot via a surface-bound ionized acceptor-exciton complex and interband or excitonic transitions due to proximity to the laser excition energy on the wetting layer, described in section 5.4 is also implicated here as well.

5.7.6 Conclusion

We have demonstrated that CdSe quantum dot assemblies, grown by molecular beam epitaxy (MBE) can provide efficient enhancement of a Raman signal from molecules adsorbed on the surface. This surface enhancement is estimated to be in the range of 10^5 to 10^6, comparable to that of noble metals. We have also analyzed the Raman spectra of several molecule of biological interest and been able to make certain inferences as to the mode of adsorption to the surface. In addition we have observed several sharp, narrow photoluminescence bands, which are attributed to the quantum dots, but are only observed by addition of the molecular layer. These results indicate that CdSe quantum dot system enable a high degree of molecular specificity and large Raman enhancement factor. This suggests a possible technique for sensitive detection and identification of biological molecules.

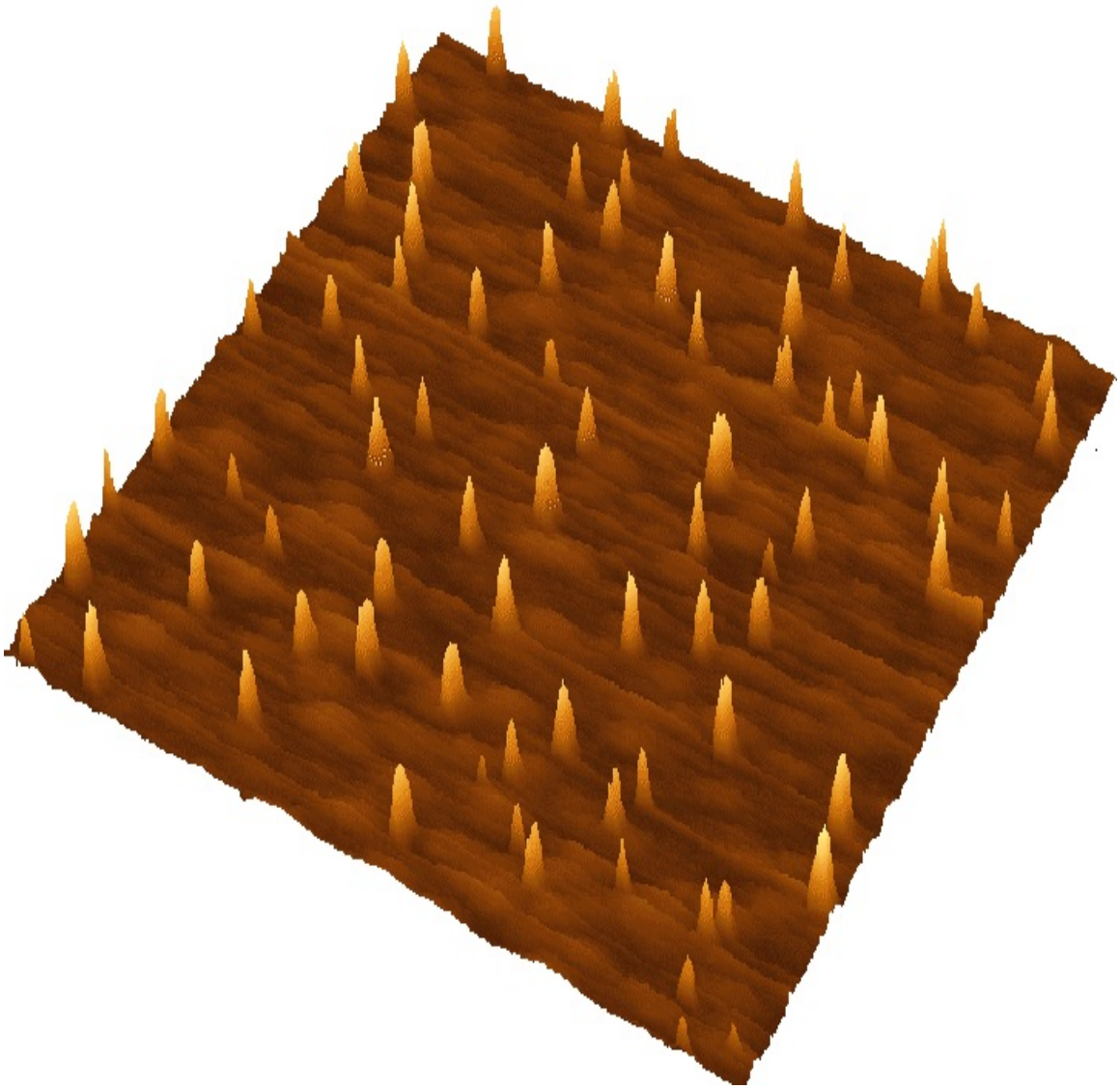

Figure 5.7. Three dimensional AFM image for uncapped QD with 2ML-CdSe nominal thickness and ZnCdMgSe barrier of approx. 2.6eV

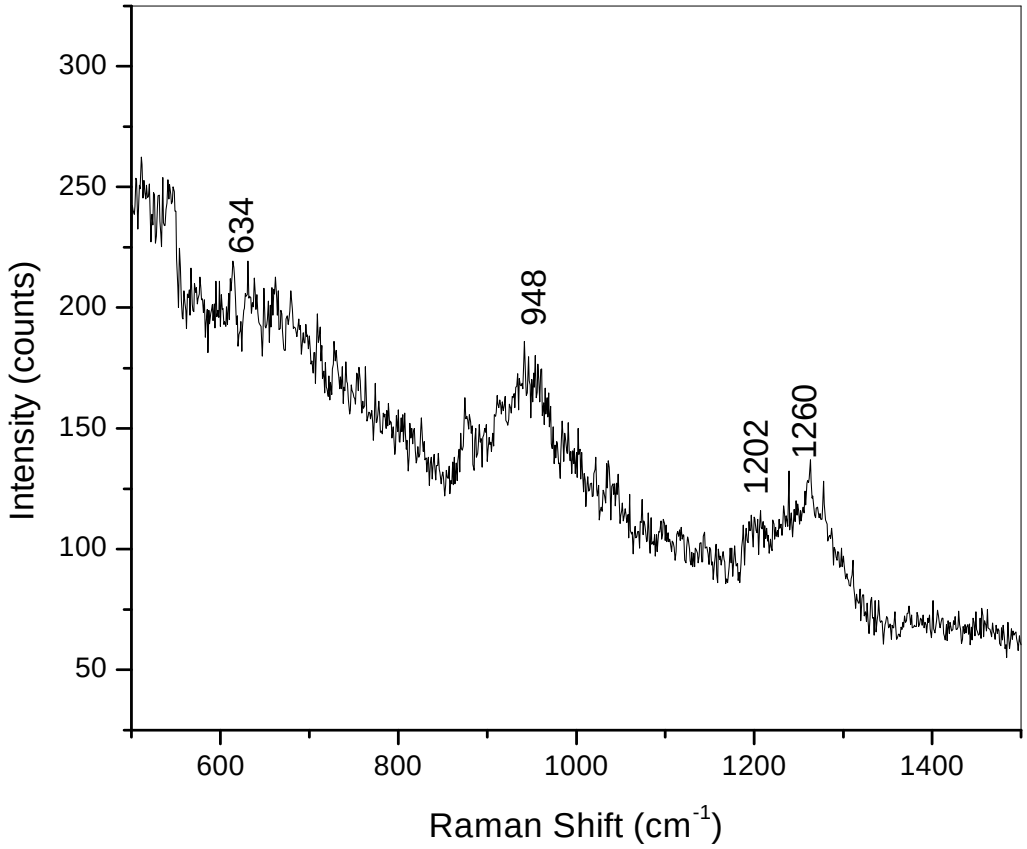

Figure 5.8 Raman spectrum of QD sample before coating with a molecule.

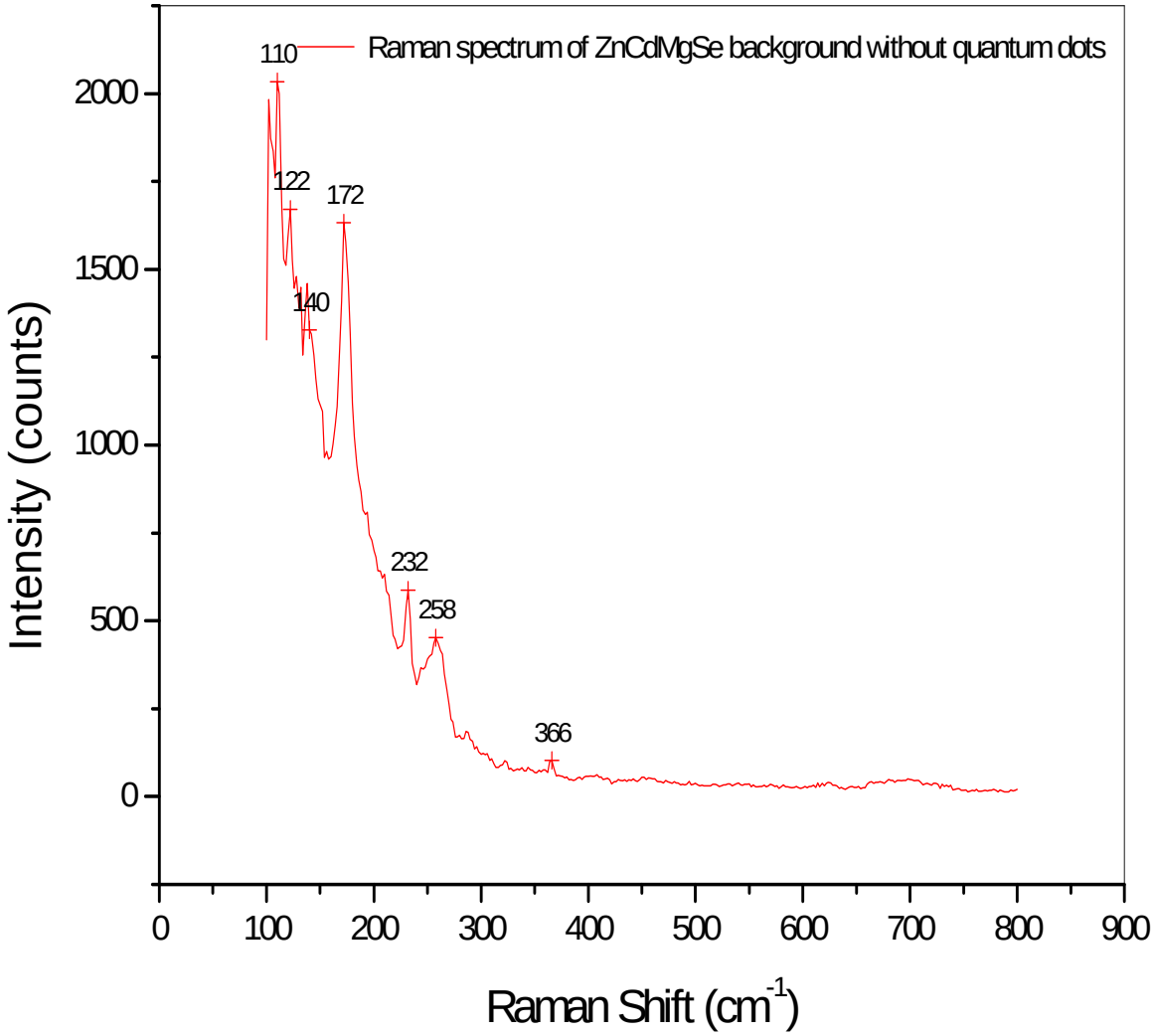

Figure 5.9 SERS spectrum of MBE grown ZnCdMgSe background without CdSe quantum dots

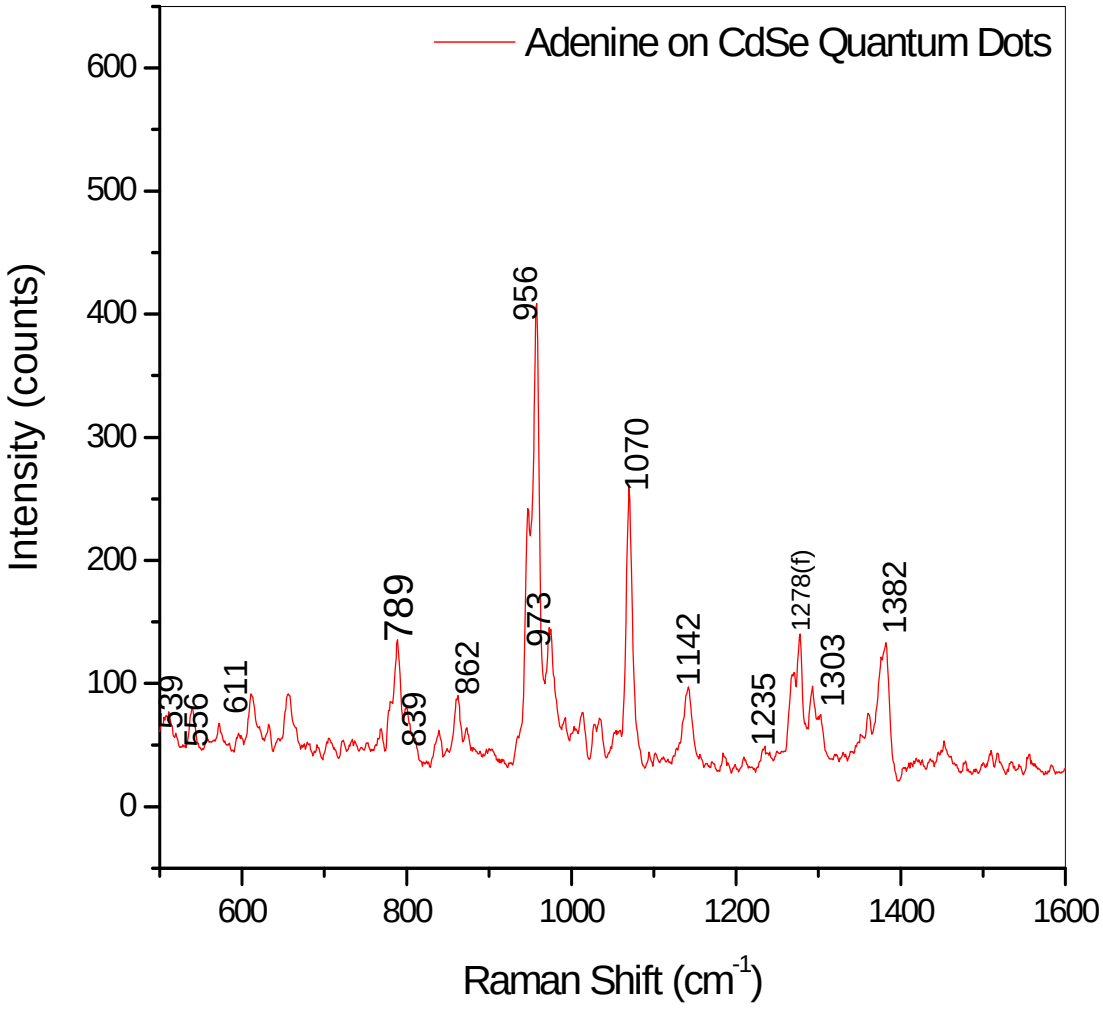

Figure 5.10 SERS spectrum of Adenine on MBE grown CdSe quantum dots

Table 5.2: Raman spectrum of Adenine on CdSe quantum dots excited at 488 nm.

NR-solid	Mode #	Description	SERS-632nm	CdSe-488nm
536	27,28	NH wag-oop	536	539
560	25	CH wag	553	556
623	24	Ring def	621	611
			690	
723	21	Ring breath	731	
797	20	Ring def-oop	788	789
839	19	CH wag-oop		839
				862
899	18	NCN def		903
942	17	NCN def	958	956(*f*)
974(calc)	16	CH wag-oop		973
1025	15	rock -NH_2	1029	
				1070
1126	14	CN str	1117	1142
1162	13	CH bend		
1234	12	rock -NH_2	1245	
1248	11	CH bend		1251
			1270	1278
1308	10	CN str		1303
1333	8,9	CH bend	1326	
1372	7	CH bend	1372	1382
1419	6	CN str	1399	
1463	5	sciss -NH_2	1460	
1483	4	sciss -NH_2		
1597	3	sciss -NH_2		
1613	2	CN str		
1674	1	sciss -NH_2		

Normal Raman (NR) of solid, Mode assignments and SERS at 632nm from: Giese, B. McNaughton, D., ***J. Phys. Chem. B,*** **2002, 106, 101-112.**

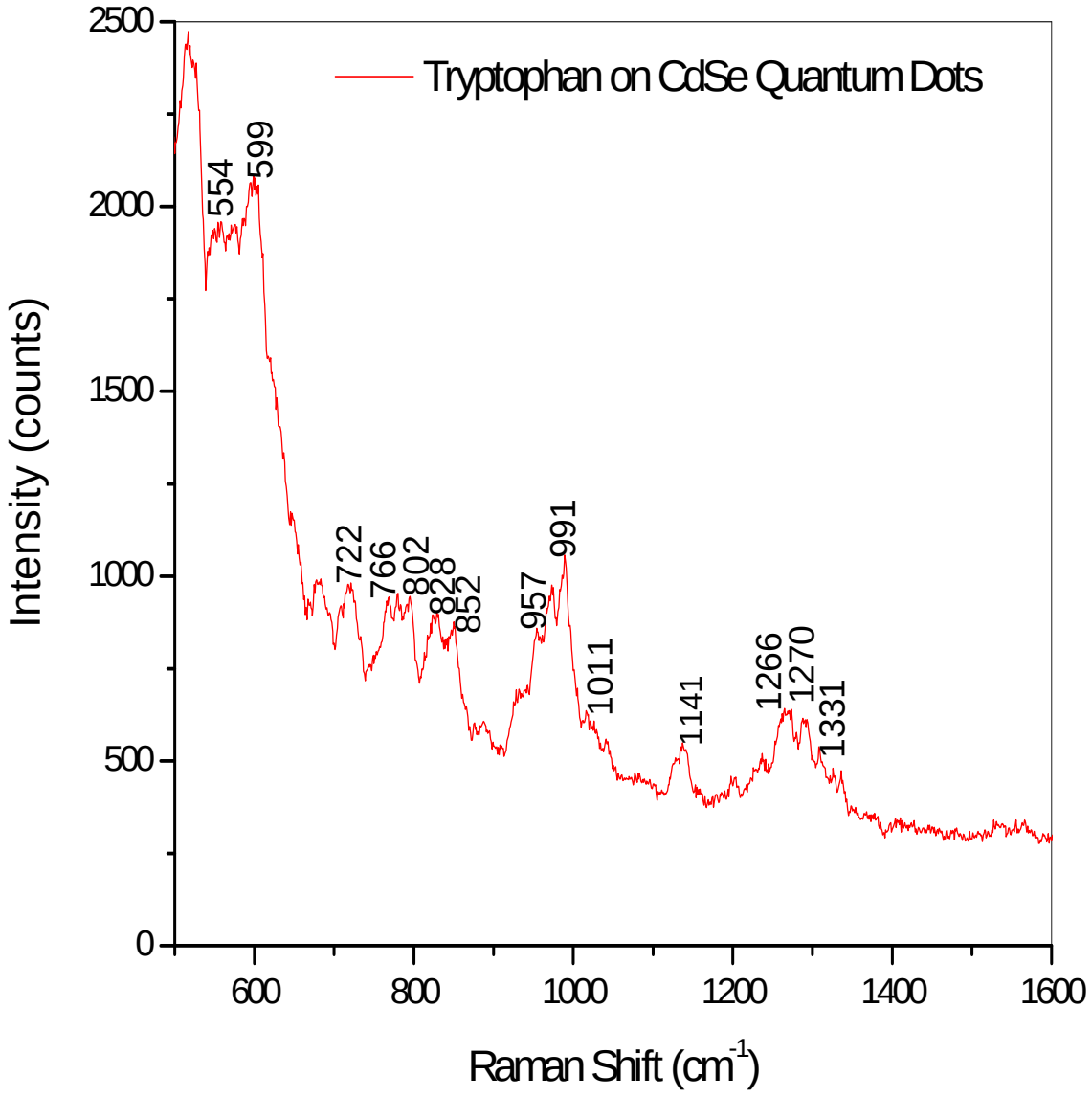

Figure 5.11 SERS spectrum of tryptophan on MBE grown CdSe quantum dots

Table 5.3: Raman spectra of Tryptophan on CdSe quantum dots excited at 488 nm.

Raman-liq 200 nm	Raman-Solid 488 nm	Description	IR-liq Zwitterion	Description	CdSe 488nm
			529	def,r,R	
	562		555	β-NH(r)	554
	580		581	β-NH(r)	
	608		613	β-CH	599
			640	def,r	
			660		
			694	def,r	
	716		725	def,r,R	722
762	764	ring-brth	763	β-CO_2^-	766
	786		794	β-CO_2^-	802
	830		821	def,r,R	828
	856		843	β-H,R	852
880	883	skel+NH	875	β-NH_3^+	895
	938		928	β-CH_2	
	970		955 calc		957(f)
	990		990 calc		991
1016	1017	ring-brth	1007	ν_{CN},β-NH_3^+	1011
	1060		1045	β-NH_3^+	
1127	1100	9b	1111	β-H,R	
1148	1148	15 or δNH	1153	ν_{CC}	1141
1238	1234	3	1226	β-CH,νR	
1256	1262		1273	νR	1266
			1283	νR	1270(f)
1305		5π	1316	β-CH_2	
1342	1340	14			1331
			1352	β-CH	
1361	1362	14π			
1434	1438	6π	1432	β-CH,νR	
1462	1470	19b	1457	β-NH_3^+	
1496		19a	1489	νR	
	1540		1526	νT	
1555	1558	ring-str	1569	β-NH_3^+	
1578	1584	8b	1578	νR	
1622	1626	8a	1625	ν_{as}-CO_2^-	

Spectrum from: Rava, R.P.; Spiro, T.G., *J.Phys.Chem*., 1985, 89, 1856-1861. IR spectrum of Zwitterion from: Cao, X.; Fischer, G., *J.Phys.Chem.A*, 1999, 103, 9995-10003. R-benzene ring, r-pyrrole ring, ν-stretch, β-bend

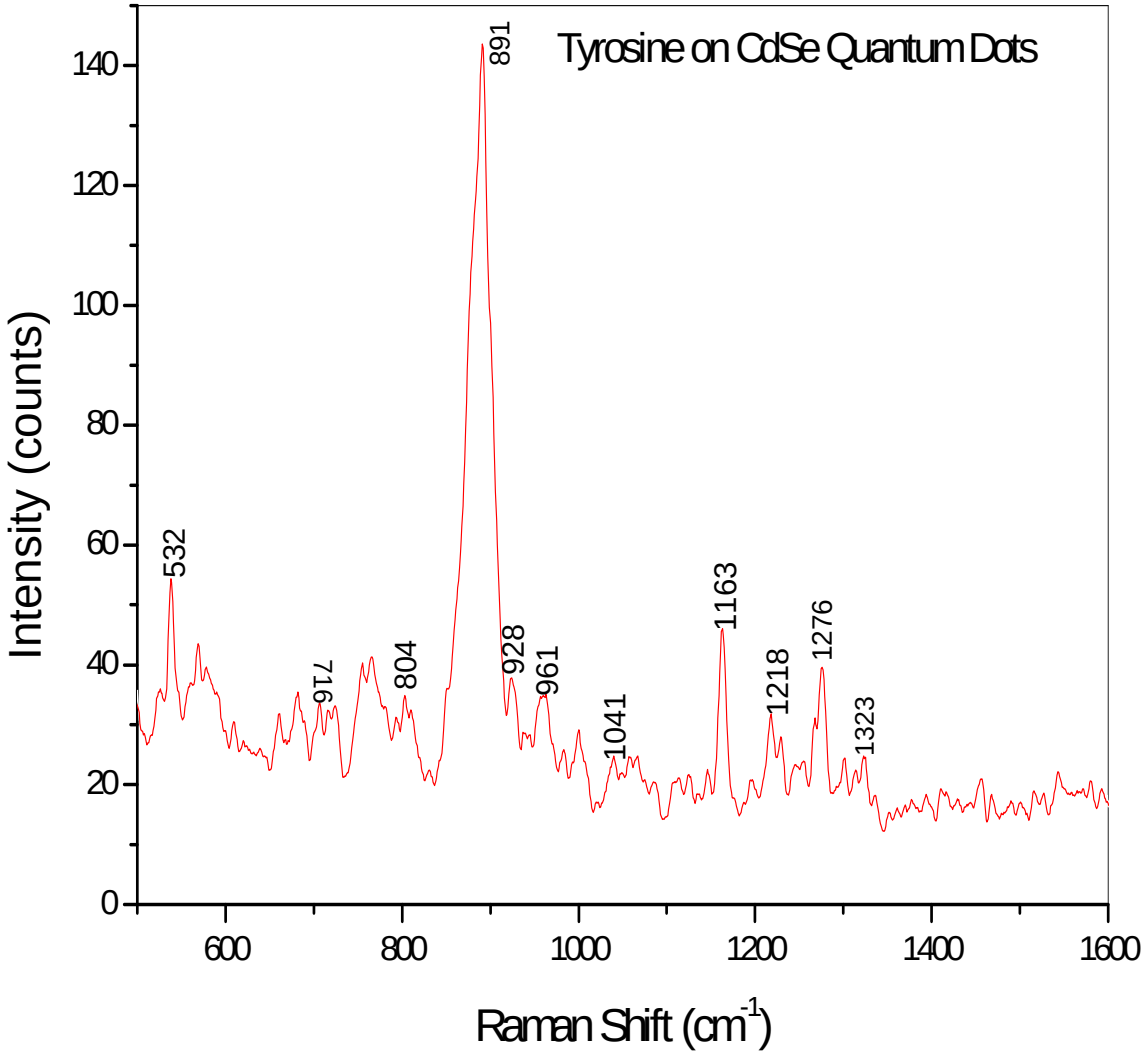

Figure 5.12 showing SERS of Tyrosine on MBE grown CdSe quantum dots

Table 5.4: Raman spectrum of Tyrosine on CdSe quantum dots excited at 488 nm.

Raman-liq pH-7 200 nm	Assmt	Raman-solid 532 nm	Assmt	CdSe 488 nm
		535	16b (oop)	532
		641	6b	
		714	4 (oop)	716
		739(IR)	12	
		797	-NH_2 wag	804
831	2X16a(oop)	828	1 (ring br)	
853	1 (ring br)	845	2X16a(oop)	
				891(f)
		939 (IR)	5 (oop)	928
		971	17a (oop)	961
		982	CH_2 rock	
		989	CH_2 rock	
		1046	C-N str	1041
1180	9a	1179	9a (ring str)	1163
		1200		
1210	p-subst-str	1213	7a	1218
		1251	-OH bend	
1263	7a	1263	14	
				1276(f)
		1329	13	1323
		1370	CH bend	
1443	19b	1437	19b	
1519	19a	1513 (IR)	19a	
1601	8b	1598	8b	
1617	8a	1616	8a	

Liquid Raman Spectrum from: Rava, R.P.; Spiro, T.G., *J.Phys.Chem*., 1985, 89, 1856-1861. Raman solid 532 nm: Grace, L.; Cohen, R.; Dunn,T.; Lubman, D.M.; de Vries, A.S., *J. Molec. Spectry*., 2002, 215, 204-219

Chapter 6. Raman and Surface-Enhanced Raman Spectra of Flavone and several Hydroxy derivatives

6.1 Introduction

Almost all flavone derivatives have been identified from botanical sources[152]. They are commonly found in vascular plants as phenyl-benzopyrones with different basic structures. Many of the flavonoids found in plants exist as sugar derivatives (glycosides)[153]. Owing to their active role in photosensitization, energy transport and cellular metabolism, many of flavone derivatives are ingredients for biochemical and pharmacological products used as human diet supplements[154-159].

Flavones and flavonols found in plants are yellow compounds and are the main components of a number of natural dyes used in textile dyeing since antiquity. Fustic, young fustic, quercitron, Persian berries, weld, dyer's broom and sawwort, which are important yellow dyes, all contain flavonoids such as quercetin, luteolin, fisetin, rhamnetin, genistein and morin[160]. Extracted from plants, they are easily hydrolyzed from the glycosides to their parent flavonoid and can be applied to textiles as mordant dyes.

Despite the fact that flavone forms the parent structure to most flavonoids, there is no Raman or surface-enhanced Raman spectral (SERS) data reported for flavone itself; one of the reasons for this may be the fact that flavonoid derivatives are more abundant in nature and are more extensively used in both medicine and dye industry than plain flavone. Low aqueous solubility may also be a factor. The structures of flavone and of some derivatives are shown in Fig. 6.1: for convenience in analysis and discussion, we designate the benzo ring in the chromone system as Ring A, the phenyl ring as Ring B and the pyrone ring as Ring C. Some of the previous works provide the infrared spectra

of flavone in carbon tetrachloride, dioxane and iodine solutions, and in Nujol boron tetraflouride complex[161]. Studies confirm that the higher wavenumber bands of flavone are dominated by the C=O and C=C vibrations, with bands at 1650, 1621, and 1605 cm^{-1} in CCl_4 and CCl_4-I_2 solutions. The BF4-nujol and plain nujol spectra confirmed the 1638 cm^{-1} band assignment to C=O and C=C vibrations.

As a member of flavonoid family, 3-hydroxyflavone (3-HF, flavonol) has been extensively studied for chemical and structural properties by UV,NMR, IR and PMR[162,163] and used in extensive studies of excited-state intramolecular proton transfer and photoisomerization by means of electronic spectroscopy and time-resolved fluorescence measurements[164-166]. Infrared spectroscopy has been widely applied to study the vibrational modes of 3-HF[167-171]. Unlike in flavone where the carbonyl absorption is at 1649 cm^{-1}, in 3-HF its wavenumber is lowered to 1610 cm^{-1} which overlaps with the C=C band. The IR spectra in the C–H and *O*–H stretching region were reported differently in various works[161,166,167], in which researchers concluded that there is no strong hydrogen bonding in 3-HF, as opposed to the 5-hydroxyflavone (5-HF) molecule. The hydroxyl stretching absorption was found at 3350 cm^{-1}.

Many studies have been reported on 5-HF, including IR, UV, NMR and proton-transfer fluorescence spectra[161,166,172-174]. The published IR spectra show that although in 5-HF the hydroxyl stretching band is broadened and displaced to lower wavenumbers (3000–2500 cm^{-1}) to an extent that it has almost disappeared, none of the compounds examined shows a marked lowering of the carbonyl wavenumber. Two possible canonical forms of 5-HF were reported, which explained the electronic behavior of the molecule and confirmed that the hydroxyl group forms a strong hydrogen bond between

the phenolic hydrogen atom and the negatively charged carbonyl oxygen atom. Carbonyl IR absorptions of 5-HF on KBr disk, Nujol mull, CCl_4 and dioxane solution were reported at 1653, 1651, 1652 and 1654 cm^{-1}, respectively. Solid-state IR spectroscopy revealed 5-HF vibrational modes with wavenumbers at 1617, 1590, 1550, 1473, 1457 and 1417 cm^{-1}, which are possibly associated with in-plane skeletal vibrations[166]. Common bands in the 1400–1000 cm^{-1} region have also been studied. Examination of the double bond region revealed C=C and C=O wavenumbers at 1620 and 1612 cm^{-1} respectively[161].

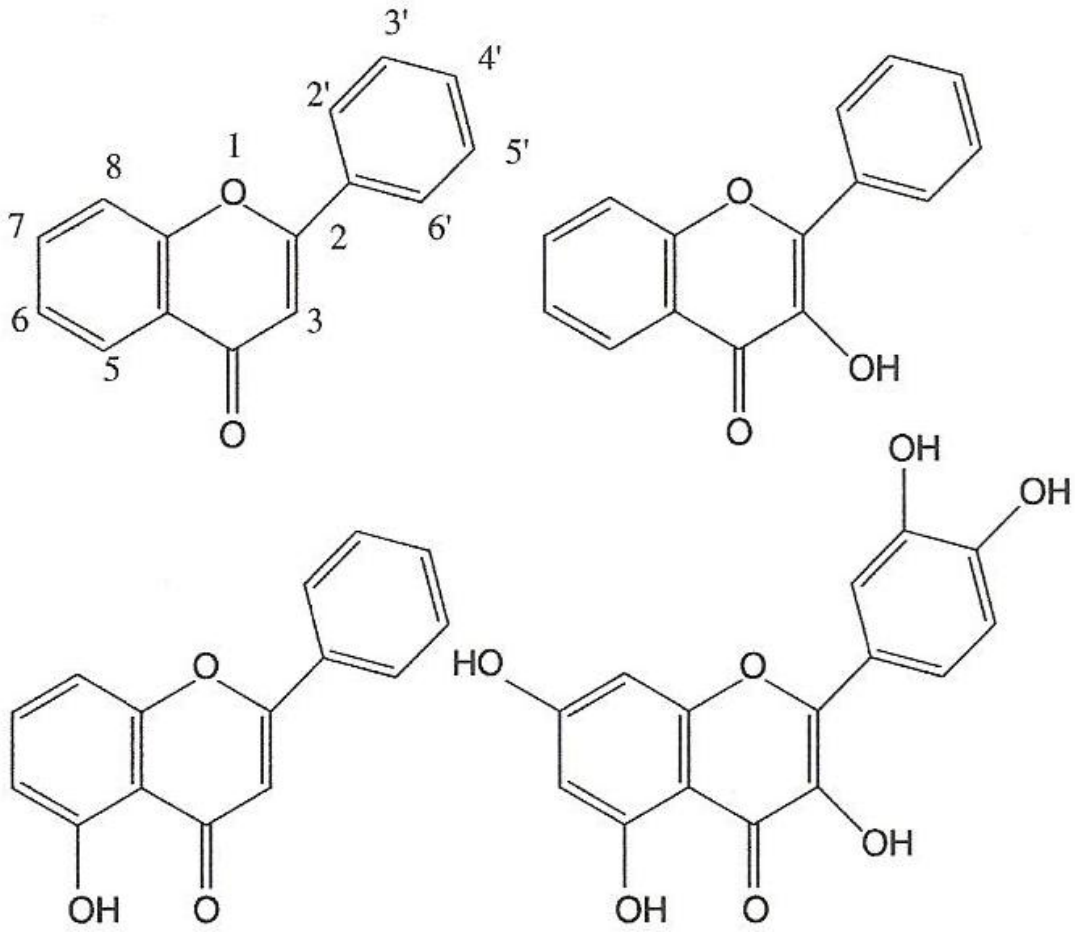

Figure 6.1. Flavone (upper left), 3-hydroxyflavone (upper right), 5-hydroxyflavone (lower left), and quercitin (3,5,7,3',4' pentahydroxyflavone (lower right). For convenience, the benzo ring in the chromone system was designate as Ring A, the phenyl ring as Ring B and the pyrone ring as Ring C.

One of the most biologically active and common dietary polyhydroxy-substituted derivative of flavonol, quercetin (3,5,7,30,40 pentahydroxyflavone Fig. 6.1), has been studied more extensively than any other flavonoid owing to its complex chemical structure and unique properties. Quercetin and its glycoside quercitrin are the main components of the natural dyestuff quercitron, extracted from the bark of the quercitron, or black oak (*Quercus velutina* Lam.); quercetin is also found in Persian berries, a dye derived from the berries of shrubs of the *Rhamnus* genus[161]. Raman, IR and pulse radiolysis techniques were successfully used to study the chelation properties of quercetin with Cu(II) ions[175]. The double bond region showed the C=O band at 1649 cm^{-1} and the C=C band at 1607 cm^{-1}. X-ray diffraction investigations reported the bond lengths, bond angles and torsional angles of quercetin, which suggested that the conformational changes with the physical state of the molecule are limited to an inter-ring link[176]. FT-Raman spectra of quercetin in the solid state and in solution have shown structural changes in themolecule depending on its physical state. Calculated and experimental wavenumbers[175] were compared after scaling the calculated values by a factor of 0.85 in the region between 600 and 1800 cm^{-1}. UV spectra also supported the calculated wavenumbers of quercetin.

Besides the wide studies on quercetin, there is almost no Raman or SERS work reported on flavone and 3- and 5-HF. A reference to unpublished work by Petroski *et al*[177]. reported 3-HF Raman bands at 1650 and 1625 cm^{-1}. The reason for the lack of Raman work may be the fact that these molecules are poorly soluble in water and show strong fluorescence upon excitation, which tends to obscure the normally weak Raman spectra. Recent studies suggest valuable application of SERS to microscopic samples in

the detection of molecules at extremely low concentration, which is particularly valuable in continuing research on biosensors[178], forensics[179] and art preservation[180]. Collaborative studies with the Metropolitan Museum of Art, of Raman spectroscopy of several natural dye constituents, with shows possible applications in the analysis of works of art. It is likely that Raman spectroscopy will be an efficient technique in the measurement of vibrational modes of flavone, 3-HF, 5-HF and quercetin at milli-, micro- and even nanomolar solutions. Furthermore, a detailed vibrational study and comparative analysis of these molecules could be useful to reveal the effects of hydroxy group substituents on structural and chemical changes of flavones. Reported in this chapter is the Fourier-transform Raman (FTR) spectra of all four molecules in the solid state as well as their SERS spectra in solution on an Ag colloid and, where possible, on an Ag electrode. All spectral assignments were aided by density functional theory (DFT) calculations. A comparative analysis of the spectra of all molecules of this study in relation to each other is also presented. These analysis became the base for future studies of other flavonoids, with the eventual aim of building a reference database of spectral assignments for most of the important derivatives. This database should be of great value in the development of pharmacological and art conservation studies.

Presented in the next section are details of the experimental procedure, as well as DFT calculations, followed by the analysis of flavone, 3-HF, 5-HF and quercetin spectra. The normal mode spectral assignments were aided by DFT calculations, and we compare the results of both the normal Raman (NR) spectrum and SERS spectra. A comparative analysis of several of the normal modes of each molecule, showing the effect of various hydroxy substituents on the basic flavone wavenumbers will then provide. Finally a

proof-of-concept experiment to demonstrate the feasibility of employing SERS in the analysis of a textile dyed with the natural dyestuff Persian berries, which consists mainly of quercetin will be provided. This concept has since been proven and applied to several natural dye pigments in art.

6.2 Experimental

The experimental setup for NR and electrochemical SERS studies has been described in previous papers[181]. A Spectra PhysicsModel 2020 BeamLock argon ion laser line at 488 nm was used as the Raman excitation source. The spectra were recorded with a Spex Model 1401 double monochromator with a resolution of 2 cm^{-1}. Photon-counting detection was used. The laser power was approximately 30 mW in the SERS experiment but only 5 mW in the NR experiment. Chemicals were purchased from the Aldrich Chemical Company Inc., and used as received.

The NR spectra of the solids were obtained in the region 100–4000 cm^{-1} directly from the pure powder samples. When possible, the 488 nm laser and Raman spectroscopy setup described above were used. In cases where the fluorescence of the dyes prevented the acquisition of a Raman spectrum, FT-Raman spectroscopy was carried out using a Bruker Ram II FT-Raman-Vertex 70 FT-IR microspectrometer. The 1064 nm line of a Nd: YAG laser was used as the excitation line. The resolution was set to 4 cm^{-1} in the backscattering mode. A liquid-nitrogen-cooled Ge detector was used to collect 100 scans for obtaining a good Raman spectrum. The laser output was kept at 150 mW for the SERS spectra and 50 mW for the solid samples.

Additionally, some SERS work on Ag colloids was carried out using a Bruker Senterra Raman microscope using 785 nm excitation with power at the sample ranging from 10 to 100 mW, a 1200 rulings/mm holographic grating and a CCD detector. The SERS spectra in an electrochemical cell were obtained at different applied potentials with an activated Ag electrode, which had various molecules adsorbed on it. In the SERS experiments, the sample cell consisted of a 99.999% pure silver working electrode, a Pt counter electrode and a saturated calomel electrode (SCE) as the reference. All potentials reported in this paper are quoted *versus* the SCE. For activating a Ag electrode, the polished Ag electrode was roughened by an oxidation–reduction cycle (ORC) pretreatment, which was accomplished in the solution of the flavone molecules (2×10^{-5} M) in 0.1 M K_2SO_4 aqueous solution by applying a potential pulse from -0.4 to 0.5V for 2 s. These solutions were made with doubly deionized, quartz distilled water. The molecule was adsorbed on the Ag electrode surface during the ORC. Non-adsorbed molecules were then washed from the electrode by distilled water. After the *ex situ* ORC pretreatment, the activated Ag electrode was placed in 0.1 M K_2SO_4 aqueous solution for carrying out SERS experiments at various potentials. The same spectra were also obtained with *in situ* ORC and direct recording of the SERS spectra in the flavone solutions. The ORC pretreatment and potential control during the SERS experiments were carried out by using an EG&G PARC Model 175 universal programmer and an EG&G PARC Model 173 potentiostat.

The Ag colloid was prepared following the method of Lee and Meisel[182] by reduction of silver nitrate (Aldrich 209139 silver nitrate 99.9%) with sodium citrate (Aldrich W302600 sodium citrate dihydrate). The colloid thus prepared shows an

absorption maximum at 406 nm and FWHM of 106 nm, as measured with a Cary 50 UV–vis spectrophotometer (after a 1 : 4 dilution with ultrapure water to keep the maximum absorbance within the instrumental range). To further concentrate the colloid for use, a volume of 10 ml of the original colloid was centrifuged at 5000 rpm for 2 min. The supernatant was discarded and the settled portion was resuspended in 1 ml of ultrapure water. All glassware was cleaned with Pierce PC54 cleaning solution and rinsed with ultrapure water and finally in acetone and methanol. This method proved to be as effective as the use of aggressive cleaning agents such as aqua regia or piranha solution, and was preferred for health and safety reasons. Only ultrapure water was used for the preparation of the various solutions. SERS measurement were made simply by adding 1 μl of the dye solution to a 2 μl drop of the colloid deposited on a gold coated microscope slide, followed by addition of 2 μl of a 0.2 M KNO_3 solution. Raman measurements were made directly from the drop using a 10 or 20d microscope objective and focusing on the microscope slide surface. SERS spectra could be obtained 2 or 3 min after addition of the KNO3 and remained constant in quality until the evaporation of the liquid.

DFT calculations were performed with Gaussian 03[183] at the B3LYP level of theory and employing the 6-31CGŁ basis set. The geometry optimization resulted in a planar geometry, and no imaginary wavenumbers were observed in the calculated spectrum. This basis set was chosen to be consistent with earlier work, in which the fit obtained was excellent (see below). The basis 6-311GŁ was also tried, which gave an equally good wavenumber fit but with lesser ability to reproduce intensities, which shows the effect of the diffuse functions in the calculation. This was especially true, for example, with the 1544 cm^{-1} line of quercitin, which is intense in the spectrum and using

the former calculation, but is quite weak in the latter calculation. A further exploration using the hybrid functional PBE0 and 6-31CGŁ basis set was carried out for quercitin. This gave essentially the same results as the B3LYP/6-31CGŁ calculation, but required considerably more computer time and memory. In general, the vibrational normal mode assignments were based on the best-fit comparison of the calculated Raman spectrum with the observed NR spectrum. Where needed, a slight scaling of the calculated spectrum was utilized (usually 0.96–0.99). In instances where there was spectral congestion, such as in the carbonyl stretch region (near 1600 cm^{-1}), the relative intensities of the calculated spectra were matched to those of the observed spectra, so that the most intense calculated lines were assigned to the most intense observed lines.

6.3 Results

6.3.1 Flavone

The NR spectrum of solid flavone along with the calculated DFT spectrum is shown in Fig.6.2 (200–1800 cm^{-1}). The wavenumber scale of the DFT spectrum was scaled by a factor of 0.98 in order to obtain the best fit of the calculated spectrum with the experimental one. The observed and calculated wavenumbers are listed in Table 6.1. In the low wavenumber region, we observe an excellent match of the spectrum with the calculated modes. The most intense peaks are well fitted (such as the modes υ_{15}, υ_{17} and υ_{22}). Only a few of the calculated wavenumbers do not match the observed ones in the low wavenumber region, such as at 745 and 888 cm^{-1}. This may be explained by the fact that the signal-to-noise ratio in this region is low and therefore the assignments are uncertain. In the higher wavenumber region, almost all the intense lines correspond to the

calculated features. The most intense peak in the spectrum at 1634 cm^{-1} corresponds to the υ_{65} mode calculated at 1627 cm^{-1}. Nearby is also an intense line at 1603 (υ_{63}) cm^{-1}. Both these are assigned to a combination of C=O and C_2 C_3 stretching vibrations. The intense lines at 1621 (υ_{64}) and 1570 (υ_{60}) cm^{-1} are due to in-plane ring stretching combined with a C_4–O stretch.

The colloid spectrum of flavone is shown in Fig. 6.5 (200–1800 cm^{-1}) along with the NR spectrum. Recorded also is a spectrum of the plain reduced citrate colloid (Fig. 6.4) as a background[184]. This shows that several of the bands observed in the flavone-colloidal spectrum, namely, peaks at 225, 952, 1030 and 1403 cm^{-1}, correspond to citrate vibrations. Despite the background interference, the peaks of flavone vibrations are still intense enough to show a good fit with the Raman spectrum of the solid compound. Some of the best matches are at 675, 1002 and 1195 cm^{-1}. As mentioned above, in the carbonyl region, however, weakened relative intensity of C=O and C_2 C_3 stretch in the colloid spectrum of flavone compared to a higher intensity of solid flavone, was observed. In the NR spectrum, it will be recalled, these are the most intense peaks, while on the colloid, they are not significantly stronger than many other observed peaks. This is probably due to a weak attachment of the rings of the flavone molecule to colloidal particles. However, observation for the other molecules in this study, shows much stronger SERS spectra than for the flavone. They are in fact so strong that the colloid background lines observed in the flavone are obscured. Furthermore, after repeated attempts, no spectrum of the flavone on a silver electrode could be observed, although this was easily observed in the other molecules. This was interpreted to mean that the presence of an OH group in the 3- or 5-position facilitates strong chemical

binding to the Ag surface, which is not possible in the unsubstituted flavone, leading to a relatively weak SERS spectrum.

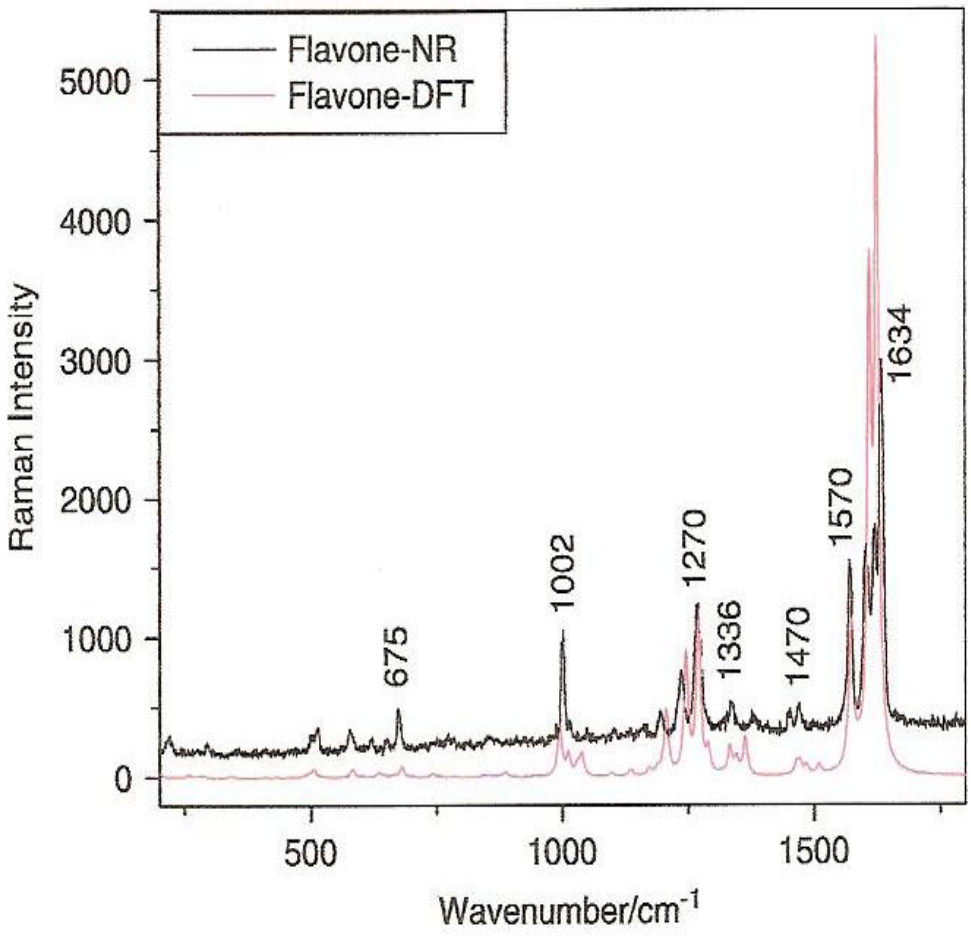

Figure 6.2. Normal Raman spectrum of flavone powder (dark) and density functional theory calculation (light).

Table 6.1. Wavenumbers (in cm_1) and assignments of the Raman and SERS spectrum of flavone. The DFT wavenumbers are scaled by a factor of 0.98

Mode no	Description of modes (flavone)	DFT (0.98) (cm^{-1})	Calc. Int.	NR (cm-1)	Colloid (cm^{-1})
6	Ring C, C-C deformation (oop)	202	0.1	-	-
7	Rings B, A and C stretch (ip)	262	6	-	-
8	Rings A, G def; Ring C=O def (oop)	282	0.9	-	-
9	Ring C; C-O bending (ip)	290	2	295	-
10	Ring B, bending; Ring C: C-) bending (ip)	321	2	-	346
11	Ring B, def (oop)	411	0.7	-	-
12	Ring C, C –C def (oop)	434	0.4	-	449
13	Ring A, B and C, def (oop)	467	0.5	-	-
14	Ring C, def (ip)	498	5	501	-
15	Ring A, B, C, C-C def	509	12	511	-
16	Ring A and C def (oop)	526	0.5	-	520
17	Ring A, B. C. C-C def	585	12	577	564
18	Ring A, B and C def (ip)	606	0.8	621	614
19	Ring B, def (ip)	638	7	652	-
20	Ring A and B, CH bending; Ring C, C2 bending (oop)	649	4	-	-
21	Ring C, CH bending; Ring A and C, def (oop)	667	3	-	-
22	Ring A, B and C, def (ip)	684	15	675	680
23	Ring CB, C-C def	703	1	-	-
24	Ring A, B, C, C-C def	745	6	-	746
25	Ring A, B, C-H (oop) bend	761	0.9	-	-
26	Ring A, B and C, C-H bending	785	0.8	-	-
27	Ring A, B, C-H (oop) bend	792	0.7	-	802
28	Ring A, B, C, C-C def	846	2	-	838
29	Ring B, C2’, C3’, C5’, C6’; Ring C, C3 bending (oop)	857	3	856	-
30	Ring A, B and C def (oop)	878	2	-	-
31	Ring C, C2-O stretch; Ring A and B def (ip)	888	5	-	-
32	Ring A, C-H (oop) bend	891	3	-	-
33	Ring B, bending (oop)	947	1	-	929/952
34	Ring A, C-H bending (oop)	984	0.2	-	-
35	Ring B, C-H (oop) bend	992	2	-	-
36	Ring A, B and C, C-C stretch	998	74	1002	1005
37	Ring A, c-H (oop) bend	1012	0	-	-
38	Ring B, def; Ring A and C, C-C stretch	1014	27	1013	-
39	Ring B, C-H bending (oop)	1016	3	-	-
40	Ring A and B, C-C stretch (ip)	1032	16	1032	1030

41	Ring B, C-H (ip) bend	1041	30	1048	-
42	Ring B, C-C stretch (ip)	1094	0.4	-	1098
43	Ring A, def; Ring B, C-C stretch (ip)	1101	5	1100	-
44	Ring A, C-H (ip) bend	1138	11	1143	-
45	Ring A, C-C stretch (ip)	1174	9	1162	1170
46	Ring B, C-H (ip) bend	1191	10	-	-
47	Ring B, C-H (ip) bend	1207	74	1195	-
48	Ring A and B, C-C stretch,; Ring C, C-01 stretch	1209	22	-	-
49	Rings A and C, C-C (ip) def	1247	174	1235	1244
50	Ring A, B and C, C-H bending (ip)	1271	232	1270	1256
51	Ring A and B, C-H (ip) bend;	1292	34	-	-
52	Ring A and B, C-H (ip) bend;	1318	2	-	-
53	Ring A, B and C, C-C stretch	1335	40	1336	1322
54	Ring A and B, C-H (ip) bend;	1348	22	-	-
55	Ring A, CC trigonal stretch	1365	54	1377	1359
56	Ring B, CH (ip) bend;	1466	16	1452	1403
57	Ring A, CH (ip) bend	1473	15	1470	-
58	Ring A, CH (ip) bend	1486	13	-	-
59	Ring B, CH (ip) bend;	1509	13	-	1522
60	Ring A, B, and C, C-C and C4-O stretch (ip)	1573	28	-	-
61	Ring A, quinoid stretch; C=O stretch	1575	195	1570	1556
62	C=O stretch; in-phase-C2=C3 stretch	1589	10	-	-
63	Ring B, quinoid stretch	1589	664	1603	1603
64	Ring A, B, and C, C-C and C4-O stretch (ip)	1621	12	1621	1625
65	C=O stretch; out-of-phase C2=C3 stretch	1627	994	1634	1636
66	Ring A and B, CH stretch	3105	-	3075	2929
67	Ring A and B, CH stretch	3113	-	3075	2929
68	Ring A and B, CH stretch	3115	-	3075	2929
69	Ring A and B, CH stretch	3119	-	3075	2929
70	Ring A and B, CH stretch	3130	-	3075	2929
71	Ring A and B, CH stretch	3130	-	3075	2929
72	Ring A, CH stretch (ip)	3143	-	3075	2929
73	Ring B, CH stretch	3143	-	3075	2929
74	Ring B, CH stretch (ip)	3154	-	3075	2929
75	Ring C, C3-H stretch (ip)	3160	-	-	-

ip: in-plane; oop: out-of-plane.

6.3.2 3-Hydroxyflavone

According to previous IR results[166-170], the presence of a hydroxy group in the 3-position lowers the wavenumbers of both the carbonyl and C_2 C_3 stretching modes, so that the band at 1610 cm^{-1} in FT-IR (1594 cm^{-1} in NR and SERS) represents the decreased double bond character of the carbonyl group and the aromatic character of the pyrone ring, i.e. the overlapping of C=O with C=C. The band at 3070 cm^{-1} in the NR spectrum can be attributed to an unsaturated C–H stretch. The band at 1351 cm^{-1} in FT-IR (1352 cm^{-1} in NR and 1354 cm^{-1} in SERS) is attributed to an *O*–H in-plane deformation. The bands in the region from 1400 to 1600 cm^{-1} are associated with aromatic in-plane skeletal vibrations, double bond character of the carbonyl group and the aromatic character of the pyrone ring, i.e. the overlapping of C=O with C=C. The Raman spectra of 3-HF have been considered in more detail in previous studies[185,186]. To facilitate comparison with the other molecules, we have abstracted some of the results here. In Fig. 6.5 we compare the results of the NR spectrum of the powder sample with the spectrum calculated from the DFT results. Detailed measured and calculated wavenumbers are listed in Columns 3 of Table 6.2. The raw wavenumbers from the calculation have been adjusted by a factor of 0.98.

It can be noticed that the calculated spectrum provides an excellent fit to the observed result. This indicates that the assignments given in the first two columns of the table are most likely correct. Column 1 is the normal mode identification number from the DFT calculation, and in Column 2 is a brief description of the largest vibrational contributions to the normal mode. Most of the lines between 1305 and 1509 cm^{-1} involve the in-plane CH bending vibration.

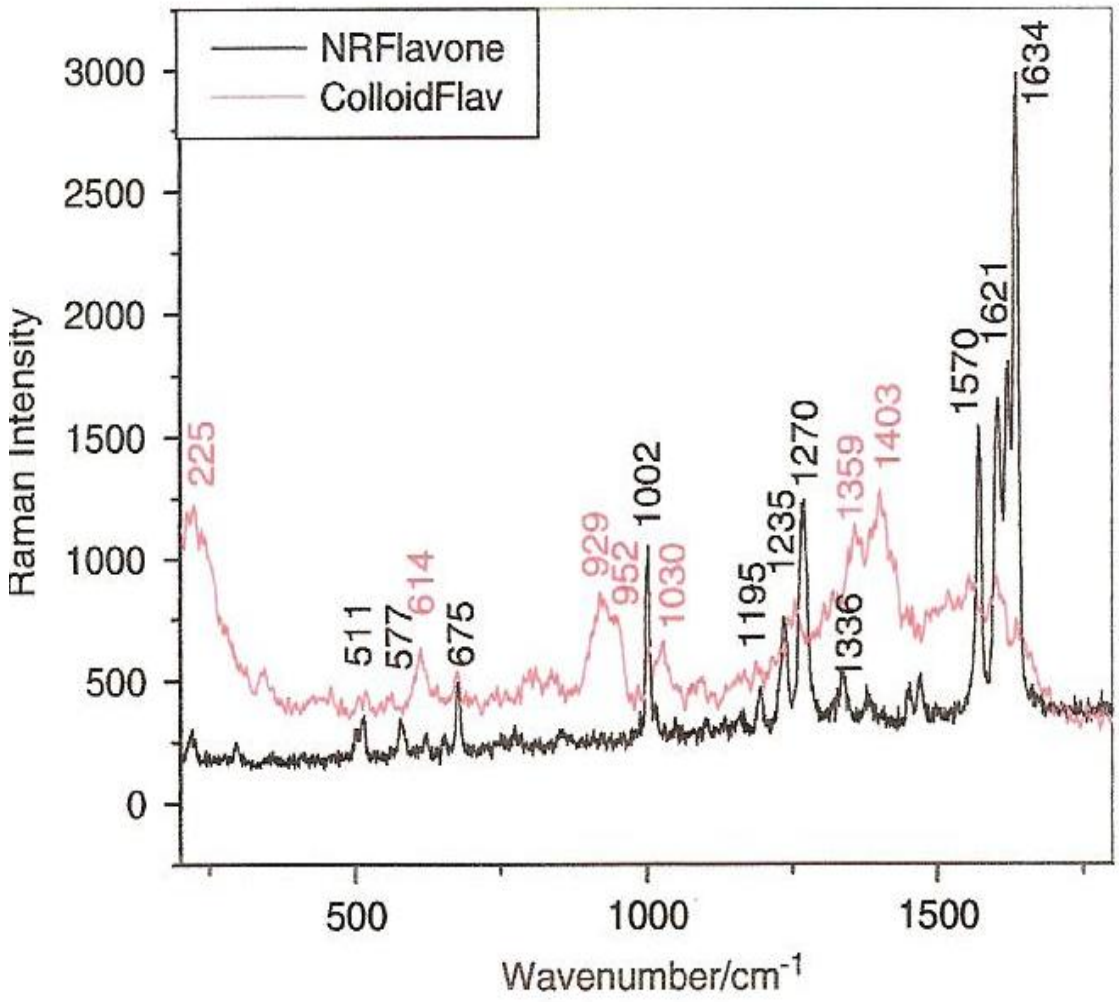

Figure 6.3. Comparison of the normal Raman with the colloid SERS spectrum of flavone in the region 200–1800 cm^{-1}.

.

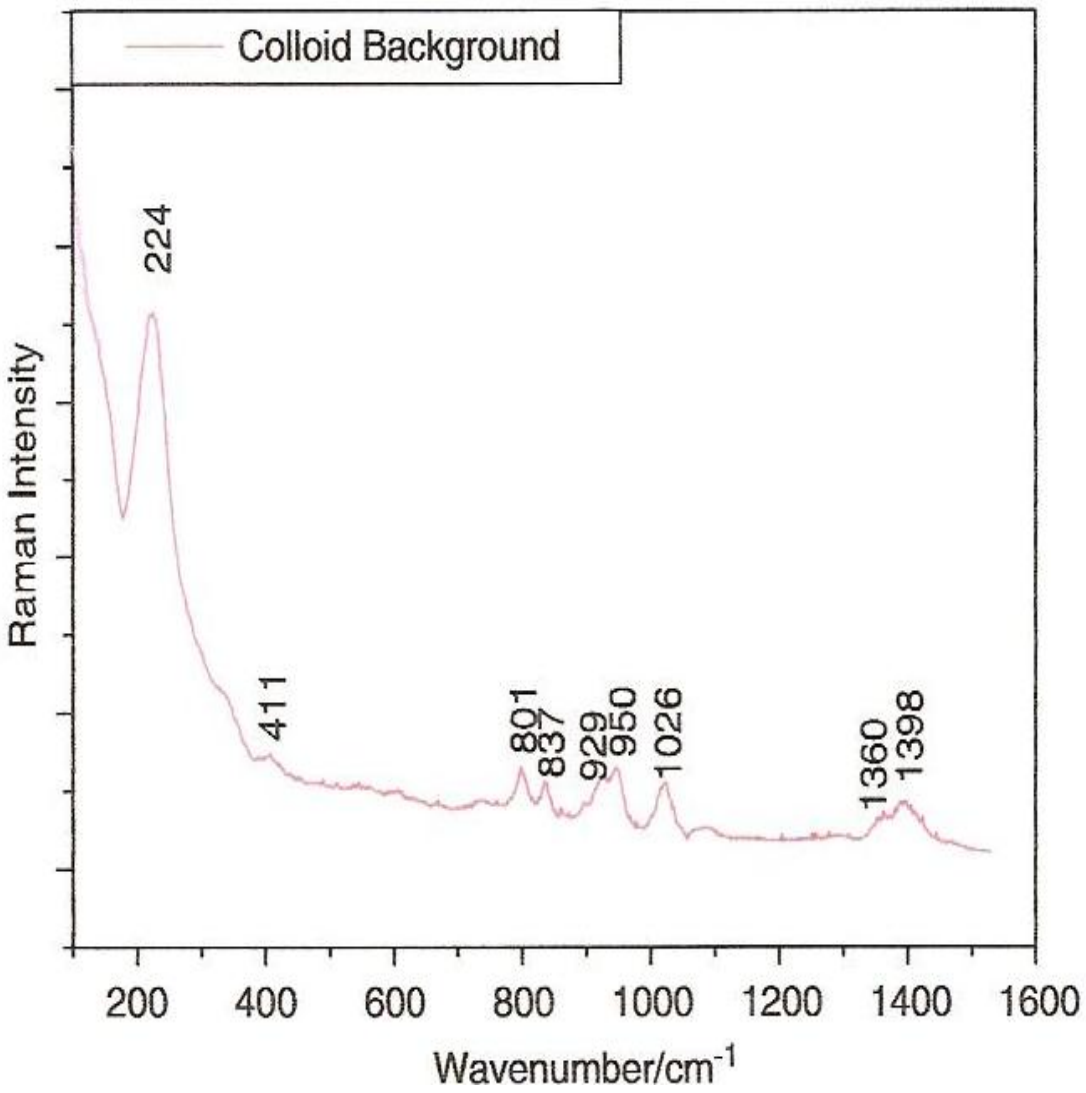

Figure 6.4. SERS of colloid-citrate background without adsorbed molecule

Note also that, except for the band at 1594 cm^{-1} (υ_{64}), all the bands between 1562 and 1619 cm^{-1} involve the C=O stretch and the C_2 C_3 stretch, with some degree of *O*–H bend. In order to examine the differences between the SERS spectrum on a colloid and that on the electrode, the spectra of both is present in Fig. 6.6. By and large, the spectra are quite similar, except that the line at 1527 cm^{-1} (υ_{62}) is very intense on the colloid and weak on the electrode. Furthermore, the 1405 cm^{-1} (υ_{58}) and 516 cm^{-1} (υ_{17}) bands are

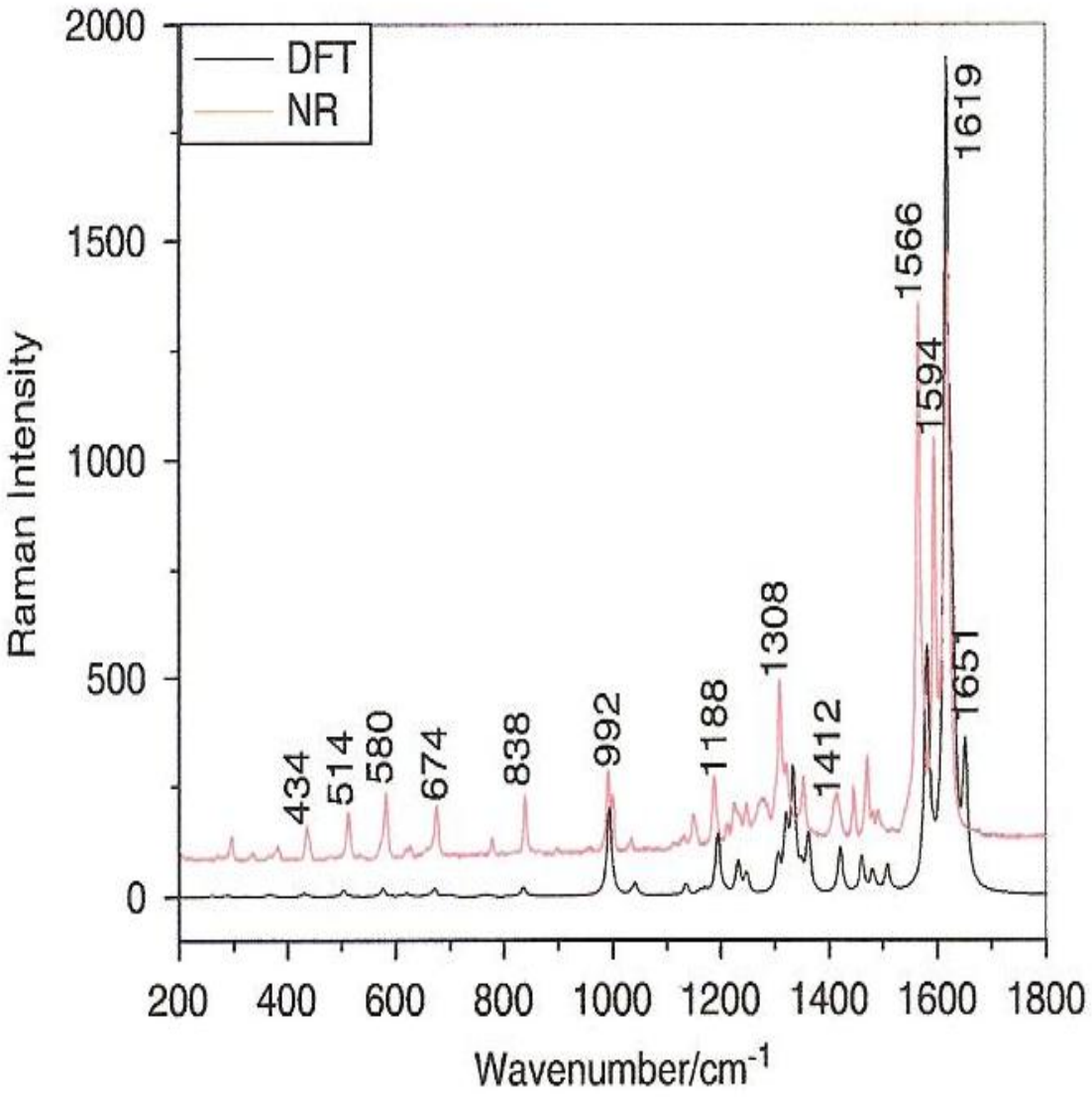

Figure 6.5 Comparison of normal Raman spectrum and density functional theory calculation for 3-hydroxyflavone in the region 200–1800 cm^{-1}.

similarly much stronger on the colloid. The latter vibration involves C–C in-plane deformation of the three rings, while the two at higher wavenumbers are due to C–H in-plane bending motions. These higher wavenumber modes also involve C–*O*–H bending, and a much stronger interaction on the electrode of a positively charged Ag ad-ion with the oxygen atom of the C–O bond in Ring C might damp the Ring C motion.

Table 5.2. Wavenumbers (in cm^{-1}) and assignments of the Raman and SERS spectrum of 3-hydroxyflavone. The DFT wavenumbers are scaled by a factor of 0.98

Mode no.	Density functional calculations (cm^{-1}) Description		NR (cm^{-1}) (Solid)	SERS (cm^{-1}) at -0.45 V	SERS (cm^{-1}) Colloid	FT-IR (KBr)
10	Ring B, C-OH (ip) rock	321	296	304	307	-
12	C - OH bend; C=O bend	367	380	390	390	-
15	Ring C, C-C deformation	431	434	454	455	-
17	Ring A, B, C, C-C deformation	504	514	516	516	-
19	Ring A, B, C. C-C deformation	576	580	578	575	-
21	Ring B, C-C deformation	619	624	618	620	-
24	Rings A, B, C, C-C deformation	670	674	672	671	-
27	Rings A, C, C-C def; C-O-C stretch	698	-	712	711	704
28	Rings A, B, C-H (oop) bend	731	-	-	-	-
30	Rings A, B, C-H (oop) bend	766	780	-	789	775
31	Rings A, B, C, C-C deformation	834	838_s	842_s	842	839_w
33	Ring A, C-H (oop) wag	859	-	-	-	864_m
34	OH Bend; Rings A, B. C. C-C def	890	899	900_m	900	898_s
35	Ring B, C-H (oop) wag	923	-	-	-	-
36	Ring A, C-H (oop) wag	956	-	946_{vw}	-	930_w
40	Rings A, B. C, C-C def	994	992_s	992_s	994	1034_m
41	Rings A, B, C, C-C def	996	1000_s	1000_s	-	-
43	Ring B, C-H (ip) wag	1041	1034_w	1028_{vw}	1032	1034_m
44	Ring B, C-H (ip) wag	1091	-	1078_{vw}	-	1078_m
46	Ring A, C-H (ip) wag	1137	1134_w	1116_w	1117	1130_s
48	Ring B, C-H (ip) wag	1170	1148_m	1150_s	1153	1155_w
49	C-OH stretch; Ring B, C-H (ip) wag	1194	1188_s	1186_s	1186	1184_w
50	C-OH stretch; Ring B, C-H (ip) wag	1208	1212_w	1218_{sh}	1213	1211_s
51	Ring C, C-C stretch	1233	1226_m	-	1233	1224_w
52	Rings B and C, C-C (ip) def	1248	1246_m 1278_m	1248_s	-	1247_w 1286_s
53	Rings A and B, C-H (ip) wag; O-H bend	1305	1308_s	1298_{sh}	1299	1306_s

54	Rings A and B, C-H (ip) wag; O-H bend	1321	1320_{sh}	1316_{s}	1316	1321 w
55	O-H (ip) bend	1332	-	-	-	-
57	OH (ip) Bend; Ring A, CC trigonal Stretch	1360	1352_{s}	1354_{m}	1355	1351_{s}
58	Rings A and B, CH (ip) wag; OH Bend	1421	1412_{s} 1444_{s}	1404_{s} 1430_{s}	1405 1430	1416_{s} 1445 m
59	Ring B, CH (ip) wag; OH Bend	1460	1470_{s}	1457_{s}	1461	1471_{s}
60	Ring A, CH (ip) wag	1481	1482_{w}	1482_{sh}	-	1481_{s}
61	Ring A, CH (ip) wag	1489	1490_{m}	1498_{s}	1491	1491_{s} h
62	Ring B, CH (ip) wag, OH Bend	1509	-	-	1527	-
63	Ring A, ip def; C=O Stretch; OH Bend	1581	1566_{vs}	-	1574_{w}	1562_{s}
64	Ring B, quinoid Stretch; OH Bend; C_2=C_3 Stretch	1590	1594_{vs}	1594_{s}	1592	1602_{s}
65	C=O Stretch; C_2=C_3 Stretch	1617_{vs}	1619_{vs}	-	-	1610
66	Rings A, b, C ip def	1627	-	-	-	1627 w
68	C=O Stretch, OH Bend; C_2=C_3 Stretch	1651	-	-	-	1647 vw
69	Ring B, CH stretch	3119	-	2860_{w}	-	-
70,71	Rings A and B, CH stretch	3130	-	2910_{w}	-	-
72,73	Rings A and B, CH stretch	3143	3070_{m}	3070_{vw}	-	-
75	Ring B, CH stretch	3160	-	3200	-	3211_{s}
78	OH stretch	3420	-	-	-	-

ip: in-plane; oop: out-of-plane

The most interesting result is illustrated in Fig. 6.7, where the NR spectrum of 3-HF is compared with that of the SERS on the colloid in the spectral region between 1000 and 1800 cm^{-1}. It was observed that the intense NR bands at 1566, 1594 and 1619 cm^{-1} (υ_{63} υ_{65}) were immediately suppressed on the surface, whereas the lines at 1405, 1491 and 1527 cm^{-1} (υ_{58}, υ_{61}, υ_{62}) become the most intense lines in the spectrum. The suppressed lines have either a strong C=O stretch coupled with a C_2 C_3 stretch or an *O*–H bend, while the surface-enhanced lines all involve the C–H in-plane wag. These results (in addition to the concomitant results on the Ag electrode) indicate strongly that the molecule is attached to an Ag ad-atom on the metal surface, reducing the intensity of the

modes involving C=O and C_2 C_3 stretch. The strong enhancement of the C–H in-plane wags indicates that the planar rings involved are oriented perpendicular to the metal surface. This is consistent with the suppression of the 1527 cm^{-1} band in the SERS on the Ag electrode, where an Ag ad-ion could be involved in the bonding of the – OH molecule to the surface. Note also that the lines at 455 (υ_{15}), 516 (υ_{17}), 671 (υ_{24}) and 711 (υ27) cm^{-1} are greatly enhanced on the colloid in comparison to the most intense lines of the NR spectrum. These lines involve in-plane ring C–C deformations. A similar result for the remaining two molecules studied here was observed.

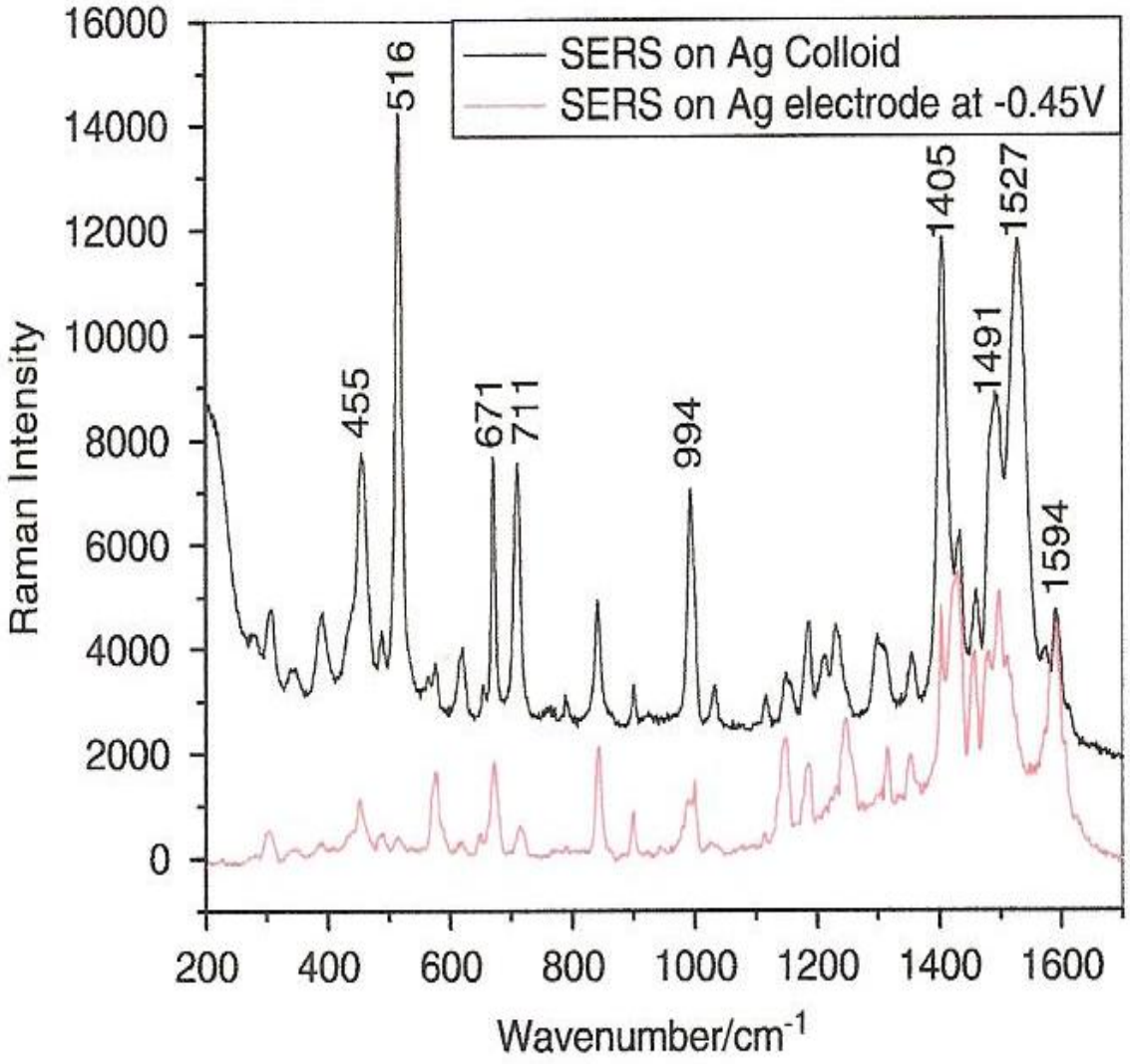

Figure 6.6. Comparison of SERS spectrum of 3-hydroxyflavone on a silver colloid with that on a silver electrode at -0.45 V.

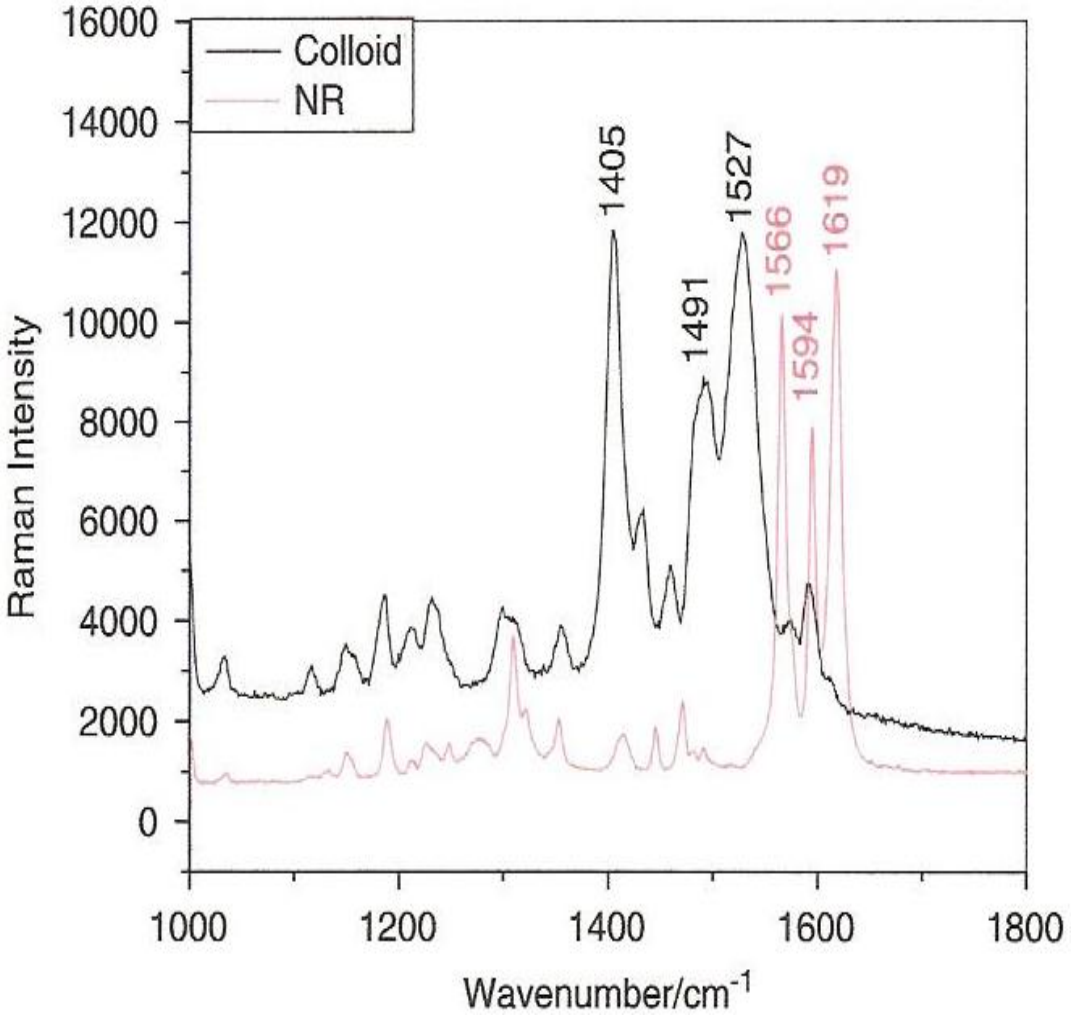

Figure 6.7. Comparison of the SERS spectrum of 3-hydroxyflavone with the normal Raman spectrum in the region 1000–1800 cm^{-1} .

6.3.3 5-Hydroxyflavone

Fig. 6.8 show the NR spectrum of the powder form of 5-HF, along with the results of the DFT calculation scaled by a factor of 0.97. For a complete summary of the observed and calculated lines, refer to Table 6.3. An excellent fit was observed with this scaling. The most intense lines at 1569, 1602, 1610 and 1650 cm^{-1} are assigned to the C=O, C_2 C_3 stretch and the Ring B quinoid stretch, as in flavone and 3-HF. Figure 6.9 displays a

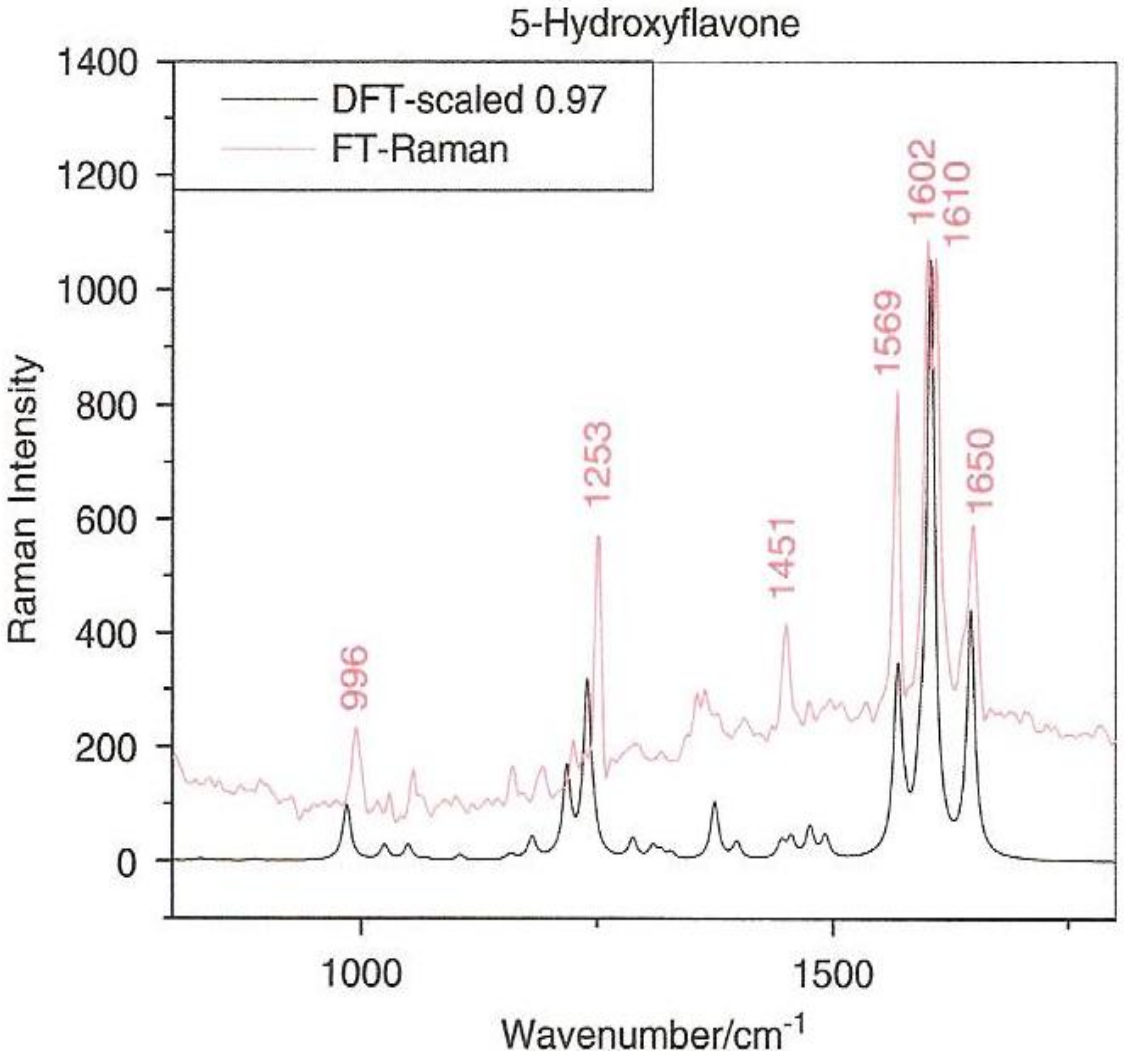

Figure 6.8. FT-Raman spectrum of 5-hydroxyflavone and comparison with density functional calculation in the region 800–1800 cm^{-1}.

comparison of the results on a silver electrode at -0.45 V with those on a colloid. For additional clarity, the DFT results are also included. As with flavone and 3-HF, the intensity of the lines near 1600 cm^{-1} are reduced relative to the other lines, especially those near 450–650 cm^{-1} (459 (υ_{16}), 524 (υ_{19}), 560 (υ_{20}), 619 (υ_{21}) and 659 (υ_{22}) cm^{-1}),

which rival all the other lines in the spectrum for intensity. These are some of the same modes that were strongly enhanced in 3-HF. In the NR and DFT, these lines are very

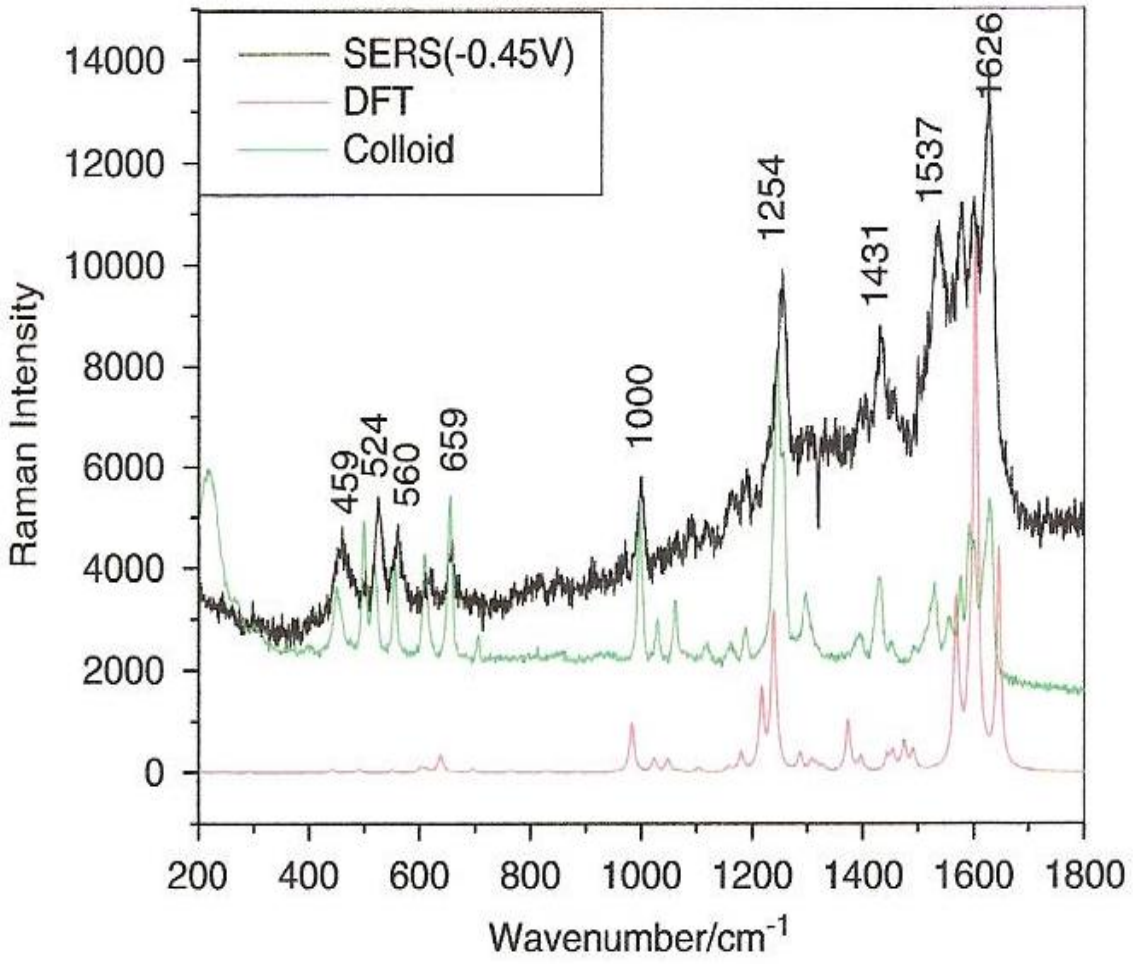

Figure 6.9. Comparison of SERS of 5-hydroxyflavone on electrode (top), colloid (middle) and DFT (bottom) in the region 200–1800 cm^{-1}.

weak. It is clear that proximity to the surface strongly affects both spectral regions but in opposite directions. The loss of intensity in the C=O stretching region indicates strong attachment of the molecule to the surface for the C=O and OH moieties, while the in-plane C–C deformations, farther from the surface, are clearly enhanced by the fact that their vibrational modes involve motions perpendicular to the surface.

Table 3. Wavenumbers (cm_1) and assignments of the Raman and SERS spectrum of 5-hydroxyflavone. The DFT wavenumbers are scaled by a factor of 0.97

Mode	DFT description of modes	Int	DFT (cm^{-1})	5-HF (cm^{-1})	5-HF (cm^{-1})	5-HF (cm^{-1})	5-HF (cm^{-1})
		Calc.	0.97	FT-NR	FT-IR	Colloid	SERS-0.45
6	Ring C. C-C deformation (oop)	-	-	224	-	-	-
7	Ring A, C-OH def (oop)	1	237	-	-	220	-
8	Ring A, B and C stretch (ip)	2	242	-	-	-	-
9	Rings A, B and C stretch (ip)	2	261	254	-	-	-
10	Rings A, B def; Ring C; O def (oop)	1	284	291	-	266	-
11	Ring C and B, C-O stretch	2	341	340	-	302	-
12	Ring A, O-H bending (oop); Ring C and B, C-C stretch	4	400	-	-	-	-
13	Ring A, O-H bending (oop)	4	402	-	-	-	-
14	Ring B, def (oop)	1	406	-	-	-	-
15	Ring A, B, and C. def (oop)	0	456	456	-	-	-
16	Ring C and B, C-C bending (ip)	2	477	-	-	451	459
17	Ring A and C, def (oop)	1	488	484	-	-	-
18	Ring A, B, C. C-C def	5	493	502	-	500	-
19	Ring A, B, C. C-C def	4	561	561	-	519	524
20	Ring A, B and C, C-C bending (ip)	16	598	618	-	555	560
21	Ring A and B, CH bending, Ring C deformation (ip)	1	599	-	615	611	619
22	Ring A, B, C, C-C def (ip)	21	629	-	-	-	-
23	Ring B, def (ip)	9	632	-	-	-	-
24	Ring A, B, C, C-C def	3	640	-	-	-	-
25	Ring A, B, C-H (oop) bend	3	654	651	650	657	659
26	Ring A, and C, C-H bending	2	695	708	675	707	-
27	Ring A, B, C-H (oop) bend	2	697	-	688	-	-
28	Ring A, B, C-H (oop) bend	0	751	-	754	-	-
29	Ring A, B, C-H (oop) bend	1	775	776	-	-	-
30	Ring A, B and C, C-H bending	1	783	-	-	-	-
31	Ring A, B, C, C-C def	3	800	-	802	814	814
32	Ring B, C_2', C_3', C_5', C_6': Ring C, C_3 bending (oop)	3	849	-	843	-	848
33	Ring A, C-H (oop) bend	1	861	-	-	-	-
34	Ring C, C_3-H bending (oop)	3	872	-	-	-	-
35	Ring A, B and C def (oop)	3	882	-	-	-	-
36	Ring B, C-H (oop) bend	2	936	-	900	-	-
37	Ring A, B and CC-C stretch	11	945	-	931	-	910
38	Ring A, C-H (oop) bend	0	964	-	-	-	-

39	Ring B, C-H bending (oop)	1	982	-	-	-	971
40	Ring B, def; Ring A and C, C-C stretch	96	999	997	997	998	1000
41	Ring B, C-H bending (oop)	1	1005	-	-	-	-
42	Ring A and B, C-C stretch (ip)	1	1021	-	-	-	-
43	Ring B, C-H (ip) bend	2	1034	1032	1032	1030	-
44	Ring A, C-C stretch (ip); Ring B and C, C-H bending (ip)	40	1061	1057	1057	1062	1065
45	Ring A, def; Ring B, C-C stretch (ip)	1	1083	-	1083		1091
46	Ring A, C-H (ip) bend	3	1108	-	1120	1121	1115
47	Ring A, C-C stretch (ip)	5	1164	1163	1157	1162	1163
48	C-OH stretch; Ring B, C-H (ip) bend	9	1179	-	-	-	-
49	Ring A, C-H, C-OH bending (ip)	3	1183	-	-	-	-
50	C-Oh stretch; Ring B, C-H (ip) bend	57	1194	1195	-	1189	1190
51	Ring A, B and C def (ip)	49	1209	1227	-	-	-
52	Ring A, B and C, C-H bending (ip)	365	1252	1253	1257	1255	1254
53	Ring A, C-H bending (ip)	21	1262	-	-	-	-
54	Ring A and B, C-H (ip) bend;	19	1277	-	-	-	-
55	Ring A and B, C-H (ip) bend;	11	1305	1291	1300	1298	1308
56	Ring A,B and C, def (ip); C-OH bending (ip)	5	1319	1318	1319	-	-
57	Ring A, B and C, C-C stretch	46	1334	-	-	-	1332
58	Ring A and B, C-H (ip) bend;	48	1349	1357	1365	-	-
59	Ring A, C-C stretch (ip)	25	1440	-	1417	1431	1431
60	Ring B, CH (ip) bend;	18	1452	1451	1452	1453	1458
61	Ring A, CH (ip) bend	7	1478	1475	1475	-	-
62	Ring B, CH (ip) bend	17	1497	1498	-	1494	1499
63	Ring A, B, and C, C-C and C_4-O stretch (ip)	56	1557	-	-	1557	1579
64	Ring A, quinoid stretch; C=O stretch	66	1568	1569	-	1577	1579
65	C=O stretch; in-phase-C_2=C_3 stretch	37	1580	-	1589	-	-
66	Ring B, quinoid stretch	500	1603	1602	-	1593	-
67	Ring A, B, and C, C-C and C_4-O stretch (ip)	69	1613	1610	1622	1600	1600
68	C=O stretch; out-of-phase-C_2=C_3 stretch	105	1646	1650	1657	1629	1626
69	Ring A, C_6, C_7-H stretch (ip)	120	3069	3062	3060	-	-
70	Ring A and B, CH stretch	47	3073	3062	3060	-	-
71	Ring A and B, CH stretch	132	3083	3062	3060	-	-
72	Ring A and B, CH stretch	108	3095	3062	3060	-	-
73	Ring A and B, CH stretch	154	3096	3062	3060	-	-
74	Ring B, C-H stretch (ip)	193	3106	3062	3060	-	-

75	Ring B, CH stretch	118	3124	3062	3060	-	-
76	Ring B, CH stretch (ip)	80	3125	3062	3060	-	-
77	Ring C, C_3-H stretch (ip)	-	-	-	-	-	-
78	O-H stretch (ip)	248	3566	-		-	-

ip: in-plane; oop: out-of-plane

6.3.4 Quercetin

The FT-Raman spectrum of solid quercetin is displayed in Figs 6.10 (200–1000 cm^{-1}) and 11 (1000–2000 cm^{-1}) along with the results of the DFT calculations. In the low wavenumber region, it was unnecessary to apply a scaling factor to the DFT results in order to obtain a good fit. In the higher wavenumber section of the spectrum, it was found necessary to multiply the raw DFT wavenumbers by a factor of 0.97 in order to properly fit the observed spectrum. Such piecewise scaling of the DFT results has been found necessary in numerous previous studies[187-189] . The observed wavenumbers and their corresponding assignments are listed in Table 6.4. The assignments were readily obtained owing to the excellent matching of the DFT calculations with the observed spectrum. Also include is the table results of Cornard *et al.*[176], who first obtained the FT-Raman and IR spectra of quercetin both in solid and solution. They used a single point Hartree-Fock SCF calculation as aid in the assignments. A good correlation was observed in this experiment when compared with their results. However, these result presents the additional information of normal mode assignments based on more accurate and optimized DFT calculations, several of which disagree with the earlier results. In the low wavenumber region (Fig. 6. 10), each of the intense lines corresponds somewhat closely to a calculated feature, and the assignment is clear for these lines. In order to obtain a good fit in the region above 1000 cm^{-1}, as mentioned above, it was necessary to scale the DFT results by a factor of 0.97. Once again, in this case an excellent fit is obtained. The

most intense region of the spectrum is around 1600 cm^{-1}, which usually involves the C=O stretching modes among others. At still higher wavenumbers (3000 cm^{-1}), only a single line is observed at 3081 cm^{-1},which is the C–H stretching region (predicted to be between 3058 and 3158 cm^{-1} (scaled) in the DFT). This line is set atop a broad featureless band. Despite the DFT predictions of various *O*–H stretching bands between 3283 and 3675 cm^{-1}, none was observed in the spectrum, possibly owing to interactions with adjacent molecules in the crystal.

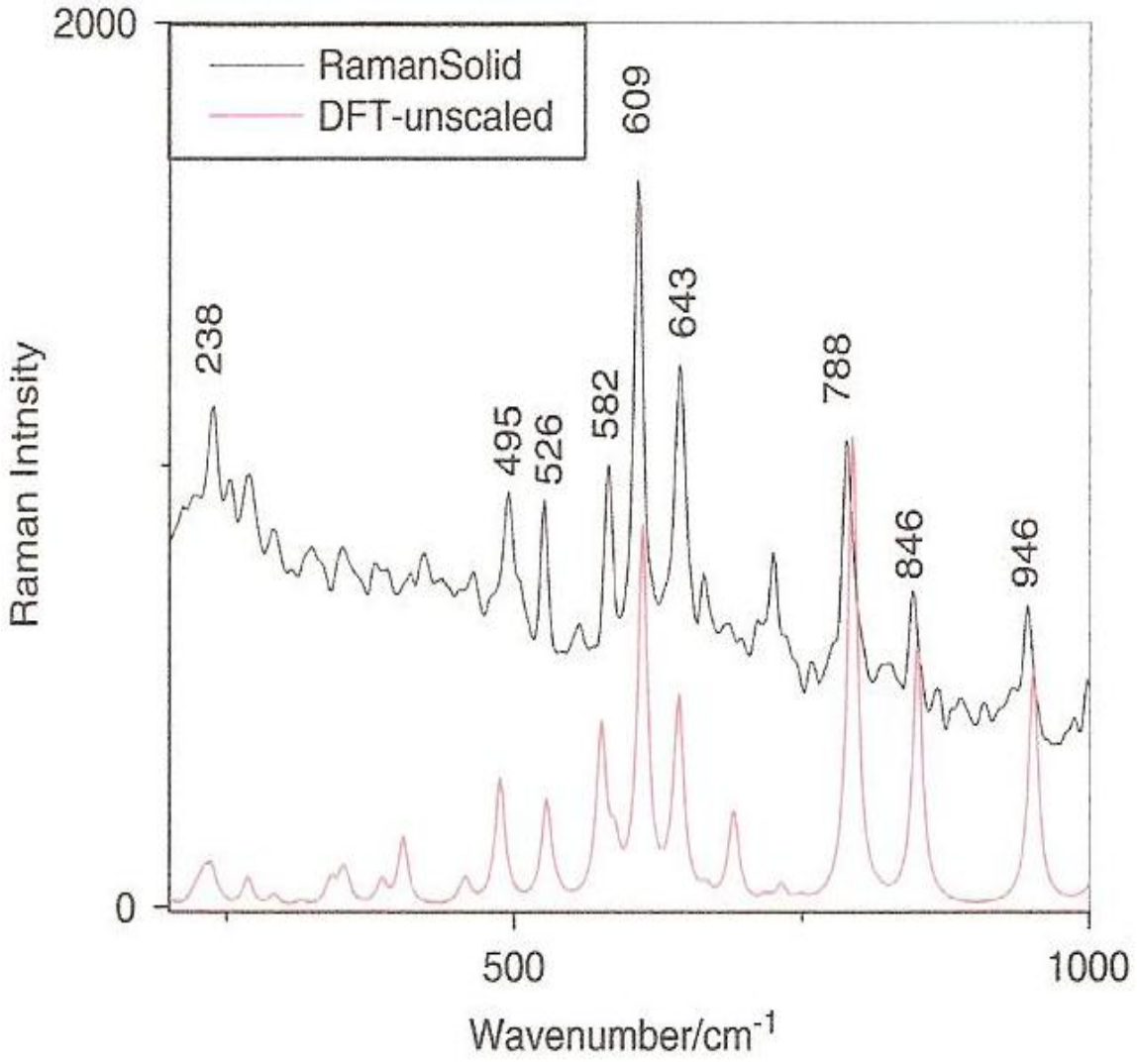

Figure 6.10. FT-Raman spectrum (200–1000 cm^{-1}) of solid quercitin compared with DFT calculated spectrum (unscaled).

Table 6.4. Wavenumbers (in cm^{-1}) and assignments of the Raman and SERS spectrum of quercitin. DFT calculations are scaled by 0.97 unless marked by 'u' for unscaled.

Mode no.	DFT	Description	Raman Solid[a] (cm^{-1})	Raman Solution[a] (cm^{-1})	FT-Raman Solid[b] (cm^{-1})	FT-Raman Colloid[b] (cm^{-1})	SERS – 0.50 V[b] (cm^{-1})
21	404u	Rings A, C ip rock; $C_{5,7}$ OH bend	-	-	-	420	433
24	460u	Rings A, C ip rock; $C_{3,7}$ OH bend	-	-	-	460	452
25	488u	Ring B, CC ip rock, $C_{3',4'}$ OH bend	-	-	495	481	-
26	528u	Ring A, CC ip def	-	-	526	-	521
28	576u	Ring A, B, CC ip def	-	-	582	586	582
32	612u	Ring A, B, C ip CC def	604	601	609	605	608
34	643u	Ring A, B ip CC def	640	638	643	636	-
35	667u	Ring A, B, C oop CC, CH bend	661	666	665	-	662
36	689u	Ring A, B, C oop CC, CH bend	686	687	-	-	676
38	719u	Ring A, B ip CC def	721	-	724	722	711
42	794u	Ring B, ip C=C str	785	789	788	772	-
46	851u	Rings A, B, C ip CC str	843	845	846	846	845
49	952u	Rings A, B, C ip CC str	942	938	946	954	-
50	1013u	CH ip bend, C-O-C bend	1013	-	998	-	1002
53	1130u	3,3',4' O-H, CH blend	-	-	1116	1100	1115
54	1139u	CH, OH, ip bend	-	-	1139	-	1149
55	1179u	C_7OH, C_8H ip bend	1175	1170	1178	1199	1186
59	1219u	CH ip bend	1216	1209	1222	-	-
60	1263u	CH, OH ip bend	-	-	1266	1255	1253
61	1266u	CH, OH ip bend	1268	1267	-	-	-
64	1310	3,5,3' OH ip bend	1315	1321	-	-	1319
66	1321	3 OH bend	1328	1333	1332	1338	1338
67	1343	4' PJ bend, CH ip bend	1357	1346	-	-	1355
68	1362	3,5,7 OH ip bend	1371	1376	1372	-	-
69	1386	3,5,7 OH ip bend	1398	1402	1403	1401	1406
70	1414	OH, CH ip bend, Rings A, B, C CC	1410	1419	-	-	-
71	1432	3,5,7 OH bend, Ring A, CC, B C=C	-	1431	-	-	1433
72	1466	3,5 OH, CH ip bend, C=O	1440	1447	1444	-	-
73	1489	3,5,7 OH ip bend $C_{6,8}$ H ip	1463	1464	-	1459	1461

		bend					
74	1517	Ring B, CH ip bend	1531	1501	-	1500	1500
75	1551	C=O str, 5 OH bend, Ring B CC str	1548	1569	1544	-	-
76	1585	C=O str, OH ip bend, Ring A B CC	1596	1577	1588	1594	1598
78	1599	C=O, C_2 =C_3 str, 3,5 OH bend	1604	1613	1604	-	-
79	1617	C_2 =C_3 str, 3,5 OH bend	1609	1627	-	-	-
80	1638	5 OH bend, Ring A quinoid str	1662	1656	1660	1644	-
81	3058	C5’ – H str	-	-	3042	-	3042
82	3084	C4 – H str	-	-	3081	-	3072
83	3094	C2’ – H str	-	-	3114	-	-
84	3123	C8 – H str	-	-	-	-	-
85	3158	C6’ – H str	-	-	-	-	-
86	3283	5 OH str	-	-	-	-	-
87	3475	3 OH str	-	-	-	-	-
88	3670	3’,4’ OH str (asym)	-	-	-	-	3699
89	3671	7 OH str	-	-	-	-	3714
90	3675	3’,4’ OH str (sym)	-	-	-	-	3784

ip: in-plane; oop: out-of-plane;
[b] This work.

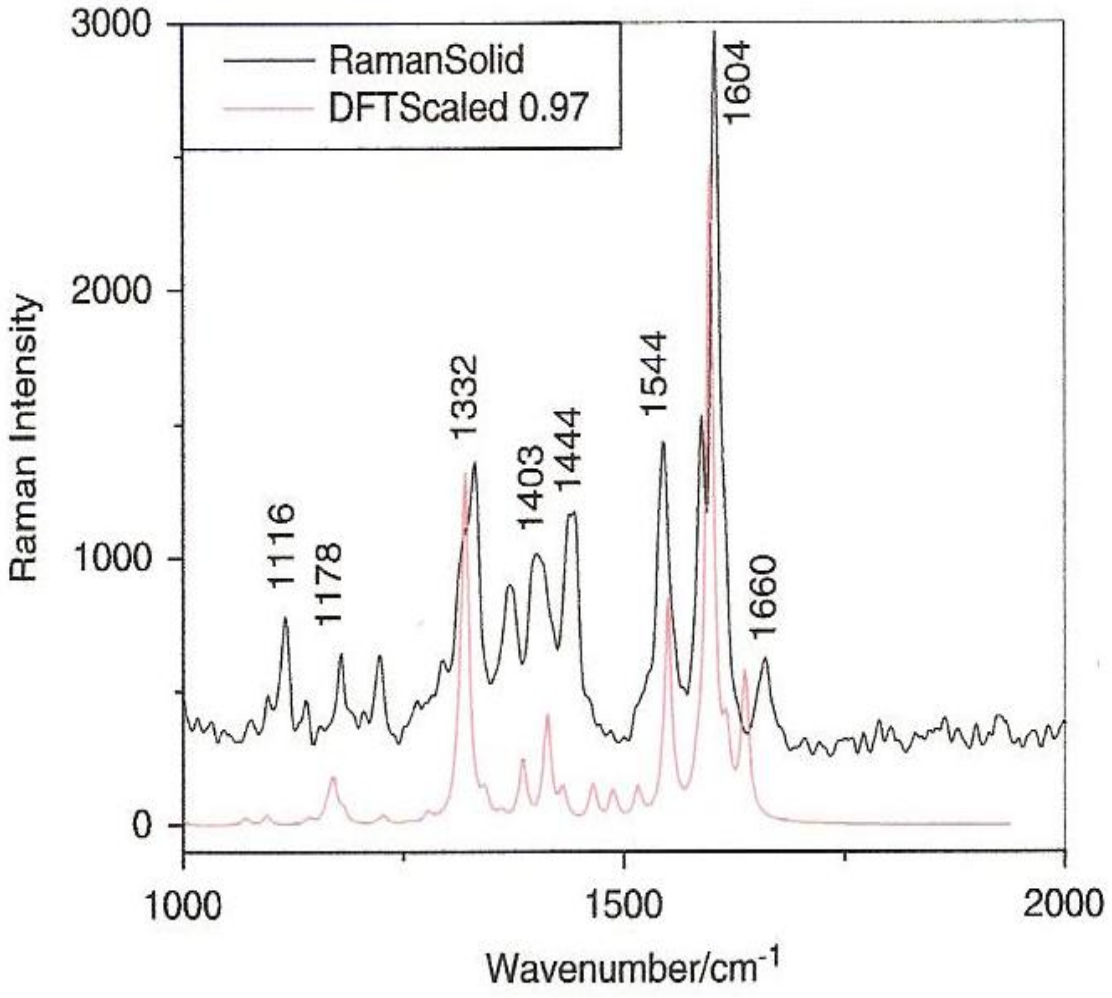

Figure 6.11. FT-Raman spectrum (1000–2000 cm^{-1}) of solid quercitin (upper) compared with DFT calculated spectrum (lower) with wavenumbers scaled by 0.97.

The most intense line in the FT-Raman spectrum of the solid is that at 1604 cm^{-1}, which is assigned to the υ_{78} mode (1599 cm^{-1} in the calculation). This may be described as mainly a combination of the C=O stretch, C_2 C_3 stretch and in-plane 3 and 5 *O*–H bends. The nearby υ_{75} (at 1544 cm^{-1}) is somewhat weaker and is assigned as the C O stretch, the 5 *O*–H (in-plane) bend and the Ring B, C=C deformation. The υ_{80} mode (at 1660 cm^{-1}) involves the 5 *O*–H bend and the Ring A, quinoid stretch. This region closely resembles that of the most intense lines in the corresponding spectrum of flavone and its

3- and 5-hydroxy derivatives discussed above. In those spectra, the most intense lines also tend to involve the C=O stretch. By examining the assignments of quercetin, it is clear that the in-plane *O*–H bends are responsible for a plurality of the observed spectral lines. Part of this is clearly just due to the fact that there are five hydroxy substituents, and these would be expected to have a noticeable effect on the spectrum.

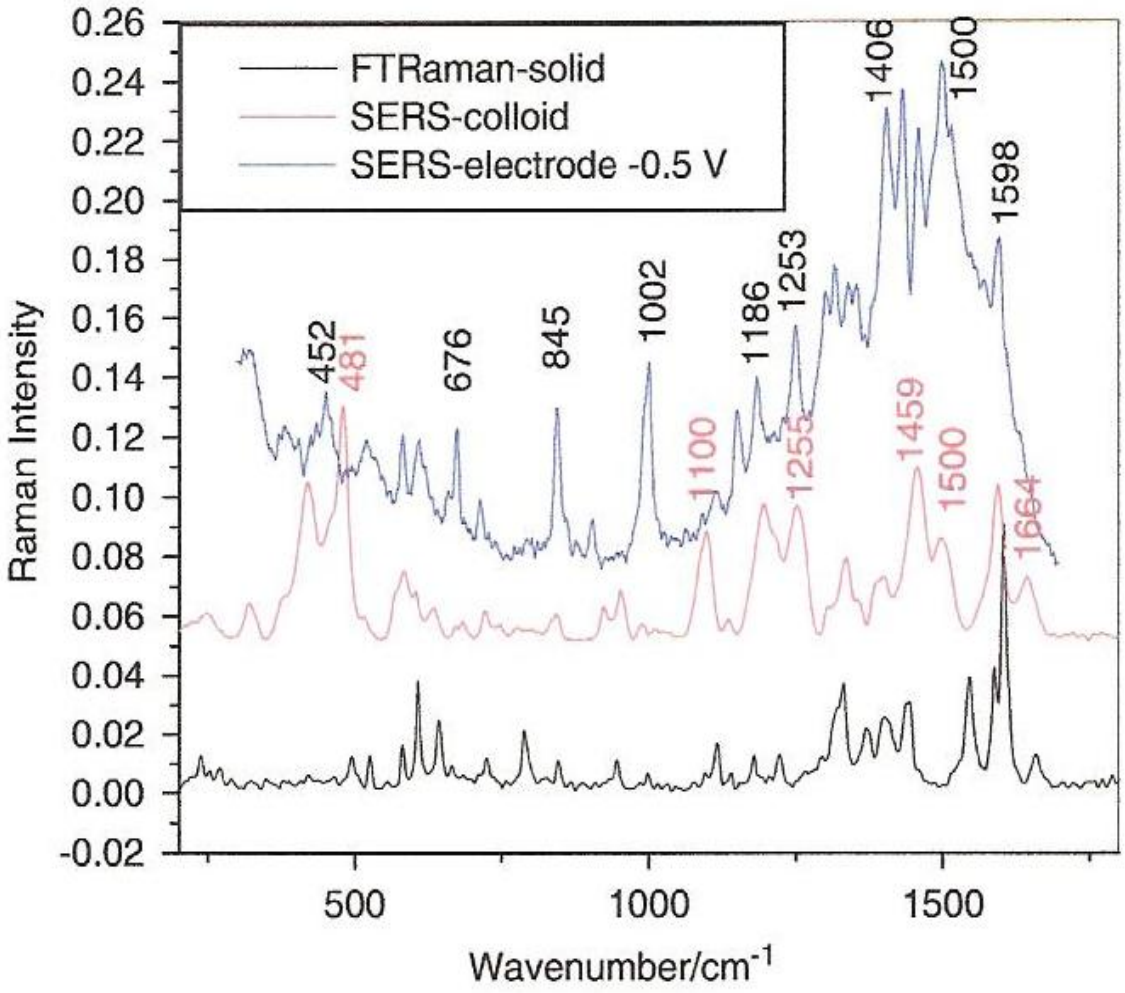

Figure 6.12. FT-Raman spectra of quercitin in solid (lower) on Ag colloid surface (middle) and on Ag electrode at -0.50 V (upper).

Fig. 6.12 shows a comparison of the spectrum of solid quercetin with that of the molecules adsorbed on a silver colloid and on an Ag electrode at -0.50 V. The measured wavenumbers are listed in Table 6.4. Note that the wavenumbers of a majority of the lines are the same, while the intensities of many lines are changed by proximity to the metal surface, as is common in SERS. Especially noteworthy is the observation of the shift of the 1660 cm^{-1} line (υ_{80}) to 1644 cm^{-1} in the colloid, with little loss of relative intensity. The rather large shift indicates that this is a likely site for adsorption to the surface. On the electrode this line is not noticed, or is perhaps hidden in the rather large shoulder that is commonly observed on Ag electrodes in this region. The line at 1544 cm^{-1} (υ_{75}), also involving the C=O stretch, disappears, possibly for the same reason. On the other hand, the band at 1588 cm^{-1} (υ_{76}) is only slightly shifted to 1594 cm^{-1} on the colloid and 1598 cm^{-1} on the electrode, also with little loss in intensity. Note also that several lines involving various in-plane OH and CH bends (such as 1100 (υ_{53}), 1199 (υ_{55}), 1255 (υ_{60}) and 1338 (υ_{66}) are strongly enhanced on the colloid surface. On the electrode, still other lines are strongly enhanced (i.e. at 1002 (υ_{50}), 845 (υ_{46}), 676 (υ_{36}) and 452 (υ_{24}) cm^{-1}).

Note, however, that the most intense lines, i.e. those at 420, 460, 481, 1459 and 1500 cm^{-1}, in the SERS spectrum on the colloid are strongly enhanced compared to those in the NR spectrum. These lines are also predicted to be weak by the DFT calculations. The lowest three are assigned to in-plane ring deformations, but with a strong component of C–OH in-plane bending. For example, the line at 420 cm^{-1} (υ_{21}) has a strong C_5OH and C_7OH bend, while the line at 481 cm^{-1} (υ_{25}) has strong contributions from $C_{30}OH$ and $C_{50}OH$ bends. The line at 1459 cm^{-1} (υ_{73}) involves 3, 5 and 7 OH in-plane bends, while

that at 1500 cm^{-1} (υ_{74}) is composed of Ring B in-plane CH bends. The strongly enhanced intensity of these lines is clearly a result of interaction with the surface. However, the most strongly enhanced lines on the Ag electrode mainly involve in-plane ring stretches..

Flavone (cm^{-1})	3-HF(cm^{-1})	5-HF(cm^{-1})	Mode description
1570 υ_{61}	1566 υ_{63}	1569 υ_{64}	Ring A ip def, C=O stretch
1603 υ_{63}	1594 υ_{64}	1602 υ_{66}	Ring B quinoid stretch
1621 υ_{64}	1627 υ_{66}	1610 υ_{67}	Rings A, B, C deformation (ip)
1634 υ_{65}	1619 υ_{65}	1650 υ_{68}	C=O, C_2 C_3 stretch

ip: in-plane.

Table 6.5 Comparison of C O stretching region for flavone, 3-hydroxyflavone and 5-hydroxyflavone (Fig.5.13).

3-HF (cm^{-1})	Mode no.	5-HF (cm^{-1})	Mode no.	Description (DFT)
711	27	707	26	Ring B, C def, CH ip bend
671	24	757	23	Ring A, B def
620	21	611	21	Ring C, def
575	19	555	20	Ring A, B, and/or C def
516	17	519	19	Ring A, B, and/or C, def
488	16	500	18	Ring A, and/or C, def
455	15	451	16	Ring A, B, and/or C def

ip: in-plane

Table 6.6. Modes of 3- and 5-hydroxyflavone, which are strongly enhanced on the colloid surface (Fig.5.15)

It is possible that the potential on the colloid is quite different from that on the electrode. We also note that the colloid has a coat of citrate remaining. These may account for the differences, and a study of the complete potential dependence of the SERS would be in order. Furthermore, we cannot rule out the possibility of a photoproduct. For example, Sanchez-Cortes *et al*[190]., in studies of diphenols on Ag colloids, found several new Raman bands, which they attributed to production of dimers through formation of C–C and either C–*O*–C bonds between pairs of diphenols. However, further investigations are most likely needed to establish the detailed reasons for the spectral observations.

6.3.5 Comparison of normal wavenumbers

It is worthwhile to compare the effects of successive OH substitution on the observed wavenumbers of flavone. However, a complete comparison of all modes for all the molecules examined here would be a lengthy and complex exercise. Instead, The focus will be on a few regions of the spectrum, which might be of special interest. First, it shpuld be noted that the *O*–H stretching region would be of considerable interest, if it were observed experimentally. For 3-HF a line is predicted at 3420 cm^{-1} by DFT, while the 5-HF counterpart is indicated at 3566 cm^{-1}. In quercetin, there are five predicted wavenumbers between 3283 and 3675 cm^{-1}. All are predicted to have sufficient intensity to be observed in NR spectroscopy, but none are found. It is possible that molecule–molecule interactions in the solid either suppress or broaden these bands, making them invisible. They are not observed in our experiments in solution, or on Ag surfaces either.

Also of considerable interest are the most intense lines near 1600 cm^{-1}, which are usually termed the carbonyl stretching region. In Fig. 6.13 comparison of the normal FT

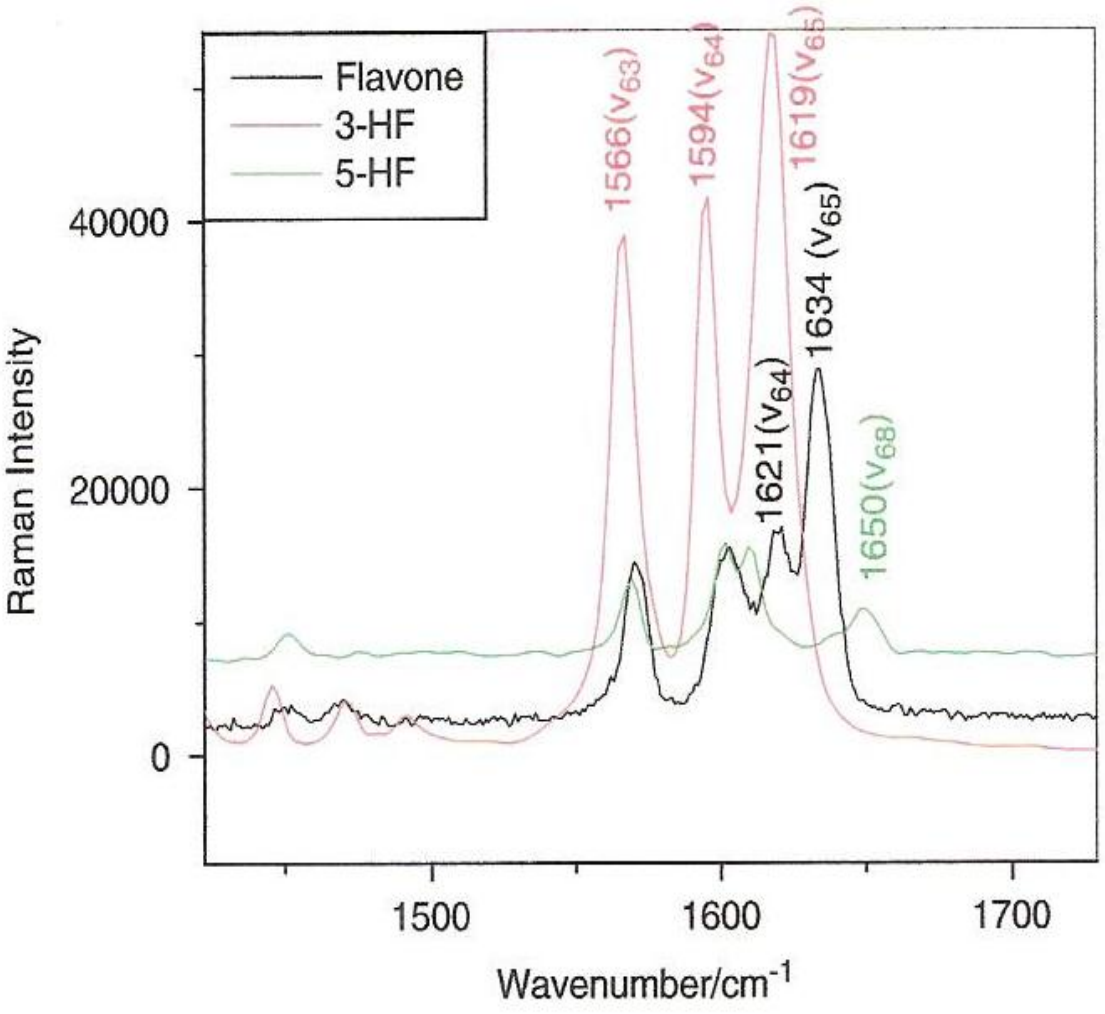

Figure 6.13. Comparison FT-Raman spectra in the C=O stretching region (1400–1800 cm^{-1}) of flavone, 3-hydroxyflavone and 5-hydroxyflavone powder.

Raman spectra of flavone, 3-HF and 5-HF powder are shown. The spectra of all the species consist of three or four intense lines and appear quite similar. However, the density functional calculation enables the comparison of like vibrational modes, in a way not accessible just by observation of the spectrum. Table 6.5 summarize the observed wavenumbers, and their spectral assignments obtained from application of DFT. The

lowest line in this region in each spectrum (1570, 1566, and 1569 cm^{-1}, respectively) maybe assigned to the simultaneous Ring A, in-plane deformation, coupled to C=O stretch. Consequently, there is almost no shift of this line from flavone on OH substitution. However, the line at 1603 cm^{-1} in flavone is nearly unchanged in 5-HF, but drops slightly to 1594 cm^{-1} in the 3-hydroxy substituent. This vibration consists mainly of the Ring B quinoid-like C=C stretch, and is therefore also likely to have only a slight variation with substitution. The series starting at 1621 cm^{-1} in flavone is assigned to the in-plane deformation of all three rings (A, B and C), and is strongly influenced by substitution. Note the υ_{66} mode in 3-HF is not observed in the spectrum, and therefore it is substituted by the calculated (scaled) wavenumber in parentheses. The most strongly perturbed line is the 1634 cm^{-1} flavone line attributed to C=O and C_2 C_3 stretching. This drops to 1619 cm^{-1} in 3-HF (below the ring deformation (υ_{66}) but increases up to 1650 cm^{-1} in the 5-hydroxy derivative. The drop on 3-hydroxy substitution is caused by attachment of the —OH to the C_3 atom, which is an important part of the unperturbed vibration in flavone, while attachment of the —OH to the C_5 position has the opposite effect, adding a strong component of —OH bending to the normal mode. As mentioned in the previous section, all of these modes are considerably weakened in intensity on attachment to a silver surface, relative to several lower lying vibrations.

It is difficult to compare the spectrum of quercetin with all the other molecules owing to the fact that the normal modes of quercetin are dominated by the large number of OH bending modes. Despite this difficulty, the spectrum of quercetin resembles those of the other molecules. Fig. 6.14, shows a comparison of the spectrum of quercetin with that of 5-HF in the region 1200–1800 cm^{-1}. This is the region that most closely resembles

that of quercetin. From the strong resemblance we may infer that the modes υ_{75}, υ_{76}, υ_{78} and υ_{80} of quercetin may be associated with υ_{64}, υ_{66}, υ_{67} and υ_{68}, respectively, of 5-HF.

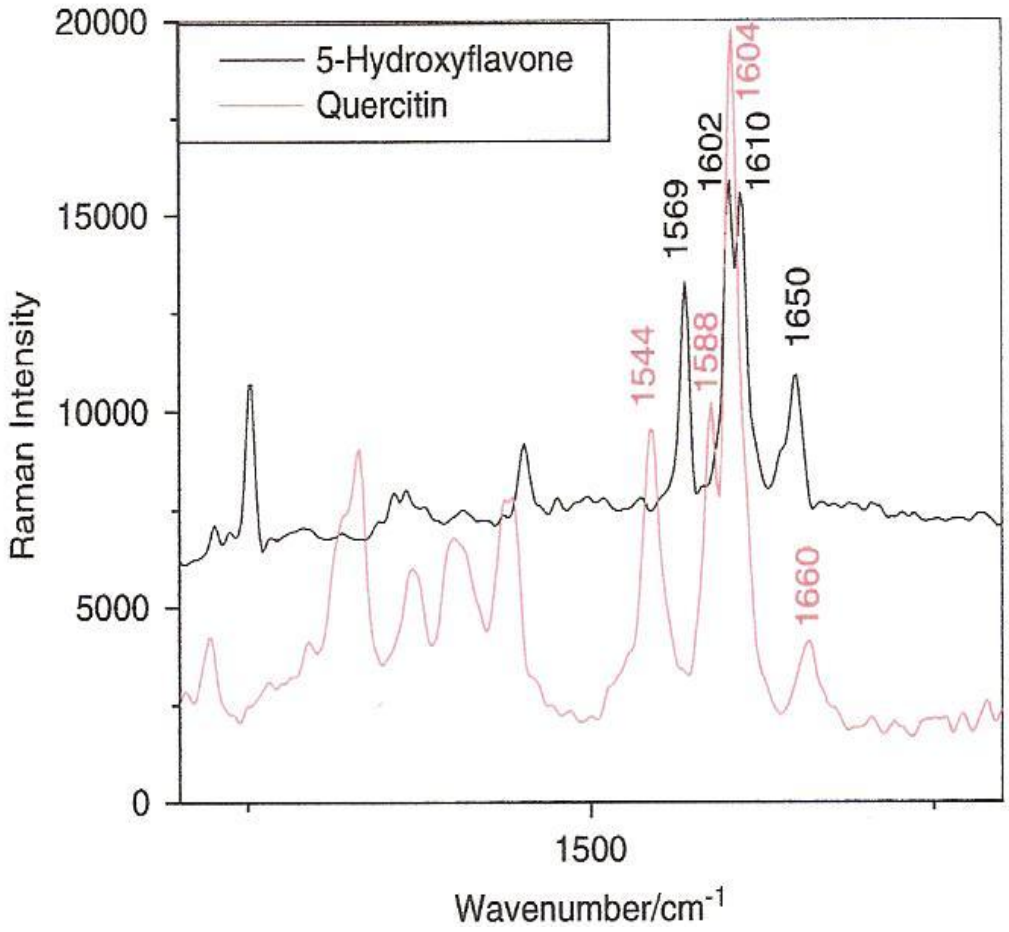

Figure 6.14. Comparison of the FT-Raman spectrum of solid 5-hydroxyflavone and quercitin in the region 1200–1800 cm^{-1}.

Several of the modes observed in 3- and 5-HF are quite strongly enhanced on the colloid or silver surface. Fig. 6.15, shows a comparison of these modes, which appear in the region of 200–800 cm^{-1}. The observed increase in intensity of these modes converts them from some of the weakest bands in the solid to dominant bands on the colloid. The measured wavenumbers and assignments are listed in Table 6.6. It can be noticed that these lines are predominantly the ring C–C in-plane deformations. This indicates that the

molecules are by and large (or at least have a large component) perpendicular to the metal surface. This is consistent with the simultaneous decrease in intensity of the higher frequency modes representing the C=O and C_2 C_3 stretch.

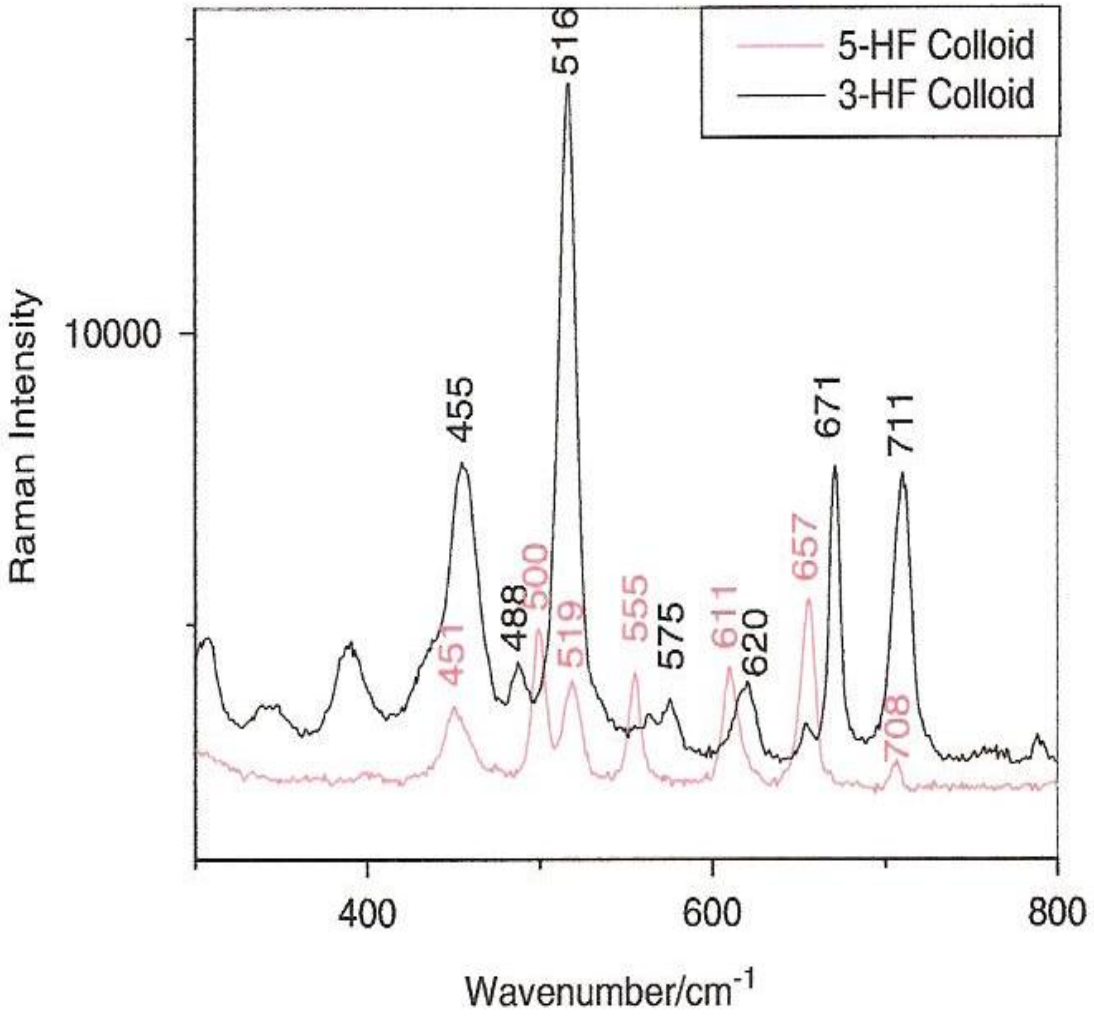

Figure 6.15. Modes of 3- and 5-hydroxy flavone, which are strongly enhanced on the colloid surface. The 200–800 cm^{-1} region is shown.

6.4 Persian berries – A case study of possible application of SERS in art

In order to demonstrate the potential of SERS as an ultrasensitive analytical tool in the identification of natural flavonoid dyes in works of art, a microscopic sample from a modern silk fabric dyed using a Persian berries extract in the Department of Textile Conservation at The Metropolitan Museum of Art was examined. Persian berries is the name for a yellow dye obtained since antiquity from the dried unripe berries of plants in the buckthorn family (*Rhamnus*)[159]. Previous work done by our group on a variety of natural dyes[191,192] has shown that microscopic textile samples can be analyzed by SERS following a vapor phase treatment with hydrofluoric acid (HF) to hydrolyze the mordant dye complex. In this case, a 2 mm fragment of a silk thread from a modern textile dyed with Persian berries following traditional practice was treated for 15 min in a micro chamber saturated with HF vapor. Following HF treatment, the sample was treated with a 2 μl drop of Ag colloid (diluted 20d) and 2 μl of a 0.2 M KNO_3 solution and the SERS spectrum measured directly from the microscopic colloidal aggregates deposited on the fiber. The spectrum obtained from the micro sample (Fig. 6.16) using 10 mW of 785 nm laser excitation clearly shows some of the quercetin bands, although the dye sample lines are somewhat broader and poorly resolved compared to our reference spectra. Note especially the prominent 1592 cm^{-1} band (υ_{76}) and the nearby shoulder at 1641 cm^{-1}. Furthermore, the intense line in the colloid spectrum of quercetin at 481 cm^{-1}shows up considerably weaker in the fabric microsample. The other bands present are probably due to other flavonoids such as rhamnetin and kaempferol, also contained in Persian berries. It should be noted that although high-quality SERS spectra of the pure dyes have been

obtained for all flavonoids, the current results show that further work on the treatment protocol for actual textile samples is needed in order to develop SERS into a routine technique for dye analysis. Nonetheless, the results shown here and the success we had with the same technique in the case of other natural dyes such as alizarin and berberine and some synthetic dyes[193] suggest that SERS has an enormous potential for analytical applications in which sampling is restricted to microscopic amounts.

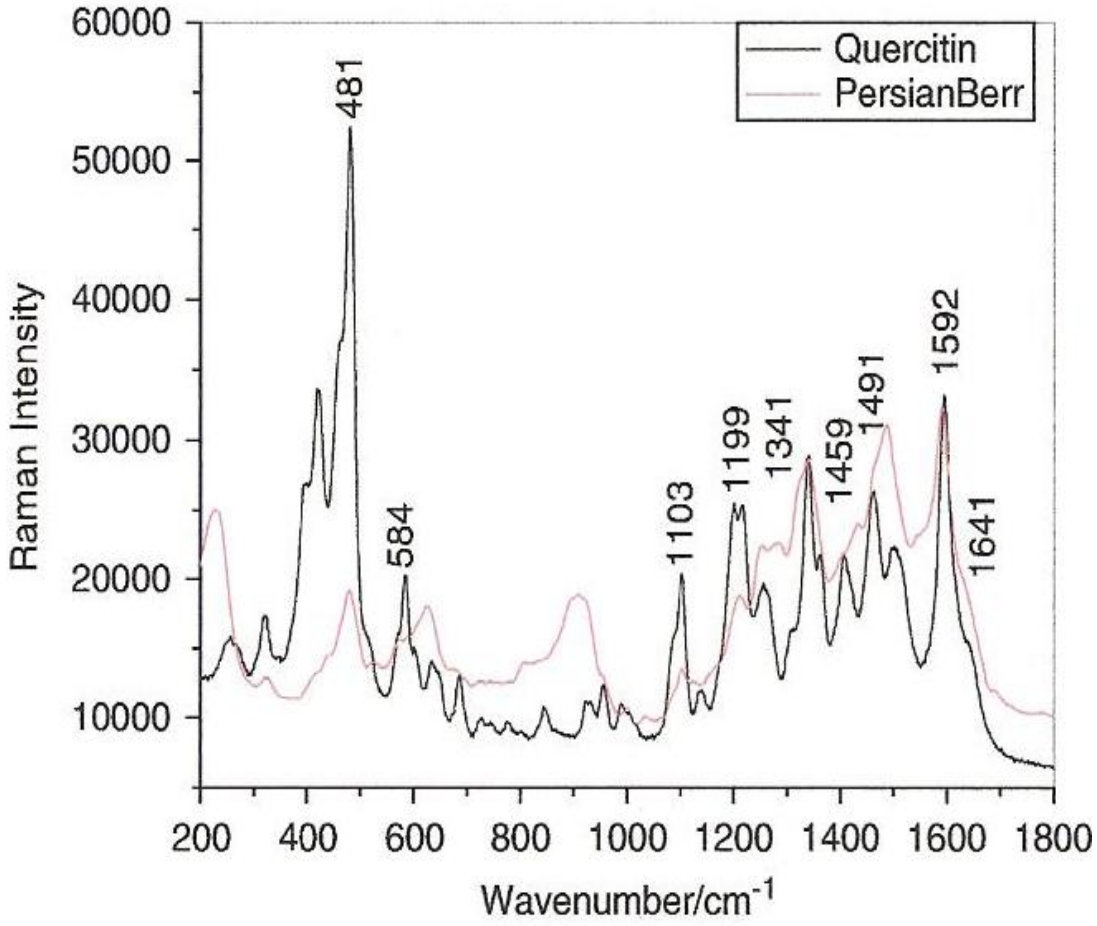

Figure 6.16. A comparison of the spectrum of quercitin on Ag colloid with that of the dye Persian berries, also on colloid. Spectra were obtained using 10 mW of the 785 nm excitation wavelength.

6.5 Conclusions

The Raman spectra of flavone and several hydroxy derivatives in powder form, as well as on Ag colloid, and where possible on Ag electrodes were obtained. The latter are enhanced by the technique of SERS, and produced intense spectra from a small quantity of material while simultaneously suppressing fluorescence. Comparison to the relative intensities from the NR spectra with both colloidal and potential-dependent SERS and with DFT calculations were made. It is concluded that DFT calculations provide a source of accurate normal mode assignments, as well as a basis of comparison of the effects of successive OH substitutions on the normal modes of the parent flavone. A more detailed understanding of these environments should answer questions such as why the normal modes with C–*O*–H bending components are suppressed in the SERS spectra of the substituted flavones. Finally, a case study in the application of this technique to the identification of the active ingredient of a dye extracted from a textile in art was provided and yielded promising results.

Chapter 1 References

[1] Arakawa, Y.; Sakaki ,H.; *Appl. Phys. Lett.* **40**, 939 **(1982).**

[2] Ekimov, A. I.; and Onushchenko, A.A.; *JETP Lett.* 34, 345 **(1981).**

[3] Rossetti, R., Nakahara, S. & Brus, L.E J. Chem. Phys. **79**, 1086 **(1983).**

[4] Karreich, E.; *Nature* **413**, 450 (2001).

[5] Xin, S.H.; Wang, P.D.; Yin, A.; Kim, C.; Dobrowolska M.; Merz, J.L.; Furdyna, J.K.; *Appl. Phys. Lett.* **69**, 3884 (1996).

[6] *Control of Microstructural and Optical Properties in Self-Assembled Quantum Dots Grown By Molecular Beam Epitaxy;* Perez -Paz, N.M.; Dissertation Thesis, Chemistry Dept. City University of New York, **2005**

[7] Sohel, M.; Muñoz, M.; and Tamargo, M. C.; *Appl. Phys. Lett.* 85, 2794 **(2004).**

[8] *Perspectives on the Physical Chemistry of Nanocrystals;* Alivisatos, A.P., *J.Phys.Chem.*, **1996,** 100, 13226.

[9] *A single-electron transistor made from a cadmium selenide nanocrystal*; Klein, D.L.;Roth, R.; Lim, A.K.L.; Alivisatos, A.P.; McEuen, P.L., *Nature*, **1997**, 389, 699.

[10] *Light-emitting diodes made from cadmium selenide nanocrystals and a semiconducting polymer;* Colvin, V.L.; Schlamp, M.C.; Alivisatos, A.P., *Nature*, **1994**, 370, 354.

[11] Cao, C.; Jin, R.; Mirkin, C.A., *Science*, 2002, 297, 1536-1762.

[12] Du, H.; Disney, M.D.; Miller, B.L.; Krauss, T.D., *J.Am.Chem.Soc*., 2003, 125, 4012-4013.

[13] *Surface Enhanced Raman Scattering* ; Chang, R.K.; Furtak, T.E.,(Plenum, New York, 1982).

[14]*Surface Enhanced Raman Scattering*; Van Duyne, R.P., *Chemical and Biochemical Applications of Lasers*, edited by C. B. Moore, (Academic Press, New York, 1979), Vol. 4, p.101.

[15] *Surface Enhanced Spectroscopy;* Moskovits, M., *Rev. Mod. Phys***. 1985**, 57**,** 783.

[16] *Surface Enhanced Raman Scattering*; Birke, R.L.; Lombardi, J.R., in *Spectroelectrochemistry: Theory and Practice* Ed. R.J. Gale, Plenum,**1988**.

[17] Merz, J.L.; Lee, S.; Furdyna, J.K.; *J. of Crystal Growth* 184/185, **1998**, 228-236

Chapter 2 References

[18] The Physics and Chemistry of Materials; Gersten, J.I.; and Smith, F.W.; New York: John Wiley & Sons, Inc, pp. 382-387, **2001**

[19] Control of Microstructural and Optical Properties in Self-Assembled Quantum Dots Grown By Molecular Beam Epitaxy; Perez -Paz, N.M.; Dissertation Thesis, Chemistry Dept. City University of New York, **2005**

[20] Vilarrubia, J. S.; J. Res. Natl. Inst, Stand. Technol. **102**, 425 **(1997).**

[21]M. Fleischmann, P. J. Hendra, and A. J. McQuillan, Chem. Phys. Lett. 26, 163 **_1974**

[22] E. Burstein, Y. J. Chen, S. Lundquist, and E. Tosatti, Solid State Commun. **21**, 567, 197**9**

[23] B. N. J. Perrson, Chem. Phys. Lett. 82, 561 **(1981).**

[24] J. I. Gersten, R. L. Birke, and J. R. Lombardi, Phys. Rev. Lett. **43**, 147, **(1979)**

[25] T. Maniv and H. Metiu, Chem. Phys. Lett. **79**, 79**, (1981)_.**

[26] J. E. Demuth and N. Sanda, Phys. Rev. Lett. **47**, 57 (1981)

[27] S. Centeno, I. Lopez-Tocon, J. F. Arenas, J. Soto, and J. C. Otero, J. Phys.Chem. B **110**, 14916,_**2006**

[28] A. C. Albrecht, J. Chem. Phys. **34**, 1476, (**1961)_.**

[29] J. R. Lombardi, R. L. Birke, T. Lu, and J. Xu, J. Chem. Phys. **84**, 4174, **(1986)_.**

[30] S. Nie and S. R. Emory, Science **275**, 1102, **(1997**)_.

[31] K. Kneipp, Y. Wang, H. Kneipp, L. Perelman, I. Itzkan, R. R. Dasari, and M. S. Feld, Phys. Rev. Lett. **78**, 1667 **(1997)**

[32] H. Xu, E. Bjerneld, M. Käll, and L. Börjesson, Phys. Rev. Lett. **83**, 4357, **(1999)**

[33]W. E. Doering and S. Nie, J. Phys. Chem. B **106**, 311 **(2002)**

[34]Y. Sharaabi, T. Shegai, and G. Haran, Chem. Phys. **318**, 44 **(2005)_.**

[35]T. L. Haslet, L. Tay, and M. Moslrovits, J. Chem. Phys. **113**, 1641, **(2000).**

[36] A. M. Michaels, M. Nirmal, and L. E. Brus, J. Am. Chem. Soc. **121**, 9932, **(1999)**

[38] A. G. Brolo, A. C. Sanderson, and A. P. Smith, Phys. Rev. B **69**, 045424, **(2004)**

[39]P. Hildebrandt and M. Stockburger, J. Phys. Chem. **88**, 5935, **(1984)**

[40] Q. Zhou, Q. Fan, Y. Zhuang, Y. Li, G. Zhao, and J. Zheng, J. Phys. Chem. B **110**, 12029, **(2006)**

[41] A. Campion, J. E. Ivanecky III, C. M. Child, and M. Foster, J. Am. Chem. Soc. **117**, 11807, **(1995)**

[42] P. Kambhampati, C. M. Child, M. C. Foster, and A. Campion, J. Chem. Phys. **108**, 5013, (1998)

[43] Z. Q. Tian and B. Ren, Annu. Rev. Phys. Chem. **55**, 197, **(2004)**

[44] Z. Q. Tian and B. Ren, Infrared and Raman Spectroscopy in Analysis of Surfaces, in Encyclopedia of Analytical Chemistry, edited by R. A. Meyers Wiley, New York, 2000_, pp. 9162–9201

[45] Q. J. Huang, X. Q. Li, J. L. Yao, B. Ren, W. B. Cai, J. S. Gao, B. W. Mao, and Z. Q. Tian, Surf. Sci. **427**, 162 **_(1999)_**

[46] R. Livingstone; L. G, Quagliano..; J, Fleumingue.; X, Zhou,; M. Tamargo; J.R, Lombardi; submitted for publication

[47] R. Livingstone, L. G. Quagliano, N. Perez-Paz, M. Munoz, M. C. Tamargo, F. Jean-Mary, and J. R. Lombardi, Proc. SPIE **6008**, 10 _2005

[48] L. Zhao, L. Jensen, and G. Schatz, J. Am. Chem. Soc. **128**, 2911, **(2006)**

[49] L. Zhao, L. Jensen, and G. Schatz, Nano Lett. **6**, 1229, **(2006)**

[50] R.L, Birke.; V. Znamenskily and J.R Lombardi; J. of Chem. Phys **132,** 214707 **(2010)**

[51] S.-Y. Lee and E. J. Heller, J. Chem. Phys. **71**, 4777,_**(1979)**

[52] E. J. Heller, R. L. Sundberg, and D. Tannor, J. Phys. Chem. **86**, 1822, **(1982)**

[53] P. A. M. Dirac, Proc. R. Soc. London, Ser. A **114**, 710, **(1927)**

[54]ADF _http://www.scm.com, 2005.

[55] A. C. Albrecht, J. Chem. Phys. **34**, 1476 , **(1961)**

[56] J.R, Lombardi,.; R.L, Birke. J. Chem. Phys (**2007)**, 126, 244709

[57] Albrecht, A. C. J. Chem. Phys. **1960**, 33, 169-178.

[58] Albrecht, A. C. J. Chem. Phys. **1960**, 33, 156-169.

Chapter 3 References

[59] Perspectives on the Physical Chemistry of Nanocrystals; Alivisatos, A.P., J.Phys.Chem., **1996,** 100, 13226.

[60] A single-electron transistor made from a cadmium selenide nanocrystal; Klein, D.L.;Roth, R.; Lim, A.K.L.; Alivisatos, A.P.; McEuen, P.L., Nature, **1997**, 389, 699.

[61] Light-emitting diodes made from cadmium selenide nanocrystals and a semiconducting polymer; Colvin, V.L.; Schlamp, M.C.; Alivisatos, A.P., Nature, **1994**, 370, 354.

[62] Cao, C.; Jin, R.; Mirkin, C.A., Science, 2002, 297, 1536-1762.

[63] Du, H.; Disney, M.D.; Miller, B.L.; Krauss, T.D., J.Am.Chem.Soc., 2003, 125, 4012-4013.

[64] Surface Enhanced Raman Scattering ; Chang, R.K.; Furtak, T.E.,(Plenum, New York, 1982).

[65]Surface Enhanced Raman Scattering; Van Duyne, R.P., Chemical and Biochemical Applications of Lasers, edited by C. B. Moore, (Academic Press, New York, 1979), Vol. 4, p.101.

[66] Surface Enhanced Spectroscopy; Moskovits, M., Rev. Mod. Phys**. 1985**, 57**,** 783.

[67] Surface Enhanced Raman Scattering; Birke, R.L.; Lombardi, J.R., in Spectroelectrochemistry: Theory and Practice Ed. R.J. Gale, Plenum,**1988**.

[68] Lombardi, J. R.; Birke, R.L.; Lu, T.; Xu, J., J. Chem. Phys.. **1986**, 84, 4357.

[69] Lombardi, J.R., Birke, R.L., J. Phys. Chem. C, **112** (14), 5605 -5617, (2008). 10.1021/jp800167v

[70]Blinking Surface-Enhanced Raman Scattering Observed in Single Colloidal Nanocrystals; Emory,S.R.; Han,M.; Doering,W., Nie, S., in Progress in Surface Raman Spectroscopy; Theory, Techniques and Applications, Ed. Z.Q. Tian, and B.Ren, Xiamen University Press, Xiamen, China, **2000**.

[71] Electromagnetic Field Enhancement and the Raman Spectra of Single R6G Dye Molecules; Michaels, A.; Brus, L. in Progress in Surface Raman Spectroscopy; Theory, Techniques and Applications, Ed. Z.Q. Tian, and B.Ren, Xiamen University Press, Xiamen, China, **2000**.

[72]Kottmann, J.P.; Martin, J.F., Smith, D.R.; Schultz, S., Phys. Rev. B, **2001**, 64, 1Chem.Phys. Lett **2001**, 34, 1.

[73] Uehara,J.;Nishihara,H.; Aramaki,K., J. Electrochem. Soc. **1990**, 137, 2677.

[74]Huang, Q.J.;Li, X.Q.;Yao, J.L.;Ren, B.;Cai, W.B.; Gao, J.S.; Mao, B.W.; Tian, Z.Q., Surface Science **1999**, 427, 162 .

[75] Cao,P.G.; Yao, J.L.; Ren, B.; Mao, B.W.; Gu, R.A.; Tian, Z.Q., Chem. Phys. Lett. **2000**, 316, 1.

[76] Quagliano, L. G: Orani D., Surface Science, **1996**, 368 (1996) 108.

[77] Quagliano, L., J.Am.Chem.Soc., 2004, 126, 7393-7398.

[78] Y. Wang, Z. Sun., Y. Wang, H. Hu, B. Zhao, W. Xu, J.R. Lombardi, Spectrochimica Acta A., **2007**, 66A, 1199-1203.

[79] Y. Wang, Z. Sun., Y. Wang, H. Hu, S. Jing, B. Zhao, W. Xu, C. Zhao, J.R. Lombardi, J. Raman Spectroscopy, J. Raman Spectry. **2007**, 38, 34-38.

[80] Y. Wang, Y. Wang, J. Zhang, H. Hu, J. Zhang, B. Zhao, B. Yang, J.R. Lombardi, submitted for publication.

[81] Y. Wang, H. Hu, S. Jing, Y. Wang, Z. Sun, B. Zhao, C. Zhao, J.R. Lombardi, Analytical Sciences, **2007**, 23, 787-791.

[82] Y. Wang, J. Zhang, H. Jia, M. Li, J. Zeng, B. Yang, B. Zhao, W. Xu, J.R. Lombardi, J. Phys. Chem. C, **2008**, 112, 996-1000: 10.1021/ jp077467h.

[83]II-VI Semiconductor materials and their applications, edited by Maria Tamargo, (Taylor & Francis, New York, 2002), Vol. 12.

[84] S.P. Guo, X.Zhou, O.Maksimov, M.C Tamargo, C. Chi, A. Couzis, C. Maldarelli, I.L.Kuskovsky, G.G. Neumark, J. Vac. Sci Technol. **B 19**, 1635 (2001)

[85] II-VI Semiconductor materials and their applications, edited by Maria Tamargo, (Taylor & Francis, New York, 2002), Vol. 12

[86] X.Zhou, M.C Tamargo, S.P Guo, and Y.C Chen; J.Elect. Mat. **Vol. 32**, No.7, 2003

[87] X. Zhou, M. Munoz, S. Guo, M.C. Tamargo, Y. Gu, I.L. Kuskovsky, G.F. Neumark, J. Vac. Sci. Technol. B, **2004**, 22, 1518.

[88] Lombardi, J.R.; Birke, R.L Foucault R; Vivoni A, J.Phys.Chem. B, 2003, 107, 5547-5557.

[89] Lombardi, J.R.; Birke, R.L., J. Phys. Chem. C., **2008**, 112, 5605.

[90] Z. Sun, B. Zhao, J. R. Lombardi, Appl. Phys. Lett., **2007**, 91, 221106.

[91] V.A. Fonoberov, A.A. Balandin, Appl. Phys. Lett., **2004**, 85, 5971.

[92] Alexander P. Richter, John R. Lombardi, Bing Zhao, in press J. Phys. Chem.C, 2010, 114, 1610-1614, DOI: 10.1021/jp909772e

[93] X. Zhou, M. Munoz, S. Guo, M.C. Tamargo, Y. Gu, I.L. Kuskovsky, G.F. Neumark, J. Vac. Sci. Technol. B, **2004**, 22, 1518

Chapter 4 References

[94] Fleischmann, M.; Hendra, P.J; McQuillan, A.J. *Chem. Phys. Lett* **1974**, 26 163

[95] Albrecht, M.G.; Creighton, J.A.: *J. Am. Chem. Soc*. 99, **1977**, 5215

[96] Paul R.L.; McQuillan A.J; Hendra P.J; and Fleischmann, M., *J. Electroanal. Chem*. 66 **1975**, 248.

[97] Jeanmaire, D.L.; van Dyne, R.P.; *J. Electroanal. Chem*. 84 **1977**, 1

[98] Otto, A. *Surface Sci.* 75, **1978**, L392

[99]Birke, R.L.; Lombardi, J.R.; Gersten, J.I.; *Phys. Rev. Lett*. 43 **(1979),** 495

[100] Bunding, K.A.; Birke, R.L.; Lombardi, J.R*; J. Chem. Phys*. 49 **(1980),** 53-58

[101] Bunding, K.A.; Birke, R.L.; Lombardi, J.R*; J. Chem. Phys*. 54 **(1980),** 115-121

[102] Sanchez, L.A.; Birke, R.L.; Lombardi, J.R.; *J. Phys. Chem* **1984**, 88, 1762-1766

[103] Moskovits, M.; *J. Chem. Phys.* 69, **1978**, 4159

[104] Tian, Z.Q.; Ren, B.; *Annu. Rev. Phys. Chem.* **2004**, 55, 197-229

[105] Wang, Y.; Sun, Z. Sun.; Hu, H.; Zhao, B.; Xu, W.; Lombardi, J.R.; *Spectrochimica Acta A.*, **2007**, 66A, 1199-1203

[106] Wang, Y.; Sun, Z. Sun.; Hu, H.; Zhao, B.; Xu, W.; Lombardi, J.R.; *J. Chem. Phys*.. **2008**, 112, 6093-6098

[107] Wang, Y.; Sun, Z. Sun.; Hu, H.; Zhao, B.; Xu, W.; Lombardi, J.R. *J. Raman Spectroscopy*, J. Raman Spectroscopy. **2007**, 38, 34-38.

[108] Moskovits, M.*;Surface Enhanced Spectroscopy; Rev. Mod. Phys***. 1985**, 57**,** 783.

[109]Van Duyne, R.P.; *Surface Enhanced Raman Scattering*; *Chemical and Biochemical Applications of Lasers*, edited by C. B. Moore, (Academic Press, New York, **1979**), Vol. 4, p.101.

[110] Chang, R.K.; Furtak, T.E.,*Surface Enhanced Raman Scattering* ;(Plenum, New York**, 1982**).

[111] Birke, R.L.; Lombardi, J.R.; *Surface Enhanced Raman Scattering*; *Spectroelectrochemistry: Theory and Practice* Ed. R.J. Gale, Plenum,**1988**

[112] Lombardi, J. R.; Birke, R.L.; Lu, T.; Xu, J., *J. Chem. Phys*.. **1986**, 84, 4357

[113] Lombardi, J.R., Birke, R.L., *J. Phys. Chem. C,* **112** (14), 5605 -5617, (**2008**). 10.1021/jp800167v

[114] Birke, R.L.; Znamenskiy, V.; Lombardi, R.L.;*J. Chem. Phys* 132, 214707, **2010**

[115] Livingstone, R; Quagliano, L. G.; Fleumingue, J.; Zhou, X,; Tamargo, M.; Lombardi, J. R; submitted for publication

[116]*Blinking Surface-Enhanced Raman Scattering Observed in Single Colloidal Nanocrystals*; Emory,S.R.; Han,M.; Doering,W., Nie, S., *in Progress in Surface Raman Spectroscopy; Theory, Techniques and Applications*, Ed. Z.Q. Tian, and B.Ren, Xiamen University Press, Xiamen, China, **2000.**

[117] *Electromagnetic Field Enhancement and the Raman Spectra of Single R6G Dye Molecules*; Michaels, A.; Brus, L. in *Progress in Surface Raman Spectroscopy; Theory, Techniques and Applications*, Ed. Z.Q. Tian, and B.Ren, Xiamen University Press, Xiamen, China, **2000.**

[118]Kottmann, J.P.; Martin, J.F., Smith, D.R.; Schultz, S., *Phys. Rev. B,* **2001**, 64, 1 *Chem.Phys. Lett.* **2001**, 34, 1.

[119] Quagliano, L., *J.Am.Chem.Soc*., 2004, 126, 7393-7398.

[120] Livingstone, R; Quagliano, L. G.; Prez-Paz, N.M.; Fleumingue, J.; Tamargo, M.; Lombardi, J. R, Manuscript in preparation

[121] Merz, J.L.; Lee, S.; Furdyna, J.K.; *J. of Crystal Growth* 184/185, **1998**, 228-236

[122] Rijnberg, E.; Kroon, J.M.; *et al; Proc. World Conf. PVSEC, 2nd **1998**, 47*

[123] Nazeeruddin, M.K.; Kay, A.; Rodicio, I.; Humphry-Baker, R.; Mueller, E.; Liska, P.; Vlachopoulos, N.; Gratzel, M.; *J. Am. Chem. Soc*, **1993**, 115, 6382

[124] Gratzel, M.; Kalyanasundaram, K.; *Curr. Sci*. **1994**, 66, 706

[125] Schlichthorl, G.; Huang, S.Y.; Sprague, J.; Frank, A.J.; .; *J. Phys. Chem. B,* **1997**, 101, 8139

[126] Greijer, H.; Lindgren, J.; Hagfeldt. A.; *J.Phys.Chem. B,* **2001**, 105, 6314-6320

[127] Katoh, R.; Kasuya, M.; Kodate, S.; Furube, A.; Fuke, N.; Koide, N.; *J. Phys. Chem. C*, **2009**, 113 (48), pp 20738–20744, DOI: 10.1021/jp906190a

[128] Shi, C.; Dai, S.; Wang, K.; Pan, X.; Kong, F.; Hu, L.*; J. Vib. Spect*. 39**, 2005**, 99-105

[129] Katoh, R.; Kasuya, M.; Furube, A.; Fuke, N.; Koide, N.;Han, L.; *J. Mat. Chem*. **2007**, 17, 3190.

[130] Erdheim, G.R.; Birke, R.L.; Lombardi, J.R.; *J. Chem. Phys. Lett*. 69, **1980**, 495

[131] Lombardi, J.R.; Birke, R.L Foucault R; Vivoni A, *J.Phys.Chem. B*, **2003**, 107, 5547-5557

[132] Dollish, F.R.; Fateley, W.G.; Bentley, R.F.; *Characteristic Raman Frequencies of Organic Compounds*. *John Wiley & Sons, Inc*, **1974,** pp 170-175

Chapter 5 References

[133] Livingstone, R; Quagliano, L. G.; Fleumingue, J.; Zhou, X,; Tamargo, M.; Lombardi, J. R; submitted for publication

[134]L. Zeng, S. P. Guo, Y.Y. Luo, W. Lin, M.C. Tamargo, H. Xing, and G.S. Cargill, III, *J. Vac. Sci. Technol*., **B17**, 1255 (1999).

[135]*II-VI Semiconductor materials and their applications*, edited by Maria Tamargo, (Taylor & Francis, New York, 2002), Vol. 12

[136] X. Zhou, M. Munoz, S. Guo, M.C. Tamargo, Y. Gu, I.L. Kuskovsky, G.F. Neumark, *J. Vac. Sci. Technol. B*, **2004**, 22, 1518.

[137] Livingstone, R; Lombardi, J. R; submitted for publication.

[138] Lombardi, J.R.; Birke, R.L., *J. Phys. Chem. C.*, **2008**, 112, 5605.

[139] Birke, R.L.; Znamenskiy, V.; Lombardi, R.L.;*J. Chem. Phys* 132, 214707, **2010**

[140]. Z. Sun, B. Zhao, J. R. Lombardi, *Appl. Phys. Lett*., **2007**, 91, 221106.

[141] V.A. Fonoberov, A.A. Balandin, *Appl. Phys. Lett*., **2004**, 85, 5971

[142] Alexander P. Richter, John R. Lombardi, Bing Zhao, J. Phys. Chem., **2010**, 114, 1610-1614, DOI: 10.1021/jp909772e

[143] X. Zhou, M. Munoz, S. Guo, M.C. Tamargo, Y. Gu, I.L. Kuskovsky, G.F. Neumark, *J. Vac. Sci. Technol. B*, **2004**, 22, 1518

[144] Giese, B.;McNaughton, D., *J.Phys.Chem. B*, 2002, 106, 101.

[145] Rava, R.P.; Spiro, T.G., *J.Phys.Chem.*, 1985, 89, 1856-1861.

[146]Cao, X.; Fischer, G., *J.Phys.Chem.A*, 1999, 103, 9995-10003.

[147] Grace, L.; Cohen, R.; Dunn,T.; Lubman, D.M.; de Vries, A.S., *J. Molec. Spectry*., 2002, 215, 204-219

[148] Siamwiza, M.N.; Lord, R.C.; Chen, M.C.; Takamatsu, T.; Harada, I.; Matsuura, H.; Shimanouchi, T., *Biochemistry*, 1975, 14, 4870.

[149] Ebina, A.; Asano, K.; Takahashi, T., *Phys. Rev. B.*, 1980, 22, 1980.

[150]Bowen Katari, J.E.; Colvin, V.L.; Alivastatos, A.P., *J. Phys. Chem*. 1994, 98, 4109-4117.

[151] Lombardi, J.R.; Birke, R.L.; Lu, T.; Xu,J., *J. Chem. Phys*.**1986**, 84, 4174

[152] Lombardi, J.R., Birke, R.L., *J. Phys. Chem. C*, **112** (14), 5605 -5617, (**2008**). 10.1021/jp800167v

Chapter 6 References

[152] Harborne, J.B.; *The Flavonoids: Advances in Research Since 1986*. Chapman and Hall: London, **1994**

[153] Ferreira, E.S.B, Hulme A.N.; McNab, H.; Quye, A.; *Chem. Soc. Rev*. **2004**; **33**: 329.

[154] Harborne J.B.; Marby, T.J.; Marby, H.; *The Flavonoids*. Chapman and Hall: London, **1975.**

[155] Harborne J.B.; Marby, T.J.; *The Flavonoids: Advances in Research*. Chapman and Hall: London, **1982**.

[156] McClure, J.W.; *Plant Flavonoids in Biology and Medicine: Biochemical, Pharmacological and Structure-Activity Relationships;* Cody, V.; Middleton, E.; Harborne J.B.; (eds). Alan, R.; Liss: New York, **1986**; 77.

[157] Geissman, T.A.; *The Chemistry of Flavonoid Compounds*. The Macmillan Company: New York, 1**962**.

[158] Smith, D.A.; Banks, S.W.; *In Plant Flavonoids in Biology and Medicine: Biochemical, Pharmacological and Structure-Activity Relationships*; Cody, V.; Middleton, E.; Harborne J.B.; (eds). Alan, R.; Liss: New York **,1986**; 113.

[159] Gabor, M.; *The Pharmacology of Benzopyrone Derivatives and Related Compounds. Akademiai Kiado: Budapest*, **1986**

[160] Hofenk de Graaff, J.H.; *The Colorful Past. Origins, Chemistry and Identification of Natural Dyestuffs*. Abegg-Stiftung and Archetype Publications: Riggisberg, London, **2004**.

[161] Jose, C.I.; Phadke, P.S.; Rao, A.V.R.; *Spectrochem. Acta* **1974**; **30A**: 1199.

[162] Dean, F.M.; *Naturally Occurring Oxygen Ring Compounds*. Butterworth: London, **1963**; 280

[163] Marby, T.J.; Markham, F.K.; Thomas, M.B.; *The Systematic Identification of Flavonoids*. Springer: Berlin, **1970.**

[164]Sengupta, P.K.; Kasha, M.; *Chem. Phys. Lett.* **1979**; **68**: 382.

[165] Brewer, W.E.; Studet, S.L.; Standiford, M.; Chou, P.T.; *J. Phys. Chem.* **1989**; **93**: 6088.

[166] Dzugan, T.P.; Schmidt, J.; Aartsma, T.J.; *Chem. Phys. Lett.* **1986; 127**(4): 336.

[167]Looker, J.H.; Hanneman, W.W.; *J. Org. Chem.* **1962**; **27**: 381.

[168] Shaw, L.; Simpson, T.H.; *J. Chem. Soc.* **1955**; 655.

[169] Hergert, H.L.; Kurth, E.F.; *J. Am. Chem. Soc.* **1953**; **75**: 1622

[170] Looker, J.H.; Hanneman, W.W.; Kagal, S.A.; Dappen, J.I.; Edman, J.R.; *J. Hetero-Cycl. Chem.* **1966**; **3**: 55.

[171] Looker, J.H.; Kagal SA, Dappen JI, Edman JR. *J. Hetero-Cycl. Chem.* **1966**; **3**: 61

[172] del Valle JC. *J. Chem. Phys.* 2006; **124**: 104506.

[173] Briggs LH, Colebrook LD. *Spectrochim. Acta* 1962; **18**: 939.

[174] Amaral, D.F.; Arruda, M.S.P.; Arruda, A.C.; Muller, A.H.; Pantoja, L.L.J.; da S, Lima T.M.; *J. Braz. Chem. Soc.* **2001**; **12**(4): 538.

[175] Torreggiani, A.; Trinchero, A.; Tamba, M.; Taddei, P.; *J. Raman Spectrosc.* **2005**; **36**: 380

[176]Cornard, J.P.; Merlin, J.C.; Boudet, A.C.; Vrielynck, L. *Biospectroscopy* **1997**; **3**(3): 183.

[177] Petroski, J.M.; Valente, C.D.S.; Kelson, E.P.; Collins, S.; *J. Phys. Chem., A* **2002**; **106**: 11714

[178] Livingstone R.; Quagliano, L.G.; Perez-Paz, N.; Munoz, M.; Tamargo, M.C.; Jean-Mary, F.; Lombardi, J.R.; Proc. SPIE **6008**, 10, **2005.**

[179] Daeid, N.N.; (ed.) Review Papers, 14th International Forensic Science Symposium, Interpol-Lyon, 19–22 October **2004** [Online]. Available: www.interpol.int/Public/Forensic/IFSS/meeting 14/ReviewPapers.pdf.

[180] Chen, K.; Leona, M.; Vo-Dinh, K.C.; Yan, F.; Wabuyele, M.B.; Vo-Dinh, T.; *J. Raman Spectrosc.* **2006**; **37**: 520.

[181] Birke, R.L.; Lu, T.; Lombardi, J.R.; *Techniques for Characterization of Electrodes and Electrochemical Processes*, Varma, R.; Selam, J.R.; (eds). John Wiley and Sons, Inc: New York, **1991**; Chapt. 5.

[182] Lee, P.C.; Meisel, D.; *J. Phys. Chem.* **1982**; **86**: 3391.

[183] Frisch, M.J.; Trucks, G.W.; Schlegel, H.B.; Scuseria, G.E.; Robb, M.A.; *et al*.; *Gaussian 03, Revision C.02*. Gaussian, Inc: Wallingford, CT, **2004**.

[184] Silman, O.; Bumm, L.A.; Callaghan, R.; Blatchford, C. G.; Kerker, M..; *J. Phys. Chem.* **1983**; **87**: 1014.

[185] Wang, M.; Teslova, T.; Xu, F.; Lombardi J.R, Birke, R..L.; Leona, M.; *J. Phys. Chem.* 2007; DOI: 10.1021/jp062100i.

[186] Wang M, Spataru T, Lombardi J.R, Birke RL. *J. Phys. Chem.* 2007; DOI: 10.1021/jp0650937.

[187] Rauhut, G.; Pulay, P.; *J. Phys. Chem.* **1995**; **99**: 3093.

[188] Pulay, P.; Fogarasi, G.; Pongor, G.; Boggs, J.E.; Vargha, A.; *J. Am. Chem. Soc.* 1983; **105**: 7037

[189] Neugebauer, J.; Hess, B.A.; *J. Chem. Phys.* **2003**; **118**: 7215.

[190] Sanchez-Cortes, S.; Francioso, O.; Garcia-Ramos, J.V.; Ciavatta, C.; Gessa, C.; *Colloids Surf. A: Physicochem. Eng. Aspects* **2001**; **176**: 177.

[191] Leona, M.; Stenger, J.; Ferloni, E.; *J. Raman Spectrosc.* **2006**; **37**: 981.

[192] Leona, M.; *Surface enhanced Raman scattering in art and archaeology*, Proc. of SPIE Vol. 5993, 5993L-1. SPIE-The International Society for Optical Engineering, Bellingham, WA, USA, **2005**

[193] Leona, M.; *Identification of Natural Dyes in Works of art by SERS Techniques*: Recent Progress and Remaining Problems. ICORS: Yokohama, 2006;; 20, August **2006**.

[133]

[134] L. Zeng, S. P. Guo, Y.Y. Luo, W. Lin, M.C. Tamargo, H. Xing, and G.S. Cargill, III, *J. Vac. Sci. Technol*., **B17**, 1255 (1999).
[135] *II-VI Semiconductor materials and their applications*, edited by Maria Tamargo, (Taylor & Francis, New York, 2002), Vol. 12.

[136] X. Zhou, M. Munoz, S. Guo, M.C. Tamargo, Y. Gu, I.L. Kuskovsky, G.F. Neumark, *J. Vac. Sci. Technol. B*, **2004**, 22, 1518.

[137] Livingstone, R; Lombardi, J. R; submitted for publication.

[138] Lombardi, J.R.; Birke, R.L., *J. Phys. Chem. C.*, **2008**, 112, 5605.

[139] Birke, R.L.; Znamenskiy, V.; Lombardi, R.L.;*J. Chem. Phys* 132, 214707, **2010**

[140] Z. Sun, B. Zhao, J. R. Lombardi, *Appl. Phys. Lett*., **2007**, 91, 221106.

[141] V.A. Fonoberov, A.A. Balandin, *Appl. Phys. Lett*., **2004**, 85, 5971.

[142] Alexander P. Richter, John R. Lombardi, Bing Zhao, J. Phys. Chem., **2010**, 114, 1610-1614, DOI:

10.1021/jp909772e

[143] X. Zhou, M. Munoz, S. Guo, M.C. Tamargo, Y. Gu, I.L. Kuskovsky, G.F. Neumark, *J. Vac. Sci.*

Technol. B, **2004**, 22, 1518

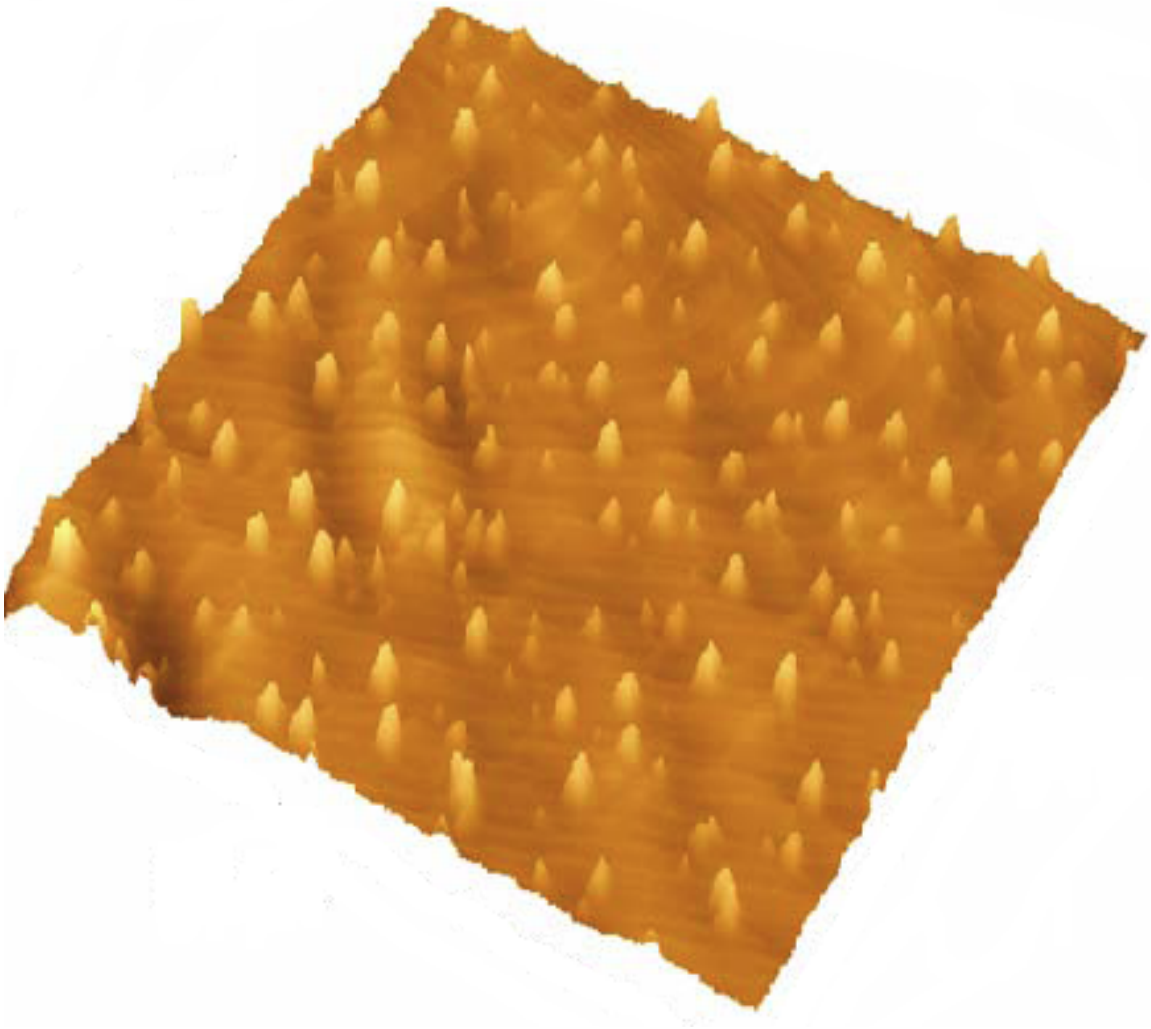

Figure 1a. Three dimensional AFM image for uncapped QD with 2ML-CdSe nominal thickness and 39% MgSe content in the ZnCdMgSe barrier

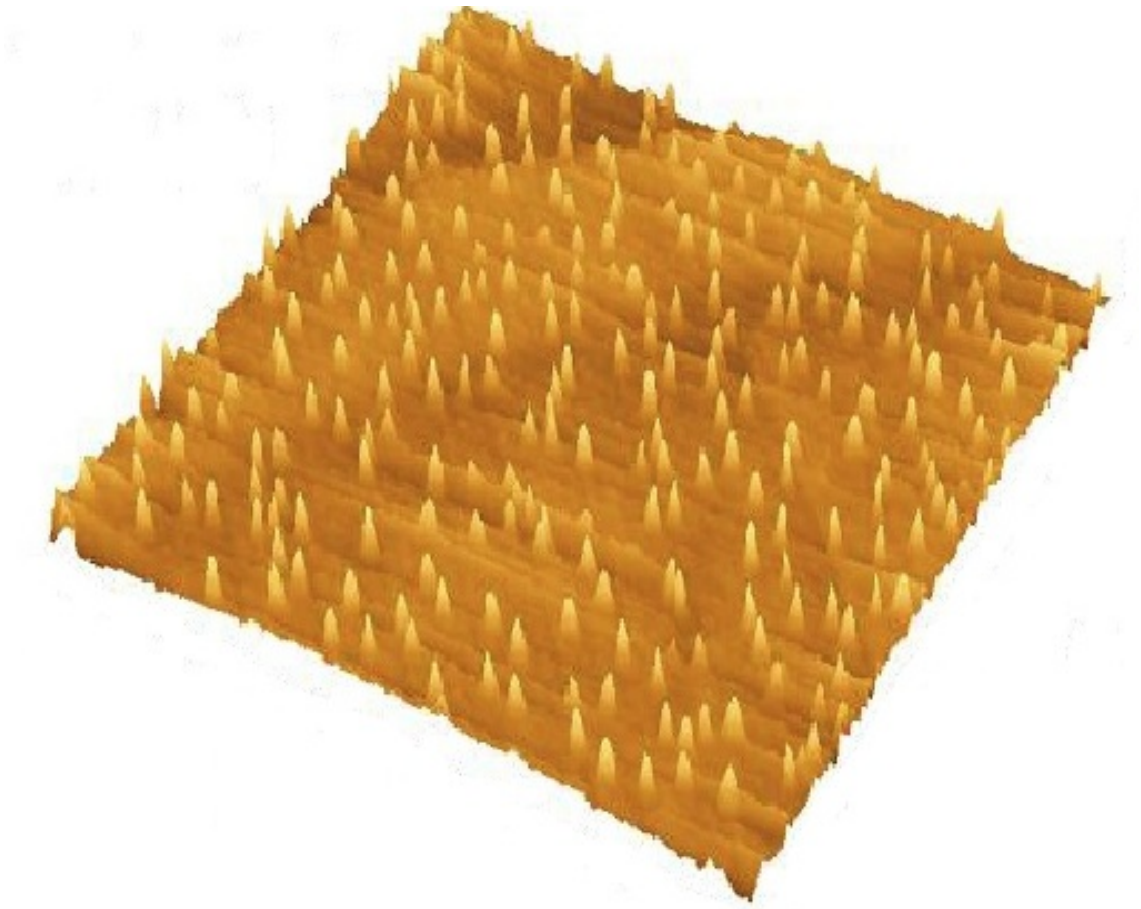

Figure 1b. Three dimensional AFM image for uncapped QD with 2ML-CdSe nominal thickness and 59% MgSe content in the ZnCdMgSe barrier

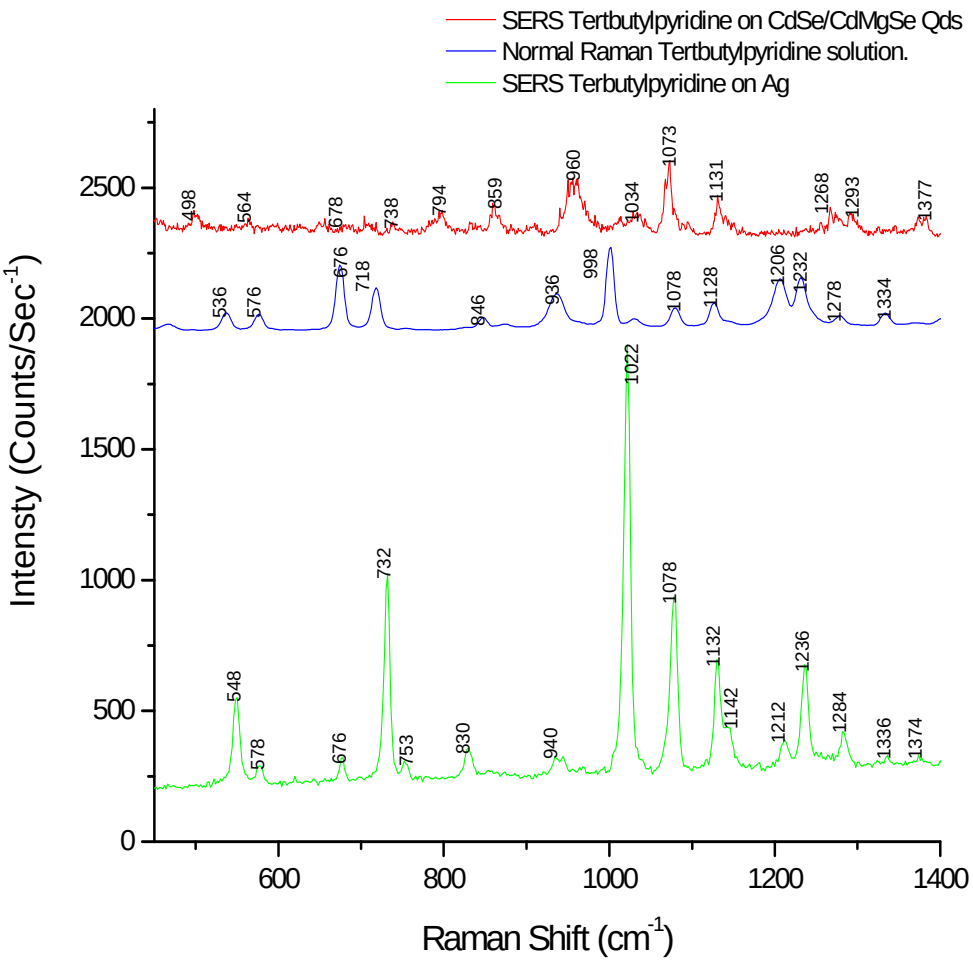

Figure2. Normal Raman and SERS spectrum of 4-tbutylpyridine on Ag and CdSe quantum dots (quaternary bandgap ~2.6 eV) excited at 488 nm. Richard: In the text you mention a spectrum of substrate alone w/o molecule—this should be added. Also move the top two to the bottom, or else make all the spectra comparable in maximum intensity by scaling.

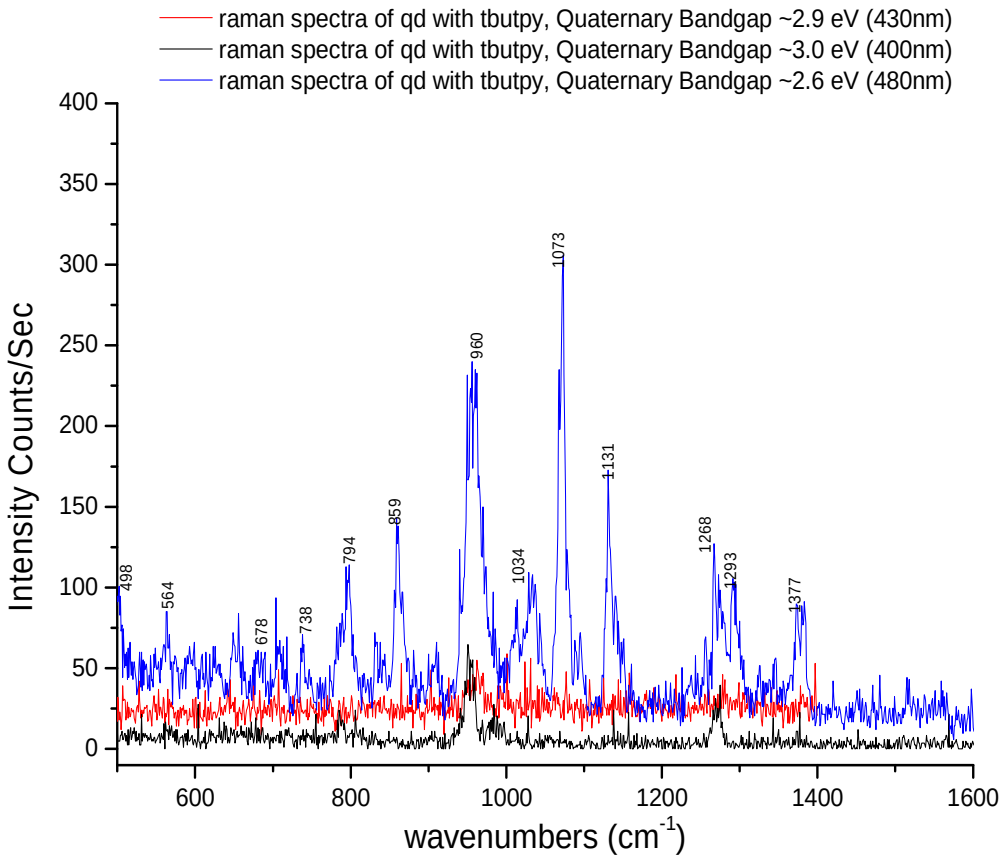

Fig 3 SERS spectrum of 4-t-butylpyridine on CdSe quantum dots, grown with different quaternary bandgap and excited at 488 nm. Richard: Do we have a spectrum with bandgap >3.0, perhaps without any lines to add to this? Also could you separate the lines a bit more, so that we can more easily see the spectra?

Wilson no	C_{2v} Symm	Hberg Assmt	t butpy Liquid (NR)	t butpy Ag (SERS)	t butpy CdSe/ ZnMgSe
		ν_{10}	536 (w)	548(s)	
			576(w)	578(m)	564(w)
6a	a_1	ν_{19}	676(s)	678(m)	678(vw)
6b	b_2	ν_{25} oop	718(m)	732(vs)	738(vw)
4	b_1			753(w)	794(w)
		$\nu_{24,}\nu_9$	846(vw)	830(m)	859(mw)
	a_2	ν_8 (oop)	936(m)	940(w)	960(s)
1	a_1	ν_8	1002(s)	1022(vs)	
12	a_1		1034 (vw)		1034(vw)
18b	b_2	$\nu_{7,}M_6$	1080 (w)	1078(vs)	1073(s)
9b	b_2		1128 (w)	1132(s)	1131(m)
15	b_2	$M_6(b_2)$		1142(sh)	
9a	a_1		1206(m)	1212(w)	
9a	a_1	m_1, ν_6	1232(m)	1236(s)	
3	b_2	M_3	1278(w)	1284(m)	1268(m)
3	b_2	M_3	1334(w)	1374(vw)	1377(m)
19b	b_2	M_4	1450(m)	1452(vw)	
19a	a_1	ν_5	1472(m)	1472(vw)	
			1554(vw)	1554(vw)	
8a	a_1	ν_4	1602(s)	1618(vs)	

Table 1: Assignment of tert butylpyridine lines as observed in Normal Raman, SERS on a Ag surface and on ZnCdMgSe /CdSe self-assembled quantum dots. Quaternary bandgap ~ 2.6 eV

Livingstone, R; Lombardi, J. R; submitted for publication.Richard: See our t-butyl SERS Ag paper—there are some corrections to the assignements—you should add explanation of notation—e.g. what does M mean? Give refeneces. Also, there are a few large shifts on going to the CdSe surface—can we justifiy these?What happens to nu1? (Isn't this also the same as with the previous spectrum in pyridine? Why are some of the normal modes assignments doubled? (i.e. nu 9a and nu3).

[144] Giese, B.;McNaughton, D., *J.Phys.Chem. B*, 2002, 106, 101.

[145] Rava, R.P.; Spiro, T.G., *J.Phys.Chem.*, 1985, 89, 1856-1861.

[146] Cao, X.; Fischer, G., *J.Phys.Chem.A*, 1999, 103, 9995-10003.

[147] Grace, L.; Cohen, R.; Dunn,T.; Lubman, D.M.; de Vries, A.S., *J. Molec. Spectry*., 2002, 215, 204-219

[148] Siamwiza, M.N.; Lord, R.C.; Chen, M.C.; Takamatsu, T.; Harada, I.; Matsuura, H.; Shimanouchi, T., *Biochemistry*, 1975, 14, 4870.

[149] Ebina, A.; Asano, K.; Takahashi, T., *Phys. Rev. B.*, 1980, 22, 1980.

[150] Bowen Katari, J.E.; Colvin, V.L.; Alivastatos, A.P., *J. Phys. Chem*. 1994, 98, 4109-4117.

Table 1: Raman spectra of Adenine on CdSe quantum dots excited at 488 nm.

NR-solid	Mode #	Description	SERS-632nm	CdSe-488nm
536	27,28	NH wag	536	541
560	25	CH wag	553	556
				572
623	24	Ring def	621	621
			690	707
723	21	Ring breath	731	731
797	20	Ring def	788	787
839	19	CH wag		836
				870
899	18	NCN def		893

942	17	NCN def	958	956
974(calc)	16	CH wag		976
				987
1025	15	rock -NH_2	1029	
				1048
				1065
				1077
				1095
1126	14	CN str	1117	
1162	13	CH bend		1152
1234	12	rock -NH_2	1245	
1248	11	CH bend		1253
			1270	1277
				1293
1308	10	CN str		1305
1333	8,9	CH bend	1326	1320
				1360
1372	7	CH bend	1372	1387
1419	6	CN str	1399	1421
1463	5	sciss -NH_2	1460	
1483	4	sciss -NH_2		
1597	3	sciss -NH_2		
1613	2	CN str		
1674	1	sciss -NH_2		

Normal Raman (NR) of solid, Mode assignments and SERS at 632nm from: Giese, B. McNaughton, D., *J. Phys. Chem. B*, 2002, 106, 101-112.

Table 2: Raman spectra of Tryptophan on CdSe quantum dots excited at 488 nm.

Raman-liq 200nm	**Description**	**IR-liq Zwitterion**	**Description**	**CdSe 488nm**
		529	def,r,R	531
		555	β-NH(r)	555
		581	β-NH(r)	586
		613	β-CH	600
				624
		640	def,r	647
		660		674

		694	def,r	691
		725	def,r,R	715
762	ring-brth	763	β-CO_2^-	761
				782
		794	β-CO_2^-	808
		821	def,r,R	832
		843	β-H,R	853
880	skel+NH	875	β-NH_3^+	873
		928	β-CH_2	945
		955 calc		966
		990 calc		990
1016	ring-brth	1007	ν_{CN},β-NH_3^+	1008
		1045	β-NH_3^+	
1127	9b	1111	β-H,R	1110
1148	15 or δNH	1153	ν_{CC}	1134
				1155
1238	3	1226	β-CH,νR	1240
1256		1273	νR	1269
		1283	νR	1281
1305	5π	1316	β-CH_2	1308
1342	14			1331
		1352	β-CH	
1361	14π			
1434	6π	1432	β-CH,νR	
1462	19b	1457	β-NH_3^+	
1496	19a	1489	νR	
		1526	νT	1532
1555	ring-str	1569	β-NH_3^+	1558
1578	8b	1578	νR	
1622	8a	1625	ν_{as}-CO_2^-	1650

Liquid Raman Spectrum from: Rava, R.P.; Spiro, T.G., *J.Phys.Chem.*, 1985, 89, 1856-1861.

IR spectrum of Zwitterion from: Cao, X.; Fischer, G., *J.Phys.Chem.A*, 1999, 103, 9995-10003.

R-benzene ring, r-pyrrole ring, ν-stretch, β-bend

Table 3: Raman spectra of Tyrosine on CdSe quantum dots excited at 488 nm.

Raman-liq pH-7 200 nm	Assmt	Raman-solid 532 nm	Assmt	CdSe 488 nm
		535	16b	529
		558	Chain	542
				614
		641	6b	651
				662
		714	4	706
		739(IR)	12	732
				748
				775

		797	$-NH_2$ wag	791
		807		812
831	2X16a(oop)	828	1	834
853	1 (ring br)	845	2X16a(oop)	857
		939	5	930
		971	17a	957
		982	CH_2 rock	983
		989	CH_2 rock	1002
		1016	18a	1029
		1046	C-N str	1068
		1153		1154
				1168
1180	9a	1179	9a	1181
		1200		
1210	p-subst-str	1213	7a	
		1251	-OH bend	1252
1263	7a	1263	14	1281
				1306
		1329	13	
		1370	CH bend	
1443	19b	1437	19b	
1519	19a	1513	19a	
1601	8a	1598	8b	
1617	10	1616	8a	

Liquid Raman Spectrum from: Rava, R.P.; Spiro, T.G., *J.Phys.Chem.*, 1985, 89, 1856-1861.
Raman solid 532 nm: Grace, L.; Cohen, R.; Dunn,T.; Lubman, D.M.; de Vries, A.S., *J. Molec. Spectry*., 2002, 215, 204-219

[151] Lombardi, J.R.; Birke, R.L.; Lu, T.; Xu,J., *J. Chem. Phys.***1986**, 84, 4174.

[152]